



**Max-Planck-Institut für Metallforschung**  
Stuttgart

---

## **Cementite in the Fe–N–C system**

Marc Nikolussi

Dissertation  
an der  
**Universität Stuttgart**

---

Bericht Nr. 220  
November 2008



# **Cementite in the Fe–N–C system**

Von der Fakultät Chemie der Universität Stuttgart zur  
Erlangung der Würde eines Doktors der Naturwissenschaften (Dr. rer. nat.)  
genehmigte Abhandlung

vorgelegt von

**Marc Nikolussi**

aus Ehenbichl

Hauptberichter: Prof. Dr. Ir. E.J. Mittemeijer

Mitberichter: Priv.-Doz. Dr. J. Bill

Prüfungsvorsitzender: Prof. Dr. H. Bertagnolli

Tag der Einreichung: 28.08.2008

Tag der mündlichen Prüfung: 18.11.2008

**INSTITUT FÜR METALLKUNDE DER UNIVERSITÄT STUTTGART**  
MAX-PLANCK-INSTITUT FÜR METALLFORSCHUNG, STUTTGART  
STUTTGART, 2008



# Table of contents

<b>1</b>	<b>General Introduction</b> .....	<b>7</b>
1.1	Cementite formation; a literature overview .....	11
1.2	Thermodynamic considerations .....	12
1.2.1	Gaseous nitriding .....	12
1.2.2	Gaseous carburising .....	15
1.2.3	Gaseous nitrocarburising .....	18
1.3	Outline of the work .....	19
1.3.1	Formation of massive cementite compound layers and its growth kinetics .....	19
1.3.2	Orientation relationships of cementite and ferrite and the consequences ...	22
1.3.3	Diffusivity of nitrogen and activation energy of nitrogen diffusion in cementite .....	22
1.3.4	New information on the Fe–N–C system .....	23
1.3.5	Elastic constants of cementite .....	24
	References .....	25
<b>2</b>	<b>Formation of massive cementite layers on iron by ferritic carburising in the additional presence of ammonia</b> .....	<b>29</b>
2.1	Introduction .....	30
2.2	Experimental procedure .....	31
2.2.1	Specimen preparation and thermochemical treatment .....	31
2.2.2	Analysis of the (nitro-)carburised specimens .....	32
2.3	Results and discussion .....	34
2.3.1	Influence of the ammonia content in the atmosphere on the layer constitution .....	34
2.3.2	Cementite layer-growths kinetics .....	39
2.4	Conclusions .....	41
	References .....	42

<b>3 Growth of massive cementite layers; thermodynamic parameters and kinetics.....</b>	<b>45</b>
3.1 Introduction.....	46
3.2 Experimental.....	47
3.3 Results and evaluation .....	49
3.4 Discussion.....	52
3.4.1 Parabolic layer growth for interstitial compounds.....	52
3.4.2 Thermodynamics of gaseous nitrocarburising.....	53
3.4.3 Interpretation of the “apparent” activation energy .....	57
3.5 Conclusions.....	61
References.....	62
<b>4 Microstructure and crystallography of massive cementite layers on ferrite substrates.....</b>	<b>65</b>
4.1 Introduction.....	66
4.2 Experimental.....	67
4.2.1 Specimen preparation and gaseous nitrocarburising .....	67
4.2.2 Microstructural and crystallographic analysis .....	68
4.3 Experimental results .....	71
4.3.1 Morphology of cementite compound layers.....	71
4.3.2 Orientation relationship cementite-ferrite.....	72
4.3.3 Preference of orientation-relationship variants.....	73
4.4 Discussion.....	75
4.4.1 The Bagaryatsky orientation relationship; cementite/ferrite misfit.....	75
4.4.2 Surface misfit-strain energy of cementite grains; orientation favouritism .....	77
4.4.3 Orientation relationship of adjacent cementite grains; consequence for the cementite-layer growth.....	79
4.4.4 Comparison with $\gamma'$ -Fe <sub>4</sub> N <sub>1-y</sub> .....	81
4.5 Conclusions.....	83
Acknowledgement .....	84
References.....	84

---

<b>5 Nitrogen diffusion through cementite layers.....</b>	<b>87</b>
5.1 Introduction.....	88
5.2 Experimental.....	89
5.2.1 Specimen preparation and gaseous nitriding/nitrocarburising .....	89
5.2.2 Microstructural and hardness analysis.....	91
5.3 Experimental results and evaluation:	
hardness measurements and chemical analysis .....	94
5.4 Modelling nitrogen concentration-depth profile development.....	98
5.4.1 General assumptions .....	98
5.4.2 Simulation of nitrogen concentration-depth profiles;	
numerical procedure .....	104
5.5 Results of the simulation.....	104
5.6 Concluding discussion .....	107
5.6.1 Hardness/concentration-depth profiles .....	107
5.6.2 Simulation of nitrogen concentration-depth profiles.....	108
5.7 Conclusions.....	110
Appendix.....	112
References.....	115
<b>6 Examination of phase transformations in the system Fe–N–C by means of nitrocarburising reactions and secondary annealing experiments; the <math>\alpha + \epsilon</math> two-phase equilibrium.....</b>	<b>119</b>
6.1 Introduction.....	120
6.2 Experimental.....	124
6.3 Results.....	126
6.3.1 Nitrocarburising experiments of set (a) ( $T_1 = 823$ K).....	126
6.3.2 Secondary annealing experiments of sample A.....	127
6.3.3 Nitrocarburising experiments of set (b) ( $T_1 = 853$ K).....	128
6.3.4 Secondary annealing experiments of sample B.....	130
6.4 Discussion .....	130
6.4.1 Nitrocarburising experiments at $T_1 = 823$ K and $T_1 = 853$ K .....	130
6.4.2 Secondary annealing experiments .....	132

6.5 Conclusions.....	136
References.....	136
<b>7 Extreme elastic anisotropy of cementite, Fe<sub>3</sub>C: First-principles calculations and experimental evidence by X-ray diffraction stress measurements .....</b>	<b>139</b>
Acknowledgement .....	149
References.....	150
<b>8 Summary.....</b>	<b>153</b>
8.1 Introduction.....	153
8.2 Experimental Procedure.....	154
8.3 Results and Discussion .....	155
8.3.1 Formation of massive cementite compound layers and its growth kinetics.....	155
8.3.2 Orientation relationships of cementite and ferrite and the consequences .	157
8.3.3 Diffusivity of nitrogen and activation energy of nitrogen diffusion in cementite .....	159
8.3.4 New information on the Fe–N–C system .....	160
8.3.5 Elastic constants of cementite.....	161
<b>9 Zusammenfassung in deutscher Sprache .....</b>	<b>163</b>
9.1 Einleitung.....	163
9.2 Experimentelle Vorgehensweise.....	165
9.3 Ergebnisse und Diskussion .....	166
9.3.1 Erzeugung von reinen, massiven Zementitschichten und deren Wachstumskinetik.....	166
9.3.2 Orientierungsbeziehung zwischen Zementit und Ferrit und die daraus resultierenden Konsequenzen.....	168
9.3.3 Stickstofftransport durch Zementit .....	170
9.3.4 Neue Informationen über das Fe–N–C system.....	171
9.3.5 Elastische Konstanten des Zementits.....	172
<b>List of publications.....</b>	<b>173</b>
<b>Danksagung .....</b>	<b>175</b>
<b>Curriculum Vitae .....</b>	<b>177</b>



# 1

## ***General Introduction***

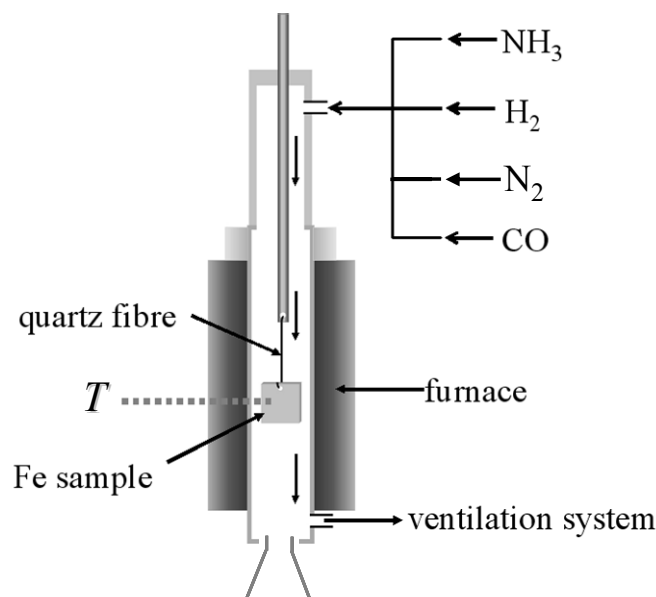
In technical applications, layer/substrate systems are of increasing importance since they may result in positive properties, which cannot be achieved by (simple) bulk materials. A layer/substrate system combines two components, the substrate material and the layer on top of the substrate. The aim is to realise a material combination which benefits from the positive properties of both the substrate such as e.g. ductility and the positive properties of the layer such as e.g. hardness and corrosion resistance. This materials combination may overcome negative properties such as e.g. the limited hardness of the substrate and the brittleness of the layer. Such layer/substrate systems can be generated by different processes, e.g. by thermochemical heat treatments due to chemical reactions of a reactive gas atmosphere with the substrate material [1-3].

Gaseous nitriding, gaseous carburising and gaseous nitrocarburising are such thermochemical heat treatments, which are of pronounced technical importance since the beginning of the twentieth century. These processes lead, due to chemical reactions of the reactive gas atmosphere with the substrate material, to a concerted change of the chemical composition of the (usually) iron-based workpieces. This concerted change of the chemical composition can lead to the formation of a diffusion zone within which nitrogen and/or carbon are either dissolved in the octahedral sites of the iron *bcc*-lattice or are bound to alloying elements. The diffusion zone, which can extend several hundreds of micrometers, is responsible for a considerable enhancement of the fatigue endurance of the iron-based workpiece [4]. Furthermore, under certain circumstances (high activities of nitrogen and/or carbon in the gas atmosphere), the change of the chemical composition of the iron-based workpiece can lead to the generation of hard, wear and corrosion resistant surface compound layers with thicknesses up to several

tenths of micrometers [5]. Gaseous nitriding and gaseous nitrocarburising are performed at temperatures in the range of 773 K – 843 K, i.e. below the binary/ternary eutectoid temperatures (ferritic regime) of the Fe–N/Fe–N–C solid solution [2]. Upon gaseous nitriding and/or gaseous nitrocarburising, nitrogen and/or carbon are diffusionally incorporated into the surface region of an iron-based workpiece. In contrast, upon carburising, carbon is incorporated into the surface region of an iron-based workpiece at usually much higher treatment temperatures in the range of 1173 – 1273 K. Due to these higher treatment temperatures, which are located in the austenitic regime, considerable changes of the dimensions of the iron-based workpiece result, which is in contrast to gaseous nitriding/nitrocarburising.

In the present work, thermochemical heat treatments were performed in a vertical quartz tube furnace. At the top part of the quartz-tube furnace, the gas inlet was located, where ammonia, hydrogen, carbon monoxide and nitrogen were inserted into the furnace. The specimen was positioned by a sample stage and a quartz fibre in the middle of the quartz-tube furnace where the process temperatures, controlled within  $\pm 1$  K, prevailed. The quartz-tube furnace was, at its bottom part, equipped with a water container for quenching the specimens to room temperature. After the desired treatment time, the quartz fibre was mechanically destroyed and the specimen dropped into the quenching facility to retain microstructural states which were produced at the treatment temperature.

(a)



(b)

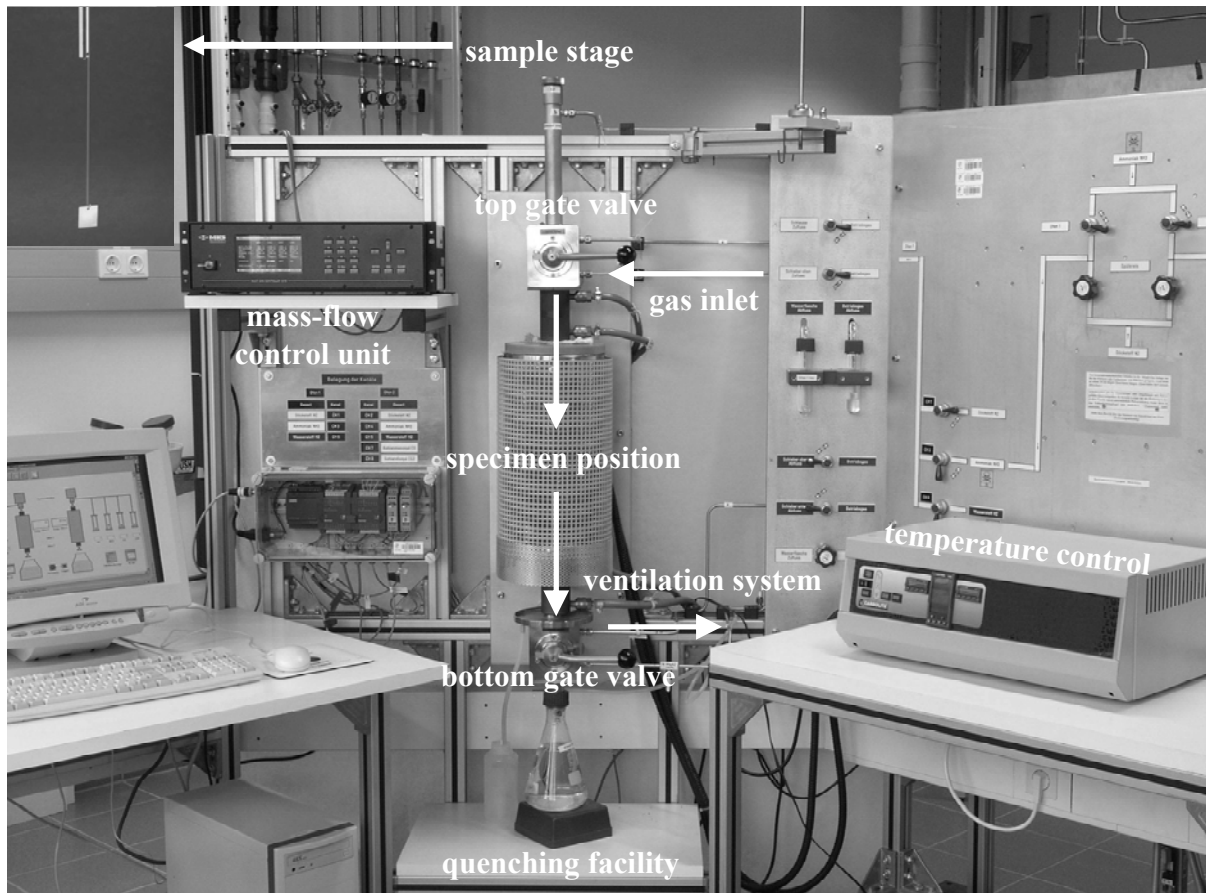


**Fig. 1.1:** (a) Schematic representation and (b) real image of the nitriding/nitrocarburising/carburising facility. The arrows indicate the gas inlet, the direction of the gas flow and the gas outlet. At the bottom part of the nitriding/nitrocarburising/carburising facility, the quenching facility was located, which consists of a water container (flushed with nitrogen).

After the thermochemical heat treatment (in the present work gaseous nitriding/nitrocarburising), a diffusion zone develops within which  $\alpha''$ - $\text{Fe}_{16}\text{N}_2$  [6-10] or  $\gamma'$ - $\text{Fe}_4\text{N}_{1-y}$  precipitates can be formed. On top of this diffusion zone a compound layer develops which can, depending on the process parameters (treatment temperature, treatment pressure, treatment time, composition of the gas atmosphere) consist of different phases [11,12]. Usually the compound layer consists of  $\gamma'$ - $\text{Fe}_4\text{N}_{1-y}$  and/or  $\epsilon$ - $\text{Fe}_3(\text{N,C})_{1+x}$  [13] but, also cementite can form within the compound layer [14,15] (cf. *chapter 2*) coexisting with  $\gamma'$ - $\text{Fe}_4\text{N}_{1-y}$  and  $\epsilon$ - $\text{Fe}_3(\text{N,C})_{1+x}$ .

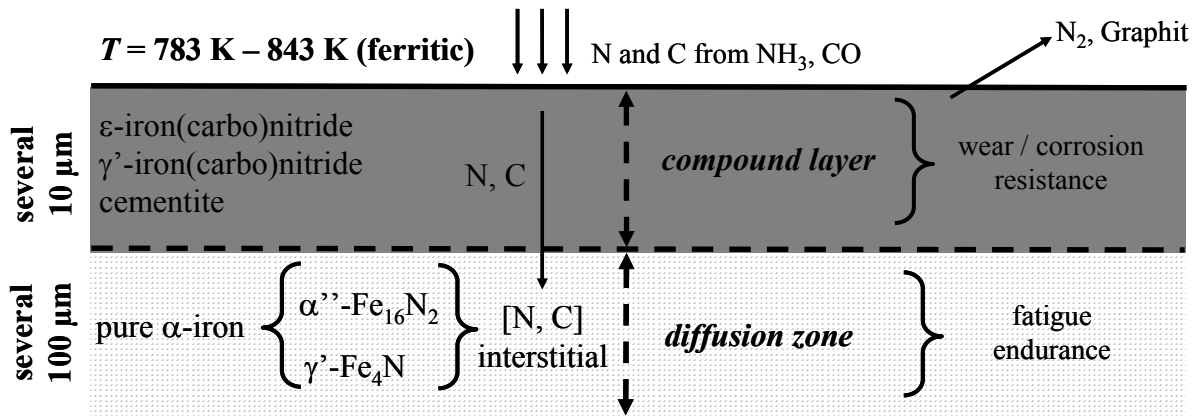


**Fig. 1.2:** Schematic illustration, which indicates that the surface region of an iron-based workpiece can be subdivided into a diffusion zone and a compound layer after gaseous nitriding/nitrocarburising. These contain, depending on the process parameters, different phases. Nitrogen and/or carbon are provided by the ammonia- and/or carbon monoxide-containing gas atmosphere. Ammonia and/or carbon monoxide dissociation occurs at the surface of the specimen. Due to a gradient of the chemical potential of nitrogen and/or carbon from the surface to the substrate, nitrogen and/or carbon are diffusively incorporated into the surface region of the iron-based workpiece.

The formation of massive cementite compound layers upon gaseous carburising is usually accompanied by severe sooting and cementite disintegration, so-called metal dusting [16]. Therefore, the generation of massive cementite compound layers is not trivial. In the literature it is reported that due to the addition of  $\text{H}_2\text{S}$  to the carburising gas atmosphere, sooting and metal dusting can be suppressed [17-20]. Moreover, there are hints that the addition of ammonia to the carburising gas atmosphere may delay or even suppress sooting and metal dusting [21].

Although gaseous nitrocarburising is widely applied in industrial processes, many open questions remain. The aim of this work is to generate massive cementite compound layers on ferrite substrates. Furthermore, the present work shall answer some open questions concerning cementite in the Fe–N–C system.

## 1.1 Cementite formation; a literature overview

The formation of cementite is of great industrial importance but also of great scientific interest. Cementite is, besides ferrite, the most important phase present in the majority of steels. In the following, a literature overview will be given, introducing several techniques to produce bulk cementite or cementite layers. Cementite, as found in cementite-containing low- and mildly-alloyed steels, will not be discussed.

In Ref. [22] it is reported that cementite can be obtained in a wear-resistant case hardened layer (thickness up to 0.5 mm) on cast iron. For that, the surface area of an iron-based workpiece will be heated and finally molten by a high-power energy source (e.g. laser, electron beam) under argon atmosphere. Due to heat transfer into the bulk material the surface area of the workpiece is cooled by itself after the heating process. By this heating process, graphite particles, which are present in the cast iron, have been transformed into a high-energy state which let them react to cementite. The addition of magnesium to the cast iron hinders graphite to react with oxygen (present although the process is performed under argon atmosphere), which would result in the formation of carbon monoxide gas bubbles which would negatively influence the mechanical properties of the cast iron.

Umemoto et al. [23] reported that it is possible to produce bulk cementite blocs by mechanical alloying and afterwards spark plasma sintering. Elemental iron powder and elemental graphite powder were mixed in stoichiometric ratio and mechanical alloying was performed by ball milling under argon atmosphere. The alloyed powder has been sintered by a spark-plasma under vacuum and under pressure in order to produce compacts of cementite.

Another method to produce cementite was introduced by Carpenne and Schaaf [24]. Cementite emerges from pure iron substrates which have been irradiated by a pulsed excimer-laser under methane atmosphere. The reaction chamber has to be evacuated before filling it with methane in order to remove oxygen. Cementite-layer thicknesses of about 1  $\mu\text{m}$  can be obtained by this process.

Further, it was reported by Mizubayashi et al. [25] that cementite can be deposited on silicon substrates by the so-called “electron-shower-assisted physical vapour deposition” (ES-PVD).

Cementite can also be formed by gaseous carburising of iron powders or iron foils. Thereby, cementite is formed upon a reaction of e.g. the iron foils with a reactive carburising gas atmosphere ( $\text{CO}/\text{H}_2/\text{H}_2\text{O}$ ,  $\text{CH}_4/\text{H}_2$ ) [16,20]. The addition of  $\text{H}_2\text{S}$  to the gas atmosphere suppresses sooting and cementite disintegration, so-called metal dusting which usually accompany the cementite forming reaction [16,20].

Besides the mentioned techniques for the formation of cementite, Naumann and Langenscheid [26] reported that there are hints that an addition of ammonia to the carburising gas atmosphere should also make the formation of cementite possible. In Ref. [21] it is further reported that there are indications that nitrogen-delivering species in the gas atmosphere can suppress carbon deposition on an iron-based surface. Furthermore, Naumann and Langenscheid assumed that the addition of nitrogen-providing media, such as ammonia, should increase carbon uptake into the iron substrate [26]. However, experiments performed by these authors indicate that cementite can only coexist with other phases within the compound layer. Pure, massive cementite layers were not produced in that work [26].

In *chapter 2* of this work a new method will be presented by which massive cementite layers on ferrite substrates can be generated. The cementite-layer thicknesses which can be achieved are in the range of several micrometers allowing investigation by different instrumental techniques.

## 1.2 Thermodynamic considerations

### 1.2.1 Gaseous nitriding

The term gaseous nitriding describes a thermochemical heat treatment upon which nitrogen is incorporated into the surface region of an iron-based workpiece [2]. Since the chemical potential of nitrogen in  $\text{N}_2$  is extremely low, it is not possible to incorporate a considerable amount of nitrogen (neither as iron nitrides nor as solid solution in iron) into the surface region of an iron-based workpiece;  $\text{N}_2$  can be considered as inert gas (cf. phase diagram [3], Fig. 1.3). In order to achieve such nitriding by  $\text{N}_2$ , an equilibrium  $\text{N}_2$ -pressure up to several thousand atmospheres [27] would be necessary.

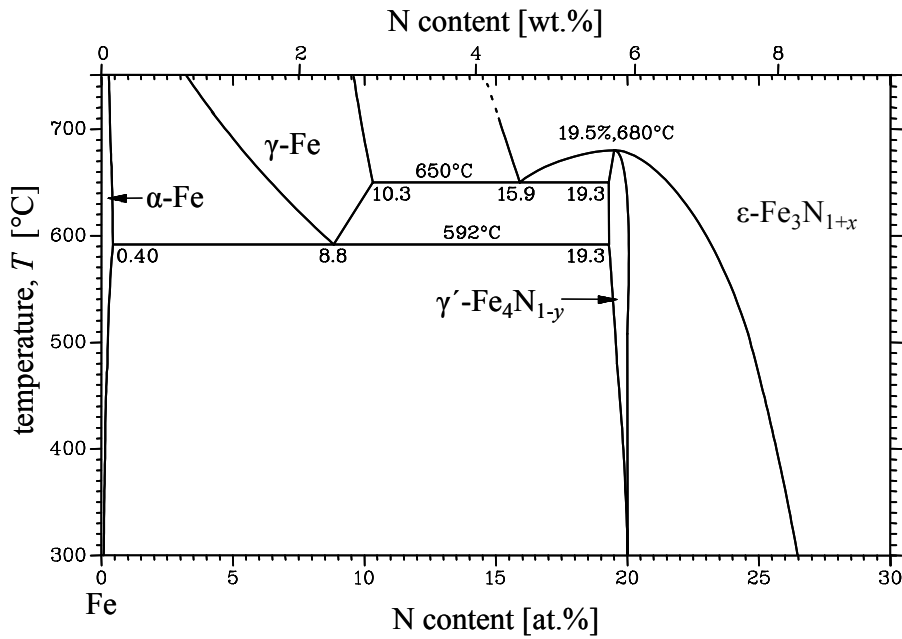


**Fig. 1.3:** Part of the metastable Fe–N phase diagram which has been redrawn according to Ref. [3].

Since the chemical potential of nitrogen in ammonia is relatively high, ammonia is well suited as nitrogen-providing medium. Upon nitriding the following chemical equilibrium has to be considered



where  $[\text{N}]$  represents nitrogen which is dissolved in the surface region of the iron-based workpiece. For the analysis of the thermodynamics of gaseous nitriding, two chemical reactions have to be considered, which hypothetically take place. The hypothetical dissociation of ammonia can be expressed by



The nitrogen which was (hypothetically) produced by this chemical reaction can be incorporated into the surface region of the iron-based workpiece according to



In order that Eq. (1.1) can be considered as chemical equilibrium, it is necessary that the occurrence of ammonia dissociation according to Eq. (1.2) within the gas atmosphere can be neglected. This can be realised by applying a relatively high flow rate of  $13.5 \text{ mm s}^{-1}$  (calculated for the gas volume at room temperature) through the quartz retort (diameter 28 mm). Furthermore, it has to be ensured that no nitrogen recombination according to Eq. (1.3) takes place. If these two premises are fulfilled, Eq. (1.1) can be considered as chemical equilibrium, i.e. local equilibrium between the gas atmosphere and the specimen surface holds.

Under the assumption that the components of the gas atmosphere can be treated as ideal gases, the chemical potential  $\mu_{\text{N}}^{\text{surface}}$  in the solid at the surface of the specimen (assumed to be in equilibrium with the gas atmosphere), which is the partial Gibbs free energy obeys

$$\mu_{\text{N}}^{\text{surface}} = \frac{1}{2} \mu_{\text{N}_2}^0 + RT \ln a_{\text{N}}^{\text{surface}} = \mu_{\text{NH}_3}^0 - \frac{3}{2} \mu_{\text{H}_2}^0 + RT \ln \left( r_{\text{N}} (p^0)^{\frac{1}{2}} \right), \quad (1.4)$$

where  $\mu_{\text{N}_2}^0$ ,  $\mu_{\text{NH}_3}^0$  and  $\mu_{\text{H}_2}^0$  are the chemical potentials of nitrogen, ammonia and hydrogen in the gaseous reference state (pressure  $p^0 = 1 \text{ atm}$ ) and  $a_{\text{N}}^{\text{surface}}$  is the activity of nitrogen dissolved in the solid at the surface. The expression  $r_{\text{N}} = \frac{p_{\text{NH}_3}}{p_{\text{H}_2}^{3/2}}$  denotes the so-called nitriding potential, where  $p_{\text{NH}_3}$  and  $p_{\text{H}_2}$  are the partial pressures of ammonia and hydrogen in the gas atmosphere, which quantifies the chemical potential of nitrogen [27]. The activity of nitrogen dissolved in the solid at the surface (assumed to be in equilibrium with the gas atmosphere),  $a_{\text{N}}^{\text{surface}}$ , equals

$$a_{\text{N}}^{\text{surface}} = \exp \left( - \frac{\frac{1}{2} \mu_{\text{N}_2}^0 + \frac{3}{2} \mu_{\text{H}_2}^0 - \mu_{\text{NH}_3}^0}{RT} \right) (p^0)^{1/2} r_{\text{N}}. \quad (1.5)$$

The chemical potential of nitrogen as well as the activity of nitrogen in the solid at the surface are governed by the nitriding potential. Therefore, a desired value of the chemical potential/activity of nitrogen in the solid at the surface can be adjusted by



controlling the partial pressures of ammonia and hydrogen by mass-flow controllers. At a certain nitriding potential and treatment temperature, the gas atmosphere is then either in equilibrium with an iron-nitride phase or a Fe–N solid solution [28-31] which is displayed by the Lehrer diagram [32]. The extended Lehrer diagram given by Fig. 1.4 contains isoconcentration lines, which indicate the expected nitrogen content in the respective phase under the applied gaseous nitriding conditions [33].

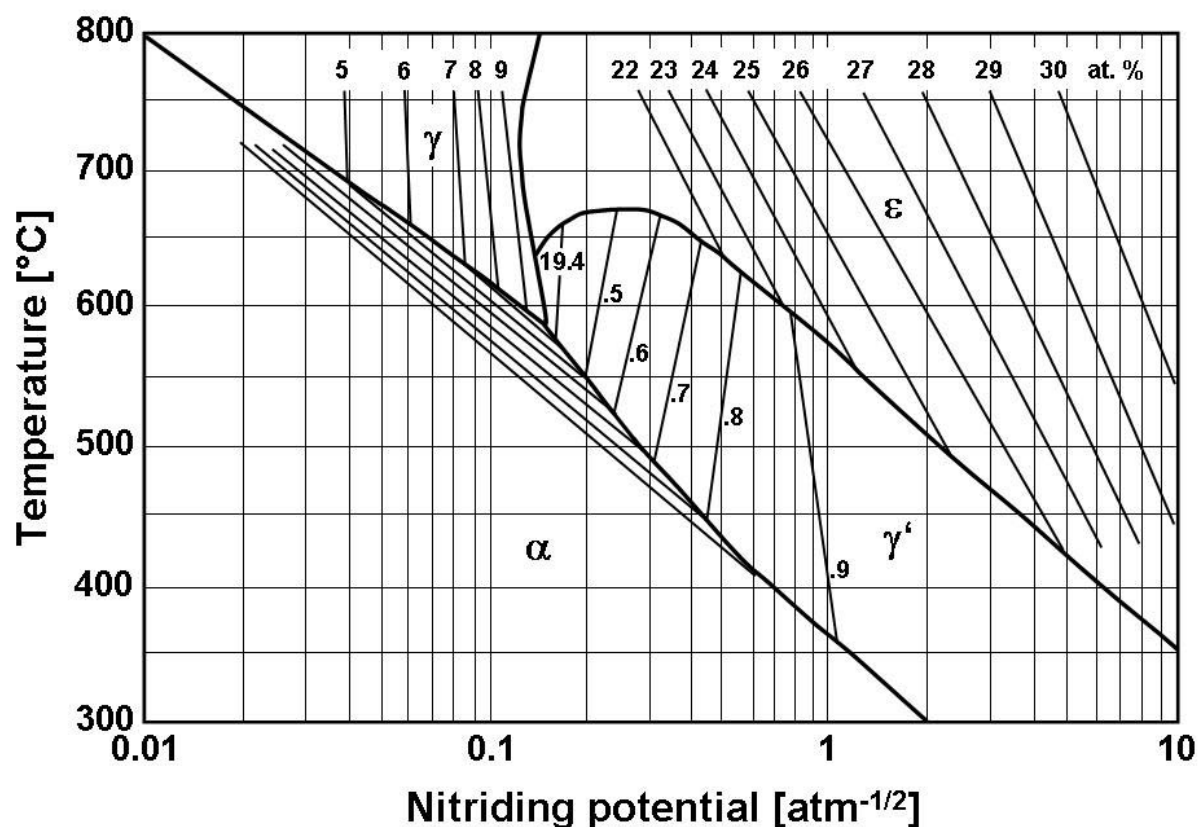


**Fig. 1.4:** The so-called extended Lehrer diagram (redrawn according to [33]). The diagram displays which phase is in equilibrium with the gas atmosphere under an applied nitriding potential, which quantifies the chemical potential/activity of nitrogen in the solid at the surface of the specimen. The isoconcentration lines indicate the expected nitrogen content in the respective phase under the applied gaseous nitriding conditions [33].

### 1.2.2 Gaseous carburising

Gaseous carburising in contrast describes a thermochemical heat treatment where carbon is incorporated into the surface region of an iron-based workpiece. Different chemical compounds could be used as carbon supply, the following considerations are

based on carbon monoxide as carbon supply as performed in the present work. Carbon transfer from carbon monoxide into the surface region of the iron-based workpieces proceeds via the water-gas reaction (if hydrogen is additionally present in the gas atmosphere)



or via the Boudouard reaction



where  $[\text{C}]$  denotes carbon dissolved in iron either as Fe–C solid solution or in a carbide. It has been shown experimentally that the heterogeneous water-gas reaction given by Eq. (1.6) is faster than the Boudouard reaction given by Eq. 1.7 [34]. Therefore, the water-gas reaction is assumed to control carburising.

Under the assumption that the components of the gas atmosphere can be treated as ideal gases, the chemical potentials of carbon in the solid at the surface (assumed to be in equilibrium with the gas atmosphere) according to Eqs. (1.6) and (1.7),  $\mu_{\text{C},(1.6)}^{\text{surface}}$  and  $\mu_{\text{C},(1.7)}^{\text{surface}}$ , equal

$$\mu_{\text{C},(1.6)}^{\text{surface}} = \mu_{\text{C}}^0 + RT \ln a_{\text{C}}^{\text{surface}} = \mu_{\text{CO}}^0 + \mu_{\text{H}_2}^0 - \mu_{\text{H}_2\text{O}}^0 + RT \ln \left( r_{\text{C},(1.6)} (p^0)^{-1} \right), \quad (1.8)$$

and

$$\mu_{\text{C},(1.7)}^{\text{surface}} = \mu_{\text{C}}^0 + RT \ln a_{\text{C}}^{\text{surface}} = 2\mu_{\text{CO}}^0 - \mu_{\text{CO}_2}^0 + RT \ln \left( r_{\text{C},(1.7)} (p^0)^{-1} \right), \quad (1.9)$$

where  $\mu_{\text{C}}^0$  is the chemical potential of graphite in the reference state (pressure  $p^0 = 1$  atm),  $\mu_{\text{H}_2}^0$ ,  $\mu_{\text{H}_2\text{O}}^0$ ,  $\mu_{\text{CO}}^0$  and  $\mu_{\text{CO}_2}^0$  are the chemical potentials of hydrogen, water, carbon monoxide and carbon dioxide in the gaseous reference state and  $a_{\text{C}}^{\text{surface}}$  is the

activity of carbon dissolved in the solid at the surface. The expressions  $r_{C,(1.6)} = \frac{p_{CO}p_{H_2}}{p_{H_2O}}$  and  $r_{C,(1.7)} = \frac{p_{CO}^2}{p_{CO_2}}$  denote the so-called carburising potentials according to Eqs. (1.6) and (1.7), which quantify the chemical potential/activity of carbon in the solid at the surface, where  $p_{H_2}$ ,  $p_{H_2O}$ ,  $p_{CO}$  and  $p_{CO_2}$  are the partial pressures of hydrogen, water, carbon monoxide and carbon dioxide in the gas atmosphere. The activities of nitrogen dissolved in the solid at the surface (assumed to be in equilibrium with the gas atmosphere) according to Eqs. (1.6) and (1.7),  $a_{C,(1.6)}^{surface}$  and  $a_{C,(1.7)}^{surface}$ , equal

$$a_{C,(1.6)}^{surface} = \exp\left(-\frac{\mu_C^0 + \mu_{H_2O}^0 - \mu_{CO}^0 - \mu_{H_2}^0}{RT}\right)(p^0)^{-1} r_{C,(1.6)} \quad (1.10)$$

and

$$a_{C,(1.7)}^{surface} = \exp\left(-\frac{\mu_C^0 + \mu_{CO_2}^0 - 2\mu_{CO}^0}{RT}\right)(p^0)^{-1} r_{C,(1.7)}. \quad (1.11)$$

For each of the chemical equilibria given by Eqs. (1.6) and (1.7) a separate chemical potential/carbon activity in the solid at the surface can be calculated. The chemical potentials of carbon as well as the activities of carbon in the solid at the surface according to Eqs. (1.8), (1.9) and (1.10), (1.11), respectively, are governed by the carburising potentials. Therefore, desired values of the chemical potential/activity of carbon in the solid at the surface can be adjusted by controlling the partial pressures of hydrogen, water, carbon monoxide and carbon dioxide. Real local equilibrium between the gas atmosphere and the specimen surface might be created by choosing the partial pressures of the components of the gas atmosphere such that the chemical potential/activities of carbon in the solid at the surface calculated according to Eqs. (1.8), (1.9) and (1.10), (1.11), respectively, exhibit the same value.

### 1.2.3 Gaseous nitrocarburising

Gaseous nitrocarburising describes a thermochemical heat treatment where both nitrogen and carbon are diffusionally incorporated into the surface region of an iron-based workpiece [2]. Therefore, gaseous nitrocarburising represents in principle a combination of gaseous nitriding and gaseous carburising, but, however (usually) performed in the ferritic regime (cf. gaseous nitriding). Gaseous nitrocarburising is more complex<sup>1.1</sup> since interactions between the gas atmosphere of gaseous nitriding and gaseous nitrocarburising occur. Therefore, e.g. the following chemical equilibria have additionally to be considered



In case of desired thermodynamic control of gaseous nitrocarburising, i.e. unequivocal determination of the nitrogen *and* carbon activity in the solid at the surface of the specimen, simultaneous equilibrium for all possible reactions in the gas atmosphere has to be fulfilled. This, however, requires the simultaneous control of the partial pressures of  $\text{NH}_3$ ,  $\text{H}_2$ ,  $\text{CO}$ ,  $\text{CO}_2$ ,  $\text{CH}_4$  and  $\text{H}_2\text{O}$  in the gas mixture with mass-flow controllers.

Since thermodynamic control of gaseous nitrocarburising is not trivial and requires a complex nitrocarburising facility, a simple solution was used in the course of the present study. Gaseous nitrocarburising was performed using dedicated  $\text{NH}_3/\text{H}_2/\text{CO}/\text{N}_2$ -containing gas mixtures. Whereas an unequivocal determination of the activity of nitrogen in the solid at the surface of the specimen can be realised, the

---

<sup>1.1</sup> The complexity of gaseous nitrocarburising originates from the presence of hydrogen in the nitrocarburising gas atmosphere. The presence of hydrogen is inevitable since it is necessary to control nitriding. Furthermore, hydrogen can also be formed at the surface of the specimen due to ammonia dissociation at this location.

carbon activity in the solid at the surface yields for the present gas atmosphere according to Eqs. (1.10) and (1.11) infinity, since neither  $\text{H}_2\text{O}$  (cf. Eq. (1.6)) nor  $\text{CO}_2$  (cf. Eq. (1.7)) were initially present in the nitrocarburising gas atmosphere ( $p_{\text{H}_2\text{O}} = p_{\text{CO}_2} = 0$ ). Nevertheless, it is concluded that a finite carbon activity rules in the solid at the surface of the specimen [35] (cf. *chapter 3*). The stationary presence of a certain amount of water, which is produced according to the chemical equilibrium given by Eq. (1.13) lowers the activity of carbon in the solid at the surface of the specimen according to Eq. (1.10) from an infinite to a finite, “effective” value [35] (cf. *chapter 3*). Furthermore, it can be assumed that the higher the fraction of carbon monoxide in the gas atmosphere is, the higher the finite, “effective” carbon activity in the solid at the surface is.

## 1.3 Outline of the work

### 1.3.1 Formation of massive cementite compound layers and its growth kinetics

There is a dearth of fundamental knowledge on cementite and the growth kinetics of cementite layers. This is mainly due to the fact that the formation of massive cementite compound layers with strongly carburising gas atmosphere, which exhibit high carbon activities, is always accompanied by simultaneous graphite deposition (sooting) on top of the initially formed cementite layer and cementite disintegration, so-called metal dusting [16]. Since sooting and metal dusting are undesired processes, at least in the view of technical processes, fundamental research was undertaken to elucidate whether these processes can be suppressed. The addition of  $\text{H}_2\text{S}$  to the gas atmosphere suppresses these processes by blocking the adsorption sites for carbon monoxide [20], but, due to the reduction of the number of adsorption sites for carbon monoxide, only limited cementite-layer thicknesses can be achieved.

In *chapter 2* and *3* of the present work, dissenting from the addition of  $\text{H}_2\text{S}$  to the gas atmosphere, a different approach for the suppression of sooting/metal dusting will be applied. To a carburising gas atmosphere, which is composed of carbon monoxide and hydrogen, a specific amount of nitrogen will be added. Since nitrogen can in the

course of these experimental conditions be considered as inert gas, an initially formed cementite layer will decompose into its components iron and graphite, i.e. sooting and metal dusting will take place as in the course of usual gaseous carburising in the absence of  $N_2$  (cf. Fig. 1.5). If a specific amount of the nitrogen is exchanged by ammonia, the initially formed cementite layer will remain stable and will not decompose into iron and graphite, i.e. sooting/metal dusting will be suppressed.

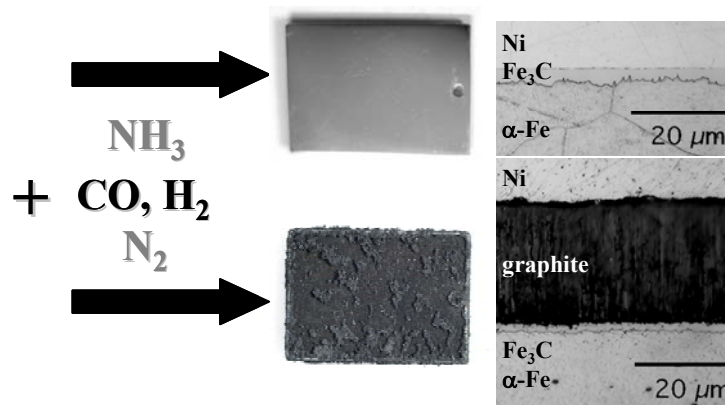


**Fig. 1.5:** Difference between the addition of a specific amount of nitrogen (inert gas) in contrast to a specific amount of ammonia to a carburising gas atmosphere, which is composed of carbon monoxide and hydrogen. Whereas by the addition of nitrogen severe sooting and cementite disintegration (metal dusting) occur, these processes will be suppressed by the addition of a specific amount of ammonia to the gas atmosphere.

Furthermore, in *chapter 2* of the present work it will be demonstrated that the cementite-layer thickness increases with increasing ammonia content. A probable explanation for the accelerating effect of ammonia on the cementite-layer growth will be given.

In the literature, the growth of iron-nitride layers is reported to be of parabolic fashion [28,30,36-39]. Very little is known about the growth kinetics of cementite layers, the studies existing in the literature [16,39,40] describe cementite-layer growth also in terms of parabolic layer growth. In *chapter 2* and *3* of the present study, the cementite-layer growth kinetics will be investigated. A modified parabolic-growth law holds for the whole temperature range within which cementite-layer growth succeeds. Cementite growth proceeds via a two stage mechanism. In the early stage, an incompletely closed cementite layer occurs. Carbon diffusion is relatively slow in

cementite as compared to ferrite [20]. Therefore, carbon diffusion takes place preferably through ferrite, bypassing the cementite (cf. Fig. 1.6a). Shortly after a closed cementite layer will have formed, short-circuit diffusion of carbon through thin and defect-rich parts of the cementite layer, which exhibit a high grain-boundary density, will occur. Both the bypass and the short-circuit mechanism will be faster as compared to later stages, where carbon volume diffusion through cementite will take place (cf. Fig. 1.6b), which can be expressed by parabolic cementite-layer growth.

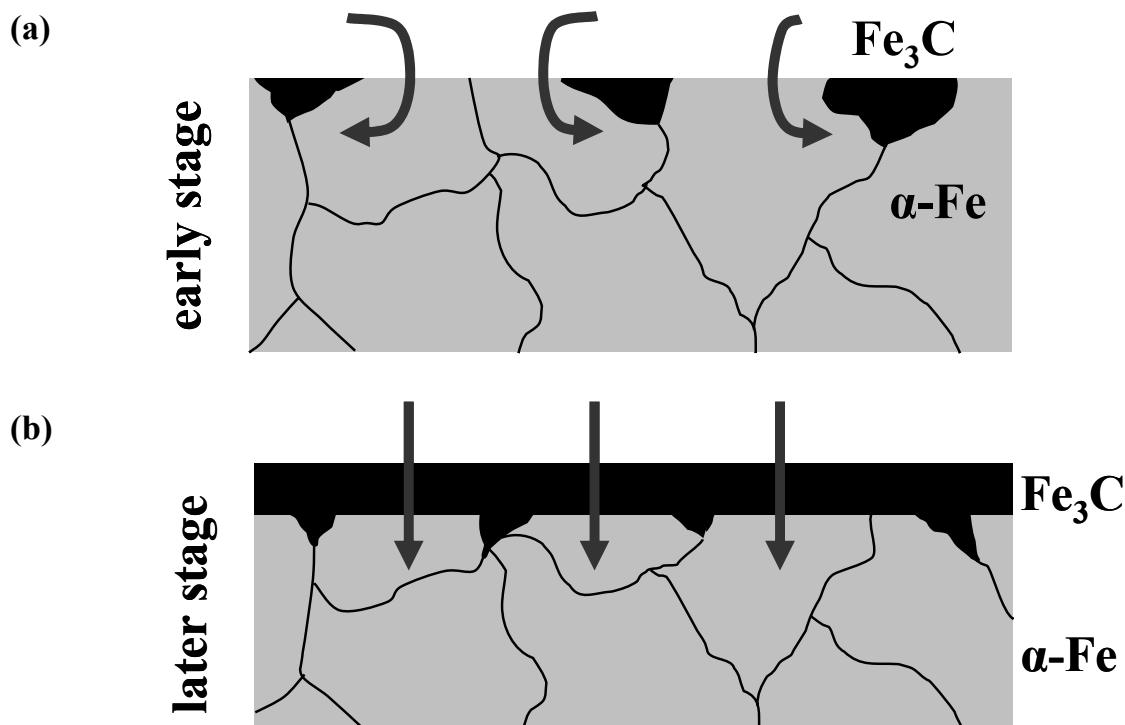


**Fig. 1.6:** Two-stage process of cementite-layer growth. (a) In the early stage of cementite formation only a few cementite crystallites will have formed on ferrite. Carbon diffusion through ferrite, bypassing cementite occurs since carbon diffusion through ferrite will be faster than carbon diffusion through cementite. This early stage will be followed by a stage where carbon will diffuse through thin and defect-rich parts of the now completely closed cementite layer (short-circuit diffusion). (b) In the later stage, carbon volume diffusion through cementite will occur which will lead to parabolic cementite-layer growth.

Due to the Arrhenius-type temperature dependence of the obtained parabolic growth constants, an “apparent” activation energy for cementite-layer growth will be determined and the different influence factors on this “apparent” activation energy will be analysed and discussed in detail (cf. *chapter 3*).

### **1.3.2 Orientation relationships of cementite and ferrite and the consequences**

In the literature, several works are dealing with the orientation relationship of cementite and ferrite [41-48]. Different orientation relationships, mostly found in pearlite, were proposed to pertain for cementite and ferrite [49-54]. Until now, there are no works reported in the literature dealing with the orientation relationship between the cementite grains of a compound layer and the ferrite grains of the underlying substrate and orientation relationship between neighboured cementite grains of a compound layer.

In *chapter 4* of this work, a detailed study of the cementite/ferrite orientation relationships will be performed by means of electron backscatter diffraction (EBSD) and it will be found that the Bagaryatsky orientation relationship [50] holds between the cementite grains of the compound layer and the ferrite grains of the substrate. Furthermore, preference of specific variants of this orientation relationship will be indicated by the experimental data. This will be ascribed to low misfit-strain energy for favoured orientation variants as compared to high misfit-strain energy for unfavoured orientation variants. According to the Bagaryatsky orientation relationship [50] it will be shown that low-energy grain boundaries will be expected between adjacent cementite grains on the same ferrite-substrate grain. In contrast, high-energy grain boundaries will occur between neighboured cementite grains on adjacent ferrite-substrate grains. These high-energy cementite grain boundaries will promote carbon grain boundary diffusion through the cementite. This will experimentally be evidenced by larger cementite-layer thicknesses at the location of ferrite-grain boundaries intersecting the substrate surface.

### **1.3.3 Diffusivity of nitrogen and activation energy of nitrogen diffusion in cementite**

Up to now there aren't any works in the literature which report either on the diffusivity of nitrogen or the activation energy of nitrogen diffusion in cementite. In order to make this information available, in *chapter 5* of this work hardness-depth profile



measurements will be performed in the ferrite substrate with a growing cementite layer of time-dependent thickness on top at different treatment temperatures. Nitrogen will diffuse through the cementite and the underlying ferrite substrate will get enriched with interstitial nitrogen. Upon embedding the specimens, which can be regarded as heat treatment,  $\alpha''$ -Fe<sub>16</sub>N<sub>2</sub> precipitates will be formed in the ferrite [6-10], which will be responsible for a considerable hardness increase of the ferrite substrate. The hardness increase is a measure for the nitrogen content in the ferrite. On the basis of additional measurements by chemical analysis, a calibration line will be constructed with which such hardness-depth profiles will be transformed into nitrogen concentration-depth profiles. By the help of a developed model using the implicit finite-difference method, simulated nitrogen concentration-depth profiles will be obtained. These simulated profiles will be accommodated to the experimentally determined nitrogen concentration-depth profiles by minimising the sum of the squared differences between simulated and experimental values. The simulation will yield, for the first time, information about the diffusivity of nitrogen through cementite and the activation energy of nitrogen diffusion in cementite. The activation energy for nitrogen diffusion in cementite will be relatively low, which will be explained on the basis of nitrogen grain-boundary diffusion through cementite.

#### 1.3.4 New information on the Fe–N–C system

In the past, several studies were carried out which have dealt with the constitution of the ternary phase diagram Fe–N–C [26,55-62], either directly based on experiments or on the basis of evaluations of experimental data adopting thermodynamic models. To date, in these literature works, the existence of the two-phase region  $\alpha$ -Fe +  $\epsilon$ -Fe<sub>3</sub>(N,C)<sub>1+x</sub> itself and the temperature range at which it occurs were discussed controversially. According to the works which favour occurrence of this two-phase region, it opens after passing the invariant transition reaction  $\gamma'$ -Fe<sub>4</sub>N + Fe<sub>3</sub>C  $\rightarrow$   $\alpha$ -Fe[N,C] +  $\epsilon$ -Fe<sub>3</sub>(N,C)<sub>1+x</sub> at a single temperature. In some works [63-70], also  $\epsilon$ -Fe<sub>3</sub>(N,C)<sub>1+x</sub> was obtained in direct contact with ferrite. However,

the corresponding authors did not state the presence of a two-phase region  $\alpha\text{-Fe} + \varepsilon\text{-Fe}_3(\text{N,C})_{1+x}$ , they only quoted kinetic reasons.

In *chapter 6* of the present work it will be shown experimentally by nitrocarburising reactions and systematic secondary annealing experiments that the two-phase region  $\alpha\text{-Fe} + \varepsilon\text{-Fe}_3(\text{N,C})_{1+x}$  exists. Furthermore, the temperature of the invariant transition reaction mentioned above will be investigated experimentally. It will be demonstrated that the EBSD method is a powerful tool for the investigation of the constitution of compound-layer microstructures. The results which will be presented in *chapter 6* will give new insight into the constitution of the ternary phase diagram Fe–N–C and will also have pronounced technical importance.

### 1.3.5 Elastic constants of cementite

Although cementite-containing steels are common in technical and industrial applications, there is a lack of fundamental knowledge on the mechanical properties of cementite. Due to difficulties in preparing single-phase polycrystalline cementite specimens, the experimental (single-crystal) elastic constants of cementite are yet unknown. Therefore, it is not possible to analyse the elastic response of e.g. cementite containing steels to mechanical deformation. Very recently the full set of nine independent elastic constants of orthorhombic cementite, provided by first-principles calculations, was reported in the literature [71].

In *chapter 7* of the present work, the results of *first-principles* calculations yielding the full set of nine independent elastic constants of cementite as a function of pressure will be presented. The results of these calculations will indicate extreme elastic anisotropy of cementite with a very small  $c_{44}$  as compared to  $c_{55}$  and  $c_{66}$ . This extreme elastic anisotropy of cementite will be evidenced experimentally by synchrotron X-ray diffraction stress measurements on cementite layers on ferrite substrates, produced as will be reported in *chapter 2*.

## References

- [1] C.H. Knerr, T.C. Rose, J.H. Filkowski, in: J.R. Davis, G.M. Davidson, S.R. Lampman, T.B. Zorc, J.L. Daquila, A.W. Ronke, K.L. Henniger, R.C. Uhl (Eds.): ASM Handbook, vol. 4, Heat Treating, ASM International (1991) 387.
- [2] M.A.J. Somers: Heat Treat. Met. 27 (2000) 92.
- [3] D. Liedtke, U. Baudis, J. Boßlet, U. Huchel, H. Klümper-Westkamp, W. Lerche, H.J. Spieß: Wärmebehandlung von Eisenwerkstoffen – Nitrieren und Nitrocarburieren, Expert-Verlag, Renningen Malsheim (2006).
- [4] E.J. Mittemeijer: J. Heat Treating 3 (1983) 114.
- [5] P.M. Unterweiser, A.G. Gray (Eds.): Source Book on Nitriding, ASM, Metals Park, OH (1977).
- [6] E. Kubalek: Härtereit Tech. Mitt. 23 (1968) 177.
- [7] D.H. Jack, K.H. Jack: Mat. Sci. Eng. 11 (1973) 1.
- [8] Y. Inokuti, N. Nishida, N. Ōhashi: Metall. Trans. A 6A (1975) 773.
- [9] U. Dahmen, P. Ferguson, K.H. Westmacott: Acta Metall. 35 (1987) 1037.
- [10] Z.Q. Liu, Y.X. Chen, Z.K. Hei, D.X. Li, H. Hashimoto: Metall. Mater. Trans. A 32A (2001) 2681.
- [11] T. Bell: Heat Treat. Met. 2 (1975) 39.
- [12] C. Dawes, D.F. Tranter: Heat Treat. Met. 3 (1985) 70.
- [13] P.F. Colijn, E.J. Mittemeijer, H.C.F. Rozendaal: Z. Metallkd. 74 (1983) 620.
- [14] M.A.J. Somers, E.J. Mittemeijer: Surf. Eng. 3 (1987) 123.
- [15] T. Gressmann, M. Nikolussi, A. Leineweber, E.J. Mittemeijer: Scr. Mat. 55 (2006) 723.
- [16] H.J. Grabke: Mater. Corr. 54 (2003) 736.
- [17] A. Schneider, H. Viehhaus, G. Inden, H.J. Grabke, E.M. Müller-Lorenz: Mater. Corr. 49 (1998) 336.
- [18] D. Moszynski, H.J. Grabke, A. Schneider: Surf. Inter. Analys. 34 (2002) 380.
- [19] H.J. Grabke, D. Moszynski, E.M. Müller-Lorenz, A. Schneider: Surf. Inter. Anal. 34 (2002) 369.

- [20] A. Schneider, H.J. Grabke: *Mater. Corr.* 54 (2003) 793.
- [21] T. Sone, E. Tsunasawa, K. Yamanaka: *Trans. Jap. Inst. Met.* 22 (1981) 237.
- [22] Toyota Jidoshi K.K., Toyota Aichi, JP (H. Nonoyama, T. Fukuizumi, A. Morita), Japanese Patent P58-122201 (1983/07/05).
- [23] M. Umemoto, Y. Todaka, T. Takahashi, P. Li, R. Tokumiya, K. Tsuchiya: *J. Metast. Nanocryst. Mater.* 15 (2003) 607.
- [24] E. Carpenne, P. Schaaf: *Appl. Phys. Lett.* 80 (2002) 891.
- [25] H. Mizubayashi, S.J. Li, H. Yumoto, M. Shimotomai: *Scr. Mat.* 40 (1999) 773.
- [26] F. K. Naumann, G. Langenscheid: *Arch. Eisenhüttenwesen* 36 (1965) 583.
- [27] E.J. Mittemeijer, J.T. Slycke: *Surf. Eng.* 12 (1996) 152.
- [28] E.J. Mittemeijer, M.A.J. Somers: *Surf. Eng.* 13 (1997) 483.
- [29] L. Maldzinski, Z. Przylecki, J. Kunze: *J. Steel. Res.* 57 (1986) 645.
- [30] M.A.J. Somers, E.J. Mittemeijer: *Metall. Mater. Trans. A* 26A (1995) 57.
- [31] B.J. Kooi, M.A.J. Somers, E.J. Mittemeijer: *Metall. Mater. Trans. A* 27A (1996) 1063.
- [32] E. Lehrer: *Z. Elektrochem.* 36 (1930) 383.
- [33] R. Hoffmann: *Härtere Tech. Mitt.* 51 (1996) 5.
- [34] H.J. Grabke: *Arch. Eisenhüttenw.* 46 (1975) 75.
- [35] M. Nikolussi, A. Leineweber, E.J. Mittemeijer: submitted for publication.
- [36] L. Torchane, P. Bilger, J. Dulcy, M. Gantios: *Metall. Mater. Trans. A* 27A (1996) 1823.
- [37] K. Schwerdtfeger, P. Grieveson, E.T. Turkdogan: *Trans. TMS AIME* 245 (1969) 2461.
- [38] C. Middendorf, W. Mader: *Z. Metallkd.* 94 (2003) 333.
- [39] A. Schneider, G. Inden, H.J. Grabke, in: M. Rühle, H. Gleiter (Eds.): *Interface Controlled Materials (Euromat 99)*, Wiley-VCH, Weinheim (2000).
- [40] A. Schneider: *Corr. Sci.* 44 (2002) 2353.
- [41] D.N. Shackleton, P.M. Kelly: *Acta Metall.* 15 (1967) 979.
- [42] D.S. Zhou, G.J. Shiflet: *Metall. Trans. A* 23A (1992) 1259.
- [43] M.A. Mangan, G.J. Shiflet: *Metall. Mater. Trans. A* 30A (1999) 2767.
- [44] D.V. Shtansky, K. Nakai, Y. Ohnkori: *Phil. Mag.* 79 (1999) 1655.

- [45] R.J. Dippenaar, R.W.K. Honeycombe: Proc. R. Soc. London A 333 (1973) 455.
- [46] D.H. Jack: Mat. Sci. Eng. 13 (1974) 19.
- [47] G. Spanos: Metall. Trans A 23A (1992) 171.
- [48] T. Takahashi, D. Ponge, D. Raabe: Steel Res. Int. 78 (2007) 38.
- [49] I.V. Isaichev: Zh. Tekh. Fiz. 17 (1947) 835.
- [50] Y. A. Bagaryatsky: Dokl. Akad. Nauk. SSSR 73 (1950) 1161.
- [51] N.J. Petch: Acta Cryst. 6 (1953) 96.
- [52] W. Pitch: Acta Metall, 10 (1962) 79.
- [53] L.S. Darken, R.M. Fisher: Decomposition of Austenite by Diffusional Processes, ed. V.F. Zackay, H.I. Aaronson, Interscience, New York (1962) 249.
- [54] A.J. Baker, P.M. Kelly, J. Nutting: Electron Microscopy and Strength of Crystals, Interscience, New York (1961) 899.
- [55] K.H. Jack: Proc. Roy. Soc. A 195 (1948) 41.
- [56] V. Raghavan: Trans. Indian Inst. Met. 37 (1984) 293.
- [57] X. Zuyao, L. Lin: Mat. Sci. Tec. 3 (1987) 325.
- [58] J. Slycke, L. Sproge, J. Ågren: Scand. J. Metallurgy 17 (1988) 122.
- [59] H. Du, M. Hillert: Z. Metallkde. 82 (1991) 310.
- [60] U. Huchel, J. Kunze: Härterei-Tech. Mitt. 46 (1991) 351.
- [61] H. Du: J. Phase Eq. 14 (1993) 682.
- [62] J. Kunze: Härterei-Tech. Mitt. 51 (1996) 348.
- [63] D. Gérardin, H. Michel, J.P. Morniroli, M. Gantois: Mémoires Sci. Rev. Mét. 77 (1977) 457.
- [64] D. Gérardin, H. Michel, M. Gantois: Scr. Metall. 11 (1977) 557.
- [65] J. Matauschek, H. Trenkler: Härterei-Tech. Mitt. 32 (1977) 4.
- [66] M.A.J. Somers, P.F. Colijn, W.G. Sloof, E.J. Mittemeijer: Z. Metallkd. 81 (1990) 33.
- [67] E.J. Mittemeijer, W.T.M. Straver, P.F. Colijn, P.J. van der Schaaf, J.A. van der Hoeven: Scr. Metall. 14 (1980) 1189.
- [68] A. Wells, T. Bell: Heat Treat. Metals (1983) 39.
- [69] A. Wells: Thin Sol. Films 128 (1985) L33.
- [70] A. Wells: J. Mat. Sci. 20 (1985) 2439.

- [71] C. Jiang, S.G. Srinivasan, A. Caro, S.A. Maloy: J. Appl. Phys. 103 (2008) 043502.

***Formation of massive cementite layers on iron by ferritic carburising in the additional presence of ammonia***

*T. Greßmann, M. Nikolussi, A. Leineweber, E.J. Mittemeijer*

**Abstract**

Massive Fe<sub>3</sub>C compound layers were grown on  $\alpha$ -Fe substrates at 823 K by a gas carburising process in the additional presence of NH<sub>3</sub>. Whereas pure carburising employing a CO/H<sub>2</sub>/N<sub>2</sub> gas mixture leads, besides Fe<sub>3</sub>C formation, to severe graphite formation, the latter can be suppressed by a partial substitution of N<sub>2</sub> in the gas mixture by NH<sub>3</sub>. The growth kinetics of the obtained massive Fe<sub>3</sub>C layers can be described by a two-stage process.

## 2.1 Introduction

Improvement of the mechanical and chemical properties of iron and iron-based workpieces is often realised by the application of surface layers. Such layers can for example be produced by gaseous nitriding/nitrocarburising [1]. These thermochemical surface treatments are widely applied in order to improve the corrosion and wear resistance as well as the fatigue endurance [2]. Thereby, nitrocarburising is the most versatile surface treatment for ferritic steels.

Upon conventional gaseous nitrocarburising (e.g. by annealing in ammonia and carbonmonoxide containing gas mixtures at temperatures below 853 K) nitrogen and carbon are provided simultaneously to an iron-based surface by atmospheres possessing nitrogen and carbon chemical potentials sufficiently high to form compound layers composed of iron-(carbo-)nitrides. These compound layers are usually composed of an outer  $\varepsilon$ -Fe<sub>3</sub>(N,C)<sub>1+x</sub> sublayer adjacent to the surface and an inner  $\gamma'$ -Fe<sub>4</sub>N sublayer adjacent to the layer/substrate interface. The presence of a carbon delivering species in the gas mixture promotes the formation of the  $\varepsilon$  phase which can dissolve considerable amounts of carbon [3,4], which is not the case for the  $\gamma'$  phase.

Until now, only a few systematic investigations on the dependence of the constitution of the compound layer on the gas composition have been performed for high chemical potentials of carbon (as provided by e.g. relatively high CO contents in the gas atmosphere) and for the concurrent presence of ammonia [1,4-6]. It has been reported that in nitrocarburising atmospheres, with high chemical potentials of carbon, besides (carbo-)nitrides also cementite can form, leading to complex compound-layer microstructures [1,6]. The nitrocarburising process can even be accompanied by sooting of the surface, if very high CO contents in the gas mixture are applied [4,5]. Graphite formation is also associated with 'metal dusting', i.e. disintegration of the surface of iron-based work pieces in carburising atmospheres due to the decomposition of cementite into iron and graphite [7].



The present work demonstrates for the first time that it is possible to grow massive cementite surface layers on  $\alpha$ -Fe by carburising (with CO) in the *presence* of ammonia in the gas atmosphere. Ammonia has been found to be decisive for the suppression of sooting and metal dusting which occur in the *absence* of ammonia. The influence of the ammonia content in the atmosphere has been systematically examined. For a selected atmospheric composition the growth kinetics of the cementite surface layer has been evaluated. Such massive cementite layers may be used for applications where corrosion resistant and very hard ( $\text{Fe}_3\text{C} \sim 1000 \text{ HV}$  [8]) surface layers are needed and the properties of the bulk have to be retained.

## 2.2 Experimental procedure

### 2.2.1 Specimen preparation and thermochemical treatment

An iron (Alfa Aesar, 99.98 wt.%) cast rod was cold rolled to a plate of about 1 mm thickness and cut into rectangular pieces (20 mm  $\times$  25 mm). Before (nitro-)carburising these specimens were recrystallised for 2 h at 973 K under hydrogen, mechanically polished (final stage 1  $\mu\text{m}$  diamond) and cleaned ultrasonically in ethanol.

The (nitro-)carburising treatment was performed in a vertical quartz tube furnace equipped with a water container for quenching. The process temperature of 823 K was controlled within  $\pm 1 \text{ K}$  at the position of the sample. The (nitro-)carburising atmosphere was composed of carbon monoxide (99.97 vol.%) as carbon supply, hydrogen (99.999 vol.%), ammonia (99.999 vol.%) as nitrogen supply and nitrogen (99.999 vol.%) as inert gas<sup>2.1</sup>. The flow rate of each gas was controlled with mass flow controllers. The overall flow rate of the gas mixture through the quartz retort (diameter 28 mm) was with  $13.5 \text{ mm s}^{-1}$  (for the gas volume at room temperature) sufficiently high to minimise the effect of reactions changing the composition of the gas phase, e.g. ammonia decomposition. For all experiments, the CO and H<sub>2</sub> contents in the gas mixture were kept constant at 20.0 vol.% and 58.0 vol.%, respectively, whereas the content of ammonia and inert nitrogen gas as well as the process time were variable.

---

<sup>2.1</sup> At atmospheric pressure and at the process temperature N<sub>2</sub> does not dissociate and hence does not react with solid iron.

After the thermochemical heat treatment the specimens were quenched in water at room temperature flushed with N<sub>2</sub>.

**Table 2.1:** Composition of the gas mixtures applied for experiment series *A*, with constant volume fractions of 20.0 vol.% CO and 58.0 vol.% H<sub>2</sub>; the nitriding potential  $r_N = p_{\text{NH}_3} / p_{\text{H}_2}^{3/2}$ ; the phases observed and the optical appearance of the surface after the treatments at 823 K for 4 h and 24 h, see also Fig. 2.3.

NH <sub>3</sub> [vol.%]	N <sub>2</sub> [vol.%]	$r_N$ [atm <sup>-1/2</sup> ]	Phases observed by XRD	Appearance of the surface
22.0 <sup>a</sup>	0	0.5	ε, γ', Fe <sub>3</sub> C	matt grey
17.6	4.4	0.4	Fe <sub>3</sub> C	shiny
13.2	8.8	0.3	Fe <sub>3</sub> C	shiny
6.6	15.4	0.15	Fe <sub>3</sub> C, graphite	partially sooted
3.3 <sup>a</sup>	18.7	0.075	Fe <sub>3</sub> C, graphite	partially sooted
1.7 <sup>a</sup>	20.3	0.0375	Fe <sub>3</sub> C, graphite	black
0	22.0	0	Fe <sub>3</sub> C, graphite	black

<sup>a</sup>treatment only for 4 h

Two series of experiments were performed: for series *A* treatment times of 4 h and 24 h and variable ammonia and nitrogen gas contents (22.0–*n* vol.% NH<sub>3</sub>, *n* vol.% N<sub>2</sub>) were applied (Table 2.1, where also corresponding values of the nitriding potential<sup>2.2</sup>,  $r_N = p_{\text{NH}_3} / p_{\text{H}_2}^{3/2}$  [9], have been gathered), whereas for series *B* constant volume fractions for NH<sub>3</sub> and N<sub>2</sub> were applied (13.2 vol.% and 8.8 vol.%, respectively) with treatment times varying from 5 min to 48 h.

### 2.2.2 Analysis of the (nitro-)carburised specimens

The thermochemically treated specimens were cut into two pieces, which were used for optical microscopy and X-ray diffraction (XRD), respectively. The piece used for

<sup>2.2</sup> The nitriding potential  $r_N$  is commonly used to quantify the chemical potential of nitrogen in NH<sub>3</sub>/H<sub>2</sub> gas mixtures, which is considerable higher than that of molecular N<sub>2</sub> [9].

light microscopical investigation was covered with an electrodeposited protective nickel layer by using a Watts bath [10] (at 333 K) in order to avoid curvature and damaging close to the surface of the specimen during subsequent metallographic handling. Next, the piece was embedded (Polyfast, Buehler GmbH) and ground and polished (final step: 1  $\mu\text{m}$  diamond paste). After etching in 1 vol.% Nital containing 0.1 vol.% HCl [1,6,11] some cross sections were stained either with a Murakami solution (1 g NaOH, 1 g KOH and 4 g  $\text{KMnO}_4$  per 100 ml distilled water) at 333 K or with an alkaline sodium picrate solution (25 g NaOH and 2 g picric acid per 75 ml distilled water) at room temperature. The staining occurred selectively on the carbon containing phases, i.e. here  $\epsilon\text{-Fe}_3(\text{N,C})_{1+x}$  and  $\text{Fe}_3\text{C}$  [12,13]. Light optical microscopy was performed with a Leica DMRM microscope. For each specimen several cross-sectional micrographs were taken close to both faces of the specimen. The cementite surface-layer thickness was determined from these micrographs: the measured area of the layer was divided by the measured lateral length of the layer, yielding the layer thickness. The values of several micrographs were arithmetically averaged.

For phase identification X-ray diffraction analysis was applied by recording diffractograms from the surface of the second piece of the original specimen, using a PANalytical X'Pert MP diffractometer (CoK $\alpha$  radiation), equipped with a graphite monochromator in the diffracted beam and employing Bragg-Brentano geometry. During the measurements the specimen pieces were rotated around the surface normal to achieve better crystallite statistics. For lattice-parameter determination Si standard powder suspended in isopropanol was deposited as a thin layer on the surface of the specimen in order to calibrate the diffraction angle.

Quantitative Electron Probe Micro Analysis (EPMA) was performed employing a Cameca SX100 instrument to determine the carbon and nitrogen contents in the compound layer. To this end the intensities of the N-K $\alpha$ , C-K $\alpha$  and Fe-K $\alpha$  radiations, excited by an incident 10 keV electron beam, were measured simultaneously. Before the measurement started, oxygen was blown at each location onto the cross section for 40 s while the electron beam was switched on in order to remove carbon contamination, which would otherwise obscure the C-K $\alpha$  intensity stemming from the carbon present in the material probed [14]. The K $\alpha$  intensities of nitrogen, carbon and

iron were compared with the corresponding intensities of  $\gamma'$ -Fe<sub>4</sub>N, Fe<sub>3</sub>C and pure iron standards. Concentration values were calculated from the intensity ratios applying the  $\Phi(\rho z)$  approach [15].

## 2.3 Results and discussion

### 2.3.1 Influence of the ammonia content in the atmosphere on the layer constitution

At the highest NH<sub>3</sub> content in the gas atmosphere (22.0 vol.%), the outer, visual appearance of the specimen of experiment series *A* (Table 2.1) is similar to that of conventionally nitrided surfaces: matt grey. The microstructure of the developed compound layer is rather complex (Fig. 2.1a) as compared to the microstructure of the compound layer developed by pure nitriding of iron [16]. Comparing the results of XRD and light microscopical investigation after Murakami staining, it appears that the outer part of the layer consists predominantly of  $\epsilon$ -Fe<sub>3</sub>(N,C)<sub>1+x</sub> and cementite (both stained), the latter phase exhibiting sometimes a needle-like morphology. The unstained part of the compound layers - adjacent to the substrate - is identified as  $\gamma'$ -Fe<sub>4</sub>N. The thickness of the overall compound layer is quite irregular. At regions where more cementite is present the total compound-layer thickness is smaller than at regions consisting predominantly of  $\gamma'$ -Fe<sub>4</sub>N (Fig. 2.1a). This suggests that cementite hinders the diffusion of nitrogen and carbon as compared to  $\epsilon$ -Fe<sub>3</sub>(N,C)<sub>1+x</sub>/ $\gamma'$ -Fe<sub>4</sub>N layers.

For lower ammonia contents in the gas atmosphere (17.6 and 13.2 vol.% NH<sub>3</sub>) the sample surface remains metallicly shiny (Fig. 2.2b) as prior to nitrocarburising (Fig. 2.2a). Optical microscopy on the cross sections and XRD analysis revealed that the microstructure of the compound layers changes upon decreasing the ammonia content in the gas mixture from multiphase to monophasic layers consisting only of cementite (Fig. 2.1b). These compound layers are of much more homogeneous thickness and are also thinner than in the above discussed case where iron (carbo-) nitrides are also present. EPMA demonstrated that the carbon content in these layers is 25 at.%, corresponding to the formula Fe<sub>3</sub>C. Nitrogen could not be detected, which is

in agreement with previously reported values for the maximum, marginal solubility of nitrogen in  $\text{Fe}_3\text{C}$  [17]. This is, in any case, much lower than the nitrogen detection limit of the EPMA technique. X-ray diffraction analysis was used to determine the lattice parameters of the cementite phase in these layers. The observed lattice parameters of orthorhombic cementite,  $a = 5.0936 \pm 0.0006 \text{ \AA}$ ,  $b = 6.7685 \pm 0.0008 \text{ \AA}$ ,  $c = 4.5310 \pm 0.0008 \text{ \AA}$  ( $Pnma$  setting), are larger than those reported in literature [18]. One has to recognise that these values were determined with the diffraction vector perpendicular to the surface. Therefore, the too large values for the lattice parameters can be explained as the consequence of the presence of compressive stresses parallel to the surface within the compound layers, as confirmed by additional X-ray stress measurements.

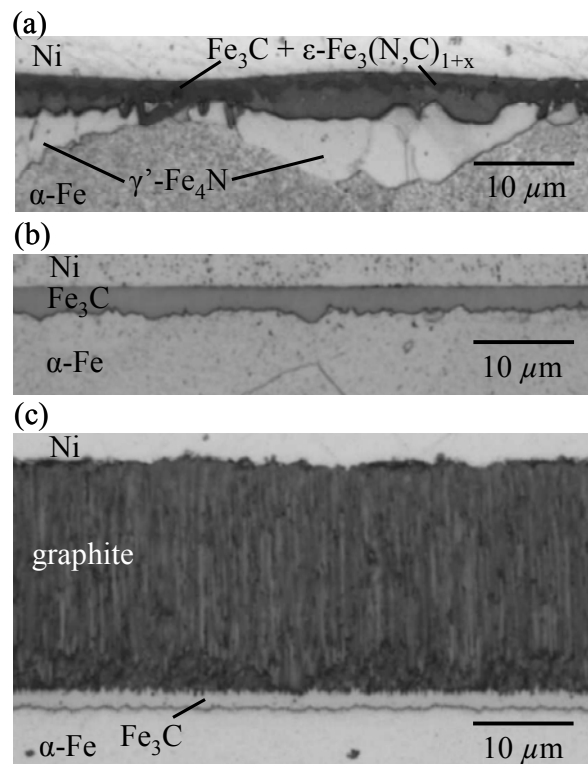


**Fig. 2.1:** Optical micrographs (bright field) showing cross sections of compound layers obtained on  $\alpha\text{-Fe}$  specimens by (nitro-)carburising at 823 K for 4 h after Nital etching; Applied gas mixture consisting of 20.0 vol.%  $\text{CO}$ , 58.0 vol.%  $\text{H}_2$  and (a) 22.0 vol.%  $\text{NH}_3$  (after additional Murakami staining; showing a complex microstructure, consisting of  $\epsilon\text{-Fe}_3(\text{N,C})_{1+x}$  and cementite (both stained) near the surface and  $\gamma'\text{-Fe}_4\text{N}$  adjacent to the substrate), (b) 13.2 vol.%  $\text{NH}_3$ , 8.8 vol.%  $\text{N}_2$  (after additional staining with picrate; showing a single  $\text{Fe}_3\text{C}$  layer) and (c) 22.0 vol.%  $\text{N}_2$  ( $\text{Fe}_3\text{C}$  layer slightly stained with picrate; the  $\text{Fe}_3\text{C}$ /graphite interface is roughened due to metal dusting).

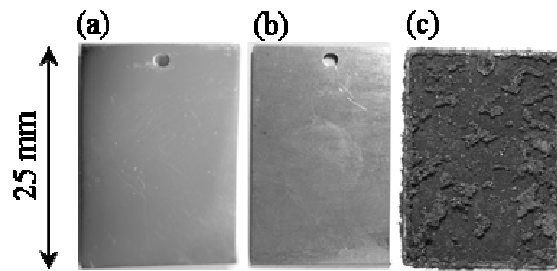


**Fig. 2.2:** Photographs of the  $\alpha$ -Fe samples (a) before (nitro-)carburising, (b) after (nitro-)carburising in a 13.2 vol.%  $\text{NH}_3$ , 58.0 vol.%  $\text{H}_2$ , 20.0 vol.%  $\text{CO}$ , 8.8 vol.%  $\text{N}_2$  gas mixture exhibiting a cementite layer and (c) after carburising in a 58.0 vol.%  $\text{H}_2$ , 20 vol.%  $\text{CO}$ , 22.0 vol.%  $\text{N}_2$  gas mixture (severely sooted).

Further reduction of the ammonia content in the gas atmosphere (down to values  $\leq 6.6$  vol.%  $\text{NH}_3$ ) leads to the formation of soot (graphite) on the surface of the samples, which is easily recognised visually since the surface becomes black (Fig. 2.2c). The degree of sooting *increases* with *decreasing*  $\text{NH}_3$  content in the gas atmosphere. In the extreme case of no ammonia in the atmosphere, the surface is severely sooted. The cross-sectional micrograph (Fig. 2.1c) reveals that the outer surface adjacent part of the specimen is composed of graphite. A relatively thin cementite layer remains adjacent to the substrate. The presence of both cementite and graphite is confirmed by XRD. During the (nitro-)carburising process the former surface of the sample, which is now the interface between  $\text{Fe}_3\text{C}$  and graphite, has become quite rough as a result of disintegration of  $\text{Fe}_3\text{C}$  on the iron surface caused by metal dusting (Fig. 2.1c).

The addition of different amounts of ammonia to the carburising gas atmosphere does not only affect the microstructure/constitution of the compound layer, but also the cementite-layer thickness. The higher the ammonia content, the thicker the cementite layer becomes. The relation between the ammonia content in the gas mixture and the corresponding cementite-layer thickness for treatment times of 4 h and 24 h as well as the approximate ammonia-content range where pure, massive cementite layers can be generated are shown in Fig. 2.3.

Indications that nitrogen delivering species in the gas atmosphere can suppress carbon deposition on an iron-based surface have also been made in the case of an ‘ion-softnitriding’ study on steels in  $\text{CH}_4/\text{H}_2/\text{N}_2$  gas mixtures<sup>2,3</sup> [19], however, without giving details. Furthermore, some observations in Ref. [20], where deformed Fe–Cr–Ti alloys were exposed to strongly carburising gas mixtures composed of  $\text{C}_3\text{H}_8$ ,  $\text{C}_4\text{H}_{10}$  and  $\text{NH}_3$  at 853 K, can also be interpreted such that ammonia suppresses the formation of graphite on the surface of the specimen.

In order to explain the possible role of ammonia in preventing sooting, one could think of substitution of some carbon in the cementite by nitrogen, which might reduce the chemical potential of carbon in  $\text{Fe}_3\text{C}$  so that it may become less unstable with respect to decomposition in Fe and graphite. However, the solubility of nitrogen in cementite is extremely low (EPMA results reported above and see Ref. [17]). A possible, more likely explanation could be that nitrogen at the gas/solid interface kinetically suppresses the formation of graphite there. Here it should be mentioned that the presence of gaseous  $\text{H}_2\text{S}$  in strongly carburising gas mixtures also suppresses metal dusting:  $\text{H}_2\text{S}$  is adsorbed at the surface and hence reduces the number of adsorption sites for CO at the iron surface [21]. However,  $\text{H}_2\text{S}$  in particular hinders carbon to enter the solid and to form cementite, whereas ammonia only prevents sooting, but still allows carbon to enter the substrate, according to the results of the present study.

The presence of ammonia even appears to accelerate the carbon absorption, as evidenced by the observed layer-growth rate (increasing layer-growth rate with increasing ammonia content in the atmosphere; see Fig. 2.3). A faster absorption of carbon in the presence of a nitrogen providing media has been observed also in the case of the austenitic carbonitriding processes [22].

---

<sup>2,3</sup> In the ion-nitriding process  $\text{N}_2$  is activated and thus can be used for nitriding reactions, whereas this is not possible in the conventional gaseous nitriding/nitrocarburising process (see footnote 2.1).

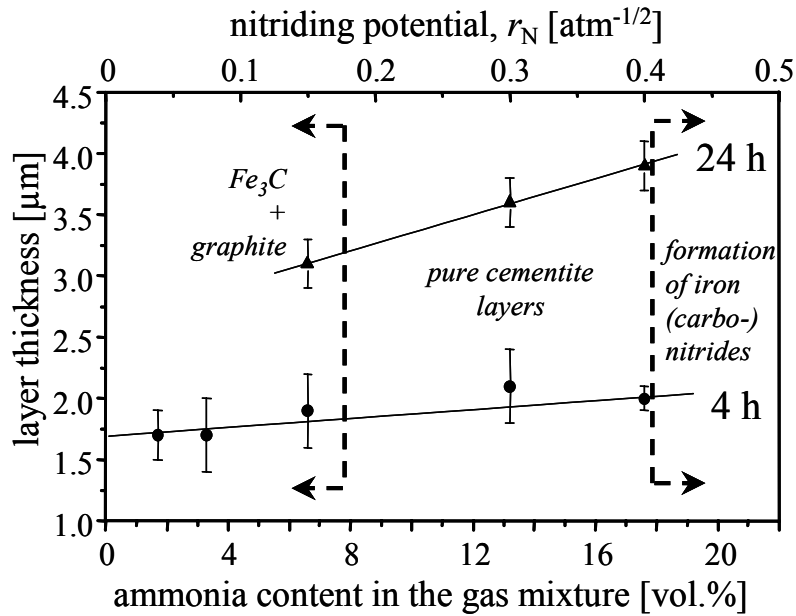


**Fig. 2.3:** Dependence of the cementite layer-thickness on the ammonia content for 4 h and 24 h treatments at 823 K in gas mixtures consisting of 20.0 vol.% CO, 58.0 vol.% H<sub>2</sub>, 22.0 –  $n$  vol.% NH<sub>3</sub> and  $n$  vol.% N<sub>2</sub>. The approximate ranges for the formation of pure cementite layers, cementite layers accompanied by sooting and the region where layers consisting of cementite and iron (carbo-) nitrides are formed have been indicated.

The following consideration may explain how ammonia enhances the cementite layer-growth rate by an accelerated carbon uptake. The heterogeneous carbon uptake reactions are [7]<sup>2.4</sup>:



These are total reactions, which can be subdivided in steps. The CO dissociation can be written as



<sup>2.4</sup> The initial gas mixtures composed of CO/H<sub>2</sub>/NH<sub>3</sub>/N<sub>2</sub>, as applied in this work, are not in equilibrium at the nitrocarburising temperature, since several homogeneous and heterogeneous reactions involving e.g. CO<sub>2</sub>, H<sub>2</sub>O, CH<sub>4</sub> can occur. The chemical potential of carbon,  $\mu_C$ , is initially hypothetically infinite with respect to reactions (2.1) and (2.2), because initially  $p_{\text{CO}_2} = p_{\text{H}_2\text{O}} = 0$ .



and may thus be conceived as the first step of reactions (2.1) and (2.2). The removal of the adsorbed oxygen due to reaction (2.3) can occur for total reaction (2.1) according to:



and for total reaction (2.2) according to



Since reaction (2.5) is considerable faster than reaction (2.4) [7], reaction (2.2) may provide the dominant pathway for the carbon uptake. The hydrogen needed for removal of the oxygen according to reaction (2.5) can be provided by the hydrogen in the gas atmosphere but also by the decomposition of ammonia:



leading to the total reaction:



Reaction (2.7) may play a crucial role to realise the growth of massive cementite layers, additionally to reaction (2.2), because, it provides an extra possibility for carbon transfer from the atmosphere to the solid. However, the nitriding potential (i.e. the chemical potential of nitrogen  $\mu_{\text{N}}$ ) must be sufficiently low in order to prevent the formation of iron (carbo-) nitrides.

### 2.3.2 Cementite layer-growths kinetics

To analyse the cementite layer-growth kinetics, the specimens of experiment series *B* were treated with a constant  $\text{NH}_3$  content of 13.2 vol.% ( $r_{\text{N}} = 0.3 \text{ atm}^{-1/2}$ ) in order to achieve massive cementite layers without sooting or the formation of iron-nitrides (cf. Fig. 2.3). Results of series *B* are shown in Fig. 2.4 where the squared cementite-layer thickness  $S^2$  has been plotted versus the treatment time  $t$ .

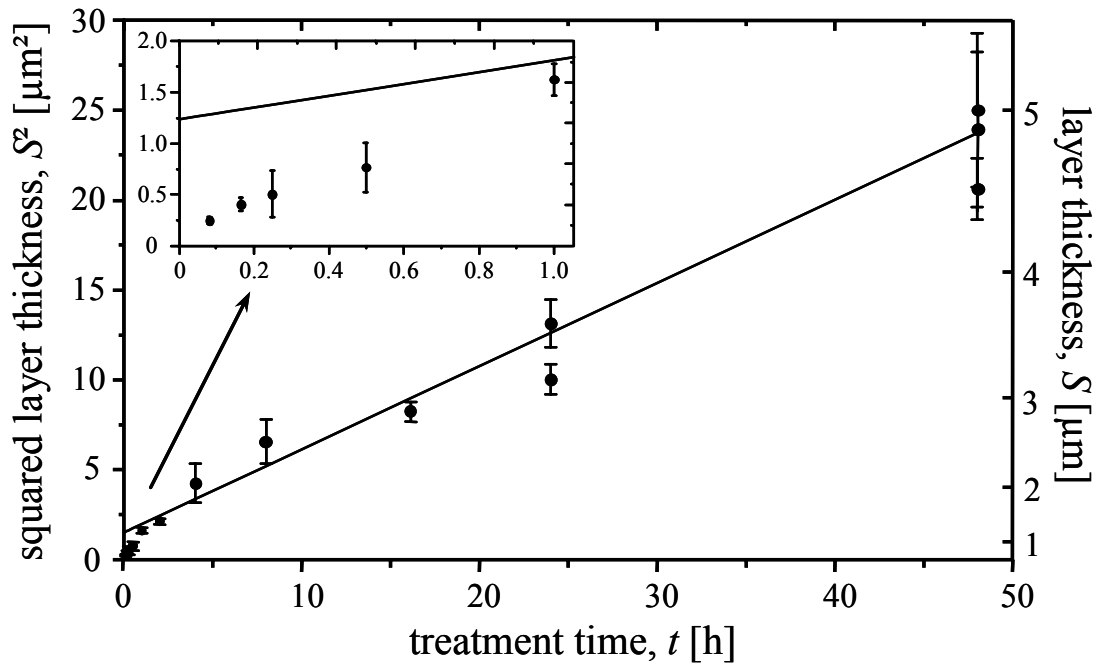


**Fig. 2.4:** The squared cementite-layer thickness versus the (nitro-) carburising time at 823 K for treatment in a gas mixture composed of 20.0 vol.% CO, 58.0 vol.% H<sub>2</sub>, 13.2 vol.% NH<sub>3</sub>, and 8.8 vol.% N<sub>2</sub> ( $r_{\text{N}} = 0.3 \text{ atm}^{-1/2}$ ). The straight line shown for stage II ( $t > 1 \text{ h}$ ) has been obtained by least-squares fitting of Eq. (2.8).

Occurrence of (carbon) volume-diffusion controlled growth would lead to a straight line through the origin in that plot. Clearly, for treatment times larger than 1 h parabolic, volume-diffusion controlled growth occurs, whereas for the shorter treatment times a faster growth rate occurs.

The initial, fast layer growth (stage I) may be caused by two effects. At the very beginning of the carburising treatment an incomplete, only fractionally closed cementite layer may be present and carbon can diffuse through ferrite (bypassing the cementite), which is much faster than the diffusion of carbon through the cementite (a similar bypassing effect has been discussed for  $\gamma'$ -Fe<sub>4</sub>N-layer growth on iron [16]). This ‘bypass’ growth mechanism can, in any case, contribute until, upon lateral growth, the cementite crystallites coalesce and form a continuous layer. Already after 5 min a complete cementite layer was observed. Thereafter, carbon diffusion may preferentially occur through especially thin and defect-rich parts of the just completed cementite layer with a high grain-boundary density (short-circuit diffusion).

Thus carbon could be transported relatively fast through the layer, as compared to volume diffusion.

Upon longer treatment times cementite crystallites may coarsen and/or defects become annihilated, leading to a microstructure not allowing substantial short-circuit diffusion, and thus the layer-growth rate decreases and becomes controlled by volume diffusion. Analysing the layer-thickness data as a function of time for  $t > 1$  h (stage II) in terms of

$$S^2(t) = kt + S_0^2, \quad (2.8)$$

with  $S_0$  as the hypothetical thickness at  $t = 0$  and  $k$  as the parabolic growth constant leads to values for  $S_0$  and  $k$  by (least-squares) fitting of a straight line through the data in Fig. 2.4. Thus an ‘initial’ layer thickness of about  $1.2 \mu\text{m}$  ( $S_0 > 0$ , because of the ‘bypass/short-circuit’ mechanism) and a growth constant of  $1.3 \times 10^{-16} \text{ m}^2/\text{s}$  were determined for the given carburising parameters. Comparison of the growth rate of the cementite layer with that of a  $\gamma'$ -Fe<sub>4</sub>N layer at the same temperature [9] indicates that the cementite layer grows much slower, leading to thinner compound layers at comparable treatment times.

## 2.4 Conclusions

1. Pure and massive cementite layers can be grown onto ferritic iron by carburising in gas atmospheres containing a certain amount of ammonia. The ammonia content in the atmosphere (consisting of 20 vol.% CO, 58 vol.% H<sub>2</sub>, 22 –  $n$  vol.% NH<sub>3</sub> and  $n$  vol.% N<sub>2</sub>) controls the phase composition of the compound layer: In a certain range of ammonia content the growth of cementite layers can be easily controlled, as required for practical applications. A too high amount of ammonia leads to the formation of iron (carbo-) nitrides, whereas a too low amount of ammonia leads to sooting at the surface.
2. Examination of the growth kinetics of the cementite layers revealed a two-stage process. In the beginning stage of cementite formation ( $t < 1$  h at 823 K) relatively fast layer growth occurs, which may be ascribed to e.g. (i) a fractionally complete

cementite layer ('bypassing' diffusion of carbon through ferrite) and (ii) short-circuit diffusion due to many defects such as cementite grain boundaries within the initially very thin layer. After that beginning stage of layer growth, massive cementite-layer growth obeys a parabolic, (likely carbon volume) diffusion-controlled growth law.

## References

- [1] M.A.J. Somers, E.J. Mittemeijer: *Surf. Eng.* 3 (1987) 123.
- [2] P.M. Unterweiser, A.G. Gray (Eds.): *Source Book on Nitriding*, ASM, Metals Park, OH (1977).
- [3] K.H. Jack: *Proc. Roy. Soc. A* 195 (1948) 41.
- [4] F.K. Naumann, G. Langenscheid: *Arch. Eisenhüttenwes.* 36 (1965) 583.
- [5] F.K. Naumann, G. Langenscheid: *Arch. Eisenhüttenwes.* 36 (1965) 677.
- [6] H. Du, M.A.J. Somers, J. Ågren: *Met. Trans. A* 31A (2000) 195.
- [7] H.J. Grabke: *Mater. Corr.* 54 (2003) 736.
- [8] M. Umemoto, Y. Todaka, T. Takahashi, P. Li, R. Tokumiya, K. Tsuchiya: *J. Metastab. and Nanocryst. Mat.* 15-16 (2003) 607.
- [9] E.J. Mittemeijer, M.A.J. Somers: *Surf. Eng.* 13 (1997) 483.
- [10] R. Chatterjee-Fischer, R. Bodenhausen, F.-W. Eysell, R. Hoffmann, D. Liedtke, H. Mallener, W. Rembges, A. Schreiner, G. Welker: *Wärmebehandlung von Eisenwerkstoffen*, Expert-Verlag, Renningen-Malmsheim (1995).
- [11] A. Wells: *J. Mat. Sci.* 20 (1985) 2439.
- [12] P.F. Colijn, E.J. Mittemeijer, H.C.F. Rozendaal: *Z. Metallkde.* 74 (1983) 620.
- [13] H.C.F. Rozendaal, P.F. Colijn, E.J. Mittemeijer: *Surf. Eng.* 1 (1985) 30.
- [14] D. Schalkoord: *M.Sc. Thesis*, Delft University of Technology (1973).
- [15] J.L. La Pouchau, F. Pichoir: *Rech. Aerospatial* 3 (1984) 167.
- [16] M.A.J. Somers, E.J. Mittemeijer: *Met. Trans. A* 26A (1995) 57.
- [17] A. Kagawa, T. Okamoto: *Trans. Japan Inst. Met.* 22 (1981) 137.

- [18] I.G. Wood, L. Vočadlo, K.S. Knight, D.P. Dobson, W.G. Marshall, G.D. Price, J. Brodholt: *J. Appl. Crystallogr.* 82 (2004) 37.
- [19] T. Sone, E. Tsunasawa, K. Yamanaka: *Trans. Japan Inst. Met.* 22 (1981) 237.
- [20] L. Demchenko, S. Sidorenko, V. Tinyaev: *Def. Diff. Forum* 216-217 (2003) 87.
- [21] A. Schneider, H.J. Grabke: *Mater. Corr.* 54 (2003) 793.
- [22] R.J. Cowan, J.T. Bryce: *Trans. Amer. Soc. Metals* 26 (1938) 766.



***Growth of massive cementite layers;  
thermodynamic parameters and kinetics***

*M. Nikolussi, A. Leineweber, E.J. Mittemeijer*

**Abstract**

Massive, pure cementite layers were grown on ferrite substrates by nitrocarburising in a dedicated  $\text{NH}_3/\text{H}_2/\text{CO}/\text{N}_2$  containing gas atmosphere at temperatures in the range of 783 K - 843 K. From the parabolic layer-growth constants an “apparent” activation energy for cementite-layer growth of  $109 \pm 12$  kJ/mol was obtained. This “apparent” activation energy can be subdivided into a positive contribution due to the activation energy for (tracer-)diffusion of carbon in cementite and a negative contribution due to the temperature dependence of the difference of the carbon activity in cementite at the surface and the carbon activity in cementite at the interface cementite/ferrite.

### 3.1 Introduction

Cementite,  $\text{Fe}_3\text{C}$ , is, besides ferrite, the major constituent of plain carbon and mildly alloyed steels. Notwithstanding its great technological importance, little is known about the intrinsic properties of cementite. This dearth of fundamental knowledge on cementite is mainly due to the difficulty in preparing single-phase (single- or polycrystalline) cementite specimens. In the past, several works dealt with the production of bulk cementite specimens applying different methods [1-5]. Yet, only recently, it was reported for the first time that massive cementite layers can be grown on ferrite substrates by a dedicated gaseous nitrocarburising process [6] (cf. *chapter 2*). The addition of ammonia to the carburising gas mixture was found to be decisive for the suppression of both the formation of graphitic soot and the disintegration of cementite once formed (metal dusting).

Gaseous nitrocarburising of iron or iron-based alloys is a thermochemical heat treatment usually performed at temperatures between 773 K and 853 K below the ternary eutectoid temperature of the Fe–N–C solid solution [7]. By this process, which gathered great technical importance during the last decades [8,9], nitrogen and carbon delivered by the gas phase are diffusively incorporated into the surface-region of the iron-based workpiece [7].

This results in (i) the formation of a compound layer (several 10  $\mu\text{m}$  thick) containing, depending on the treatment temperature (and pressure) and the composition of the gas atmosphere, different phases, typically  $\gamma'$ - $\text{Fe}_4\text{N}_{1-y}$  and  $\epsilon$ - $\text{Fe}_3(\text{N,C})_{1+x}$  [10], but sometimes, under certain circumstances, also cementite [6,11] (cf. *chapter 2*), and (ii) the formation of a diffusion zone (several 100  $\mu\text{m}$  thick), enriched with interstitial nitrogen (and carbon). Whereas the compound layer is responsible for a considerable enhancement of the corrosion and wear resistance, the diffusion zone enhances the fatigue endurance [12].

The present work focuses on an analysis of cementite-layer growth kinetics. Massive cementite layers were grown on ferrite substrates in the treatment-temperature range of 783 K - 843 K, thus extending the preceding study [6] (cf. *chapter 2*) in



which only experiments at  $T = 823$  K were conducted. The experimental values for the (temperature dependence of the) parabolic growth constant were determined. These results were evaluated in terms of an “apparent” activation energy for cementite-layer growth and discussed with reference to previous work on the kinetics of cementite (layer) growth [4,13-19]. The discrepancy between the results of the present work and the literature data are discussed in terms of thermodynamic consequences of the different gas atmospheres used.

### **3.2 Experimental**

Pure iron foils (20 mm × 25 mm) were produced by cold rolling a ferrite cast rod (Alfa Aesar, 99.98 wt.-% Fe) on both sides to a thickness of 1 mm. The specimens to be nitrocarburised were cut from this cold-rolled plate, ground, polished (final stage 1 μm diamond suspension) and cleaned ultrasonically in ethanol. Prior to the nitrocarburising process, the specimens were recrystallised at 973 K for 2 h under a hydrogen flow of 200 ml min<sup>-1</sup>, polished (final stage 1 μm diamond suspension) and cleaned ultrasonically in ethanol.

Gaseous nitrocarburising was carried out in a vertical quartz-tube furnace. To retain solid states produced at the nitrocarburising temperature, the quartz-tube furnace was equipped at its end with a water (flushed with N<sub>2</sub>) container for quenching the specimens to room temperature. The iron foils were suspended on a quartz fibre and positioned in the middle of the furnace where the process temperature prevailed, controlled within ± 1 K. In order to quench the specimens to room temperature, the quartz fibre was destroyed by a mechanical device and the specimen dropped into the water container. The gas atmosphere was composed of 13 vol.-% ammonia (99.999 vol.-% purity) as a nitrogen-providing medium, 58 vol.-% hydrogen (99.999 vol.-% purity), 20 vol.-% carbon monoxide (99.97 vol.-% purity) as a carbon-providing medium and 9 vol.-% nitrogen (99.999 vol.-% purity) as inert gas; each gas flux was controlled by a mass-flow controller. In order to ensure that ammonia dissociation, which would change the composition of the gas atmosphere, can be neglected, an

overall linear flow rate of  $13.5 \text{ mm s}^{-1}$  (calculated for the gas volume at room temperature) through the quartz retort (diameter 28 mm) was maintained.

Four sets of nitrocarburising experiments were performed at  $T = 783 \text{ K}$ ,  $803 \text{ K}$ ,  $823 \text{ K}$  and  $843 \text{ K}$  (the data for  $T = 823 \text{ K}$  were already reported in a preceding study [6]; cf. *chapter 2*) for different treatment times in the range of 5 min – 48 h.

After gaseous nitrocarburising and quenching, the specimens were cut into two pieces, one used for optical microscopy and one used for X-ray diffraction (XRD).

In order to avoid mechanical damage at the surface of the specimen (parts) used for metallographic analysis and to ensure a sufficient sharpness at the specimen surface in the cross sections, the specimens were covered with a protective nickel layer electrodeposited at  $333 \text{ K}$  using a Watts bath [10,20]. Thereafter, the specimens were embedded (Polyfast, Buehler GmbH), ground, polished (final stage  $1 \mu\text{m}$  diamond suspension) and etched using 1 vol.% Nital containing 0.1 vol.% HCl [21]. To improve the optical contrast between the massive cementite layer and the ferrite substrate, the cross-sectional specimens were additionally stained using either an alkaline potassium permanganate solution (1 g NaOH, 1 g KOH and 4 g  $\text{KMnO}_4$  per 100 ml distilled water) at  $328 \text{ K}$  [6,22] (cf. *chapter 2*) of which the effect is similar to that of a Murakami solution [10,22] or an alkaline sodium picrate solution (25 g NaOH and 2 g picric acid per 75 ml distilled water) at room temperature [22]. By these procedures, the massive cementite layer gets, due to its high carbon content, severely stained and can therefore easily be distinguished upon light optical microscopy from the ferrite substrate which remains unstained. Light optical microscopy was performed using a Zeiss Axiophot microscope.

For the determination of the cementite-layer thickness several micrographs were taken from each specimen. From these micrographs the area of the massive cementite layer was measured and divided through its lateral length, yielding, after averaging the experimental values obtained from several micrographs, the cementite-layer thickness.

Phase identification was carried out by X-ray diffraction to verify the presence of a massive cementite layer on the ferrite substrate. A PANalytical X'Pert Multi-Purpose Diffractometer equipped with a graphite monochromator in the diffracted beam, utilising  $\text{CoK}\alpha$  radiation and Bragg-Brentano geometry, was used.

To achieve better crystallite statistics the specimens were rotated during the measurements around their surface normal.

### 3.3 Results and evaluation

All experiments performed led to the formation of massive cementite layers on the ferrite substrates (cf. Fig. 3.1).

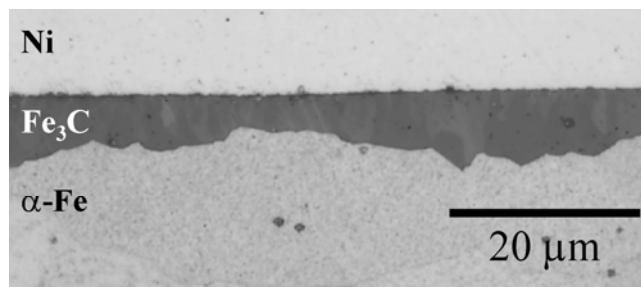


**Fig. 3.1:** Light optical microscopic image of a metallographic cross-section after etching with 1 vol.-% Nital containing 1 vol.-% HCl and staining with an alkaline sodium picrate solution. The massive cementite layer (stained) was grown on the ferrite substrate (unstained) by gaseous nitrocarburising at 823 K for 48 h using a gas atmosphere containing 13 vol.-% NH<sub>3</sub>, 58 vol.-% H<sub>2</sub> (nitriding potential  $r_N = 0.3 \text{ atm}^{-1/2}$ ), 20 vol.-% CO and 9 vol.-% N<sub>2</sub> (as inert gas).

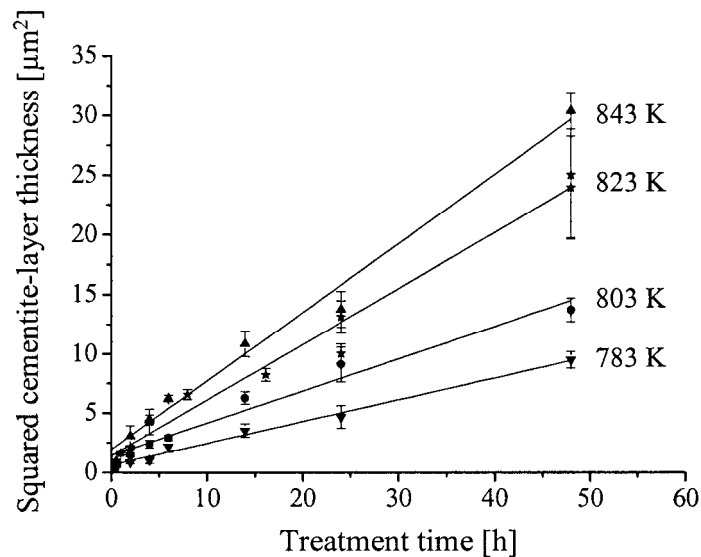


**Fig. 3.2:** Squared cementite-layer thickness vs. treatment time at 783 K, 803 K, 823 K and 843 K, using a gas atmosphere composed of 13 vol.-% NH<sub>3</sub>, 58 vol.-% H<sub>2</sub> (nitriding potential  $r_N = 0.3 \text{ atm}^{-1/2}$ ), 20 vol.-% CO and 9 vol.-% N<sub>2</sub>. The straight lines represent least-squares fitting of Eq. (3.1) for the different treatment temperatures to the respective experimental data ( $t > 1 \text{ h}$ ) yielding the growth constant  $k$  and the hypothetical initial cementite-layer thickness  $S_0$  (cf. Table 3.1).

The squared value of the experimentally determined cementite-layer thickness (cf. section 3.2) was plotted vs. the treatment time at the various temperatures (cf. Fig. 3.2). Occurrence of parabolic layer growth from  $t = 0$  onwards is given by a straight line through the origin of the plot of the squared layer thickness versus time (cf. Fig. 3.2). Such a simple parabolic layer growth was assumed for treatment times larger than 1 h. Evidently, as follows from the data in Fig. 3.2, for treatment times  $t < 1$  h cementite-layer growth occurred faster than indicated by such a parabolic relation. This can be discussed as follows.

At the beginning of the cementite formation, an incompletely closed cementite layer can occur. Hence, carbon can diffuse through ferrite to the (also bottom tip of the) cementite grains growing from the surface (this diffusion through ferrite is much faster than diffusion through cementite), thus bypassing the cementite. Further, shortly after establishment of a closed cementite layer, short-circuit diffusion of carbon may occur through thin and defect-rich parts of the cementite layer, exhibiting a relatively high grain-boundary density. Both ‘bypass/short-circuit’ mechanisms for carbon lead to relatively fast cementite growth as compared to later stages (cf. Ref. [6]; *chapter 2*). The initial ‘bypass/short-circuit’ mechanism involves that the parabolic cementite-layer growth law pertaining to later stages of cementite-layer growth has to be modified by introducing a hypothetical initial cementite-layer thickness  $S_0 (> 0)$  at  $t = 0$ . Hence, the time-dependence of the cementite-layer growth is given by

$$S^2(t) = kt + S_0^2 \quad (\text{for } t > 1 \text{ h}), \quad (3.1)$$

where  $S$  denotes the cementite-layer thickness,  $k$  the growth constant and  $t$  the treatment time.

Least-squares fitting of Eq. (3.1) to the experimental data at the four treatment temperatures for  $t > 1$  h (cf. Fig. 3.2) yielded the results for the growth constant and the hypothetical initial cementite-layer thickness shown in Table 3.1.

**Table 3.1:** Experimentally determined growth constants  $k$  and hypothetical initial cementite-layer thicknesses  $S_0$  at four different treatment temperatures  $T = 783$  K, 803 K, 823 K and 843 K. The results were obtained by least-squares fitting of Eq. (3.1) to the respective experimental data (cf. Fig. 3.2).

treatment temperature [K]	growth constant [m <sup>2</sup> /s]	initial cementite-layer thickness [m]
783	$(5.1 \pm 0.2) \cdot 10^{-17}$	$(0.79 \pm 0.09) \cdot 10^{-6}$
803	$(7.6 \pm 0.6) \cdot 10^{-17}$	$(1.20 \pm 0.14) \cdot 10^{-6}$
823	$(1.3 \pm 0.7) \cdot 10^{-16}$	$(1.19 \pm 0.16) \cdot 10^{-6}$
843	$(1.6 \pm 0.8) \cdot 10^{-16}$	$(1.39 \pm 0.16) \cdot 10^{-6}$

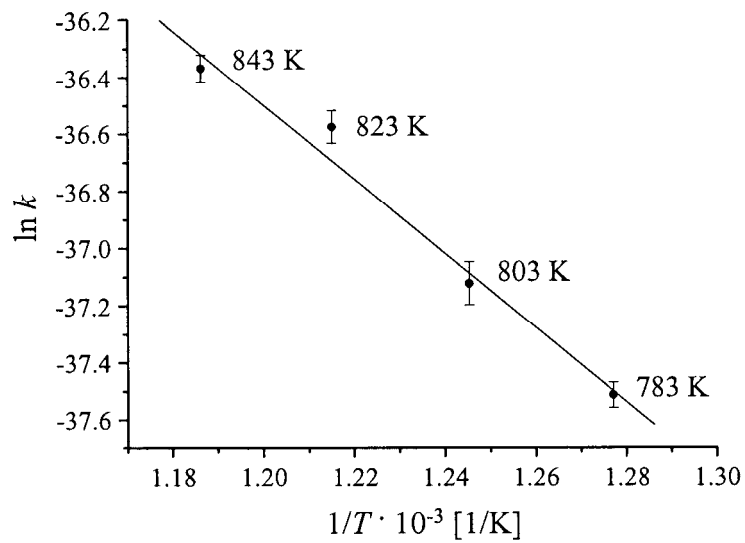


**Fig. 3.3:** Arrhenius plot: natural logarithm of the growth constant  $k$  versus the inverse treatment temperature  $1/T$ . The „apparent“ activation energy of the cementite-layer growth can be calculated from the slope of the straight line which was obtained by least-squares fitting of Eq. (3.2) to the experimental data.

An Arrhenius-type temperature dependence is adopted for the growth constant  $k$

$$k = k_0 \exp\left(-\frac{Q_{\text{app}}}{RT}\right), \quad (3.2)$$

where  $k_0$  denotes a preexponential factor,  $Q_{\text{app}}$  is an „apparent“ activation energy of cementite-layer growth,  $R$  is the gas constant and  $T$  is the treatment temperature. Then, a plot of the logarithm of the growth constant vs. the inverse treatment temperature should yield a straight line. Such linear dependence is observed indeed (cf. Fig. 3.3), validating the application of Eq. (3.2) (see also section 3.4.3). The slope of the plot,  $m = -Q_{\text{app}}/R$ , yields an “apparent“ activation energy equal to  $109 \pm 12$  kJ/mol.

## 3.4 Discussion

### 3.4.1 Parabolic layer growth for interstitial compounds

In the literature the growth kinetics of pure iron nitride layers [23-26] but also of cementite layers [4,15,16] was described by a parabolic growth law. A comparison of the rates of cementite-layer growth and  $\gamma'$ -Fe<sub>4</sub>N<sub>1-y</sub>-layer growth indicates that, at the same temperature,  $\gamma'$ -Fe<sub>4</sub>N<sub>1-y</sub>-layer growth proceeds faster than cementite-layer growth, which can be ascribed to nitrogen volume diffusion in  $\gamma'$ -Fe<sub>4</sub>N<sub>1-y</sub> being faster than carbon volume diffusion in cementite.

Parabolic layer growth according to Eq. (3.1) with  $S_0 = 0$  is expected in particular for close-to-stoichiometric interstitial compounds like  $\gamma'$ -Fe<sub>4</sub>N and cementite if the following general assumptions are valid [18,27]: (a) local equilibrium at the interface gas atmosphere/specimen surface; (b) local equilibrium at the interface compound layer/ferrite substrate; (c) a completely closed, massive compound layer; i.e. nitrogen/carbon mass transport proceeds exclusively via nitrogen/carbon (volume) diffusion through the massive compound layer.

If these conditions hold, the parabolic growth constant is proportional to the product of (i) the (tracer)diffusion coefficient of nitrogen/carbon<sup>3.1</sup> in the compound layer,  $D^*$  - diffusion of the metal component (iron) can generally be neglected [29] - and of (ii) a function  $f(\Delta a)$  (taken as time-independent) which increases monotonously with the difference of the activity of nitrogen/carbon in the solid at the surface,  $a^{\text{surface}}$ , and the activity of nitrogen/carbon in the solid at the interface layer/substrate,  $a^{\text{interface}}$ <sup>3.2</sup>.

$$k \propto D^* f(\Delta a) \quad (3.3)$$

with

$$\Delta a = a^{\text{surface}} - a^{\text{interface}} \quad (3.4)$$

According to the assumption of local equilibrium at the surface (see above), the activity  $a^{\text{surface}}$  is determined by the composition of the gas atmosphere, and is controlled as described in section 3.4.2. According to the assumption of local equilibrium at the layer/substrate interface, the activity  $a^{\text{interface}}$  is compatible with the corresponding phase boundary in the ternary phase diagram Fe–N–C.

### 3.4.2 Thermodynamics of gaseous nitrocarburising

Upon exposing the ferrite substrates to the  $\text{NH}_3/\text{H}_2/\text{CO}/\text{N}_2$ -containing gas atmosphere, N and C are introduced into the solid, where  $\text{NH}_3$  and CO act as the nitrogen and carbon providing media<sup>3.3</sup>.

---

<sup>3.1</sup> It was shown that, due to cementite layer/ferrite substrate misfit-strain development, specific crystallographic directions of cementite,  $[uvw]_{\text{C}}$  with  $w$  large, occur parallel to the surface normal of the specimen [28] (cf. *chapter 4*). The diffusion data for carbon presented in this work pertain to these directions.

<sup>3.2</sup> For details concerning the dependence of  $k$  on the activities  $a^{\text{surface}}$  and  $a^{\text{interface}}$  with respect to the operating diffusion mechanism see Ref. [18].

<sup>3.3</sup> At atmospheric pressure and at the applied treatment temperatures  $\text{N}_2$  does not react with solid iron; it can be regarded as an inert gas.

Since *thermal* decomposition of  $\text{NH}_3$  as well as decomposition of (metastable) iron nitrides are slow, transfer of nitrogen from the gas atmosphere into the specimen can be described by the following heterogeneous chemical equilibrium:



where  $[\text{N}]$  denotes nitrogen either dissolved in the ferrite substrate (solid solution) or in iron nitride. The chemical potential  $\mu_{\text{N}}^{\text{surface}}$  and the activity  $a_{\text{N}}^{\text{surface}}$  of nitrogen dissolved in the solid at the surface (assumed to be in equilibrium with the gas atmosphere) obey:

$$\mu_{\text{N}}^{\text{surface}} = \frac{1}{2} \mu_{\text{N}_2}^0 + RT \ln a_{\text{N}}^{\text{surface}} = \mu_{\text{NH}_3}^0 - \frac{3}{2} \mu_{\text{H}_2}^0 + RT \ln \left( r_{\text{N}} (p^0)^{\frac{1}{2}} \right), \quad (3.6)$$

where  $\mu_{\text{N}_2}^0$ ,  $\mu_{\text{NH}_3}^0$  and  $\mu_{\text{H}_2}^0$  are the chemical potentials of nitrogen, ammonia and hydrogen in the gaseous reference state (pressure  $p^0 = 1$  atm) and  $r_{\text{N}} = \frac{p_{\text{NH}_3}}{p_{\text{H}_2}^{3/2}}$  denotes the so-called nitriding potential, where  $p_{\text{NH}_3}$  and  $p_{\text{H}_2}$  are the partial pressures of ammonia and hydrogen in the gas atmosphere. Hence, according to Eq. (3.6), the nitriding potential<sup>3,4</sup> of the gas atmosphere at the surface fixes the chemical potential and the activity of nitrogen in the solid at the surface [31]. It follows that the activity  $a_{\text{N}}^{\text{surface}}$  of nitrogen dissolved in the solid at the surface (assumed to be in equilibrium with the gas atmosphere) obeys:

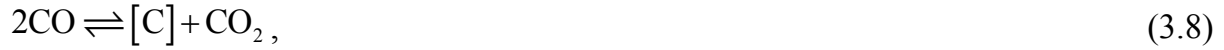
$$a_{\text{N}}^{\text{surface}} = \exp \left( - \frac{\frac{1}{2} \mu_{\text{N}_2}^0 + \frac{3}{2} \mu_{\text{H}_2}^0 - \mu_{\text{NH}_3}^0}{RT} \right) (p^0)^{1/2} r_{\text{N}}. \quad (3.7)$$

---

<sup>3,4</sup> In the present experiments a nitriding potential of  $r_{\text{N}} = 0.3 \text{ atm}^{-1/2}$  was applied (cf. section 3.2) which, in absence of CO, would lead to the formation of a  $\gamma\text{-Fe}_4\text{N}_{1-y}$  compound layer [30].



Transfer of carbon from the gas atmosphere into the specimen is associated with the presence of CO in the gas atmosphere and can proceed via the, in principle potentially carburising, heterogeneous Boudouard equilibrium:



and the so-called heterogeneous water-gas equilibrium



where [C] denotes carbon dissolved either in the ferrite substrate (solid solution) or in cementite. The hydrogen necessary for the chemical equilibrium given by Eq. (3.9) is delivered by the H<sub>2</sub>-containing gas atmosphere. The chemical potentials  $\mu_{\text{C},(3.8)}^{\text{surface}}$  and  $\mu_{\text{C},(3.9)}^{\text{surface}}$  and the activities  $a_{\text{C},(3.8)}^{\text{surface}}$  and  $a_{\text{C},(3.9)}^{\text{surface}}$  of carbon dissolved in the solid at the surface (assumed to be in equilibrium with the gas atmosphere according to either Eq. (3.8) or Eq. (3.9)) obey:

$$\mu_{\text{C},(3.8)}^{\text{surface}} = \mu_{\text{C}}^0 + RT \ln a_{\text{C}}^{\text{surface}} = 2\mu_{\text{CO}}^0 - \mu_{\text{CO}_2}^0 + RT \ln \left( r_{\text{C},(3.8)} (p^0)^{-1} \right), \quad (3.10)$$

and

$$\mu_{\text{C},(3.9)}^{\text{surface}} = \mu_{\text{C}}^0 + RT \ln a_{\text{C}}^{\text{surface}} = \mu_{\text{CO}}^0 + \mu_{\text{H}_2}^0 - \mu_{\text{H}_2\text{O}}^0 + RT \ln \left( r_{\text{C},(3.9)} (p^0)^{-1} \right), \quad (3.11)$$

where  $\mu_{\text{C}}^0$  is the chemical potential of graphite in the reference state (pressure  $p^0 = 1$  atm) and  $\mu_{\text{CO}}^0$ ,  $\mu_{\text{CO}_2}^0$ ,  $\mu_{\text{H}_2}^0$  and  $\mu_{\text{H}_2\text{O}}^0$  are the chemical potentials of carbon monoxide, carbon dioxide, hydrogen and water in the gaseous reference state (pressure  $p^0 = 1$  atm) and  $r_{\text{C},(3.8)} = \frac{p_{\text{CO}}^2}{p_{\text{CO}_2}}$  and  $r_{\text{C},(3.9)} = \frac{p_{\text{CO}} p_{\text{H}_2}}{p_{\text{H}_2\text{O}}}$  denote the so-called carburising potentials according to the equilibria given by Eqs. (3.8) and (3.9), where  $p_{\text{CO}}$ ,  $p_{\text{CO}_2}$ ,  $p_{\text{H}_2}$  and

$p_{\text{H}_2\text{O}}$  are the partial pressures of carbon monoxide, carbon dioxide, hydrogen and water in the gas atmosphere. The carburising potential fixes, similar to the nitriding potential (see above), the chemical potential and the activity of carbon in the solid at the surface. It follows that the activity  $a_{\text{C},(i)}^{\text{surface}}$  of carbon in the solid at the surface (assumed to be in equilibrium with the gas atmosphere) obeys for the equilibria given by Eqs. (3.8) and (3.9) ( $i = 3.8, 3.9$ ):

$$a_{\text{C},(3.8)}^{\text{surface}} = \exp\left(-\frac{\mu_{\text{C}}^0 + \mu_{\text{CO}_2}^0 - 2\mu_{\text{CO}}^0}{RT}\right) (p^0)^{-1} r_{\text{C},(3.8)}, \quad (3.12)$$

and

$$a_{\text{C},(3.9)}^{\text{surface}} = \exp\left(-\frac{\mu_{\text{C}}^0 + \mu_{\text{H}_2\text{O}}^0 - \mu_{\text{CO}}^0 - \mu_{\text{H}_2}^0}{RT}\right) (p^0)^{-1} r_{\text{C},(3.9)}, \quad (3.13)$$

For each of the equilibria given by Eqs. (3.8) and (3.9) a separate carbon activity in the solid at the surface can be calculated. The heterogeneous water-gas equilibrium (Eq. (3.9)) is much faster established than the Boudouard equilibrium (Eq. (3.8)) [32]. Therefore, the heterogeneous water-gas equilibrium (Eq. (3.9)) is considered to control the carburising.

In general, in case of equilibrium with the nitrocarburising gas atmosphere, the carbon activity in the solid at the surface complies with the occurrence of simultaneous equilibrium for all possible reactions in the gas atmosphere. Thus, the equilibria given by Eqs. (3.14) – (3.16), have to be considered as well:



In the present experiments neither CO<sub>2</sub> (cf. Eq. (3.8)) nor H<sub>2</sub>O (cf. Eq. (3.9)) were initially present in the nitrocarburising gas atmosphere ( $p_{\text{CO}_2} = p_{\text{H}_2\text{O}} = 0$ ). Hence, the carbon activity according to either Eq. (3.12) or Eq. (3.13) equals (hypothetically) infinity.

No soot formation occurred in the present experiments. Further, as discussed in section 3.4.1, local equilibrium (or at least a stationary state) at the interface gas atmosphere/specimen surface is a prerequisite for parabolic (cementite) layer growth as observed in this work. It is concluded that in the present experiments a finite carbon activity appears to rule in the solid at the surface. Such a finite, “effective” carbon activity can prevail if e.g. due to the chemical reaction according to Eq. (3.15), a certain amount of water is produced. The stationary presence of this amount of water induces a specific finite, “effective” carbon activity in the solid at the surface according to the heterogeneous water-gas equilibrium (cf. Eq. (3.13)). The value of this “effective” carbon activity at the surface can be estimated using literature data (see what follows in section 3.4.3).

### 3.4.3 Interpretation of the “apparent” activation energy

Values reported for the activation energy of carbon volume diffusion in metal carbides range from about 125 kJ/mol up to 230 kJ/mol [29]; for cementite activation energy values of 154 kJ/mol [18] and 163-185 kJ/mol [13,14]<sup>3.5</sup> have been reported. These values differ considerably with the value of  $109 \pm 12$  kJ/mol determined in the present work for the “apparent” activation energy. This difference arises because in the previous works, e.g. Refs. [13,14], the carbon activities in the solid at the surface and at the interface with the substrate were known and accounted for in the determination

---

<sup>3.5</sup> It should be noted that this data was *not* determined on the basis of growth-rate dependence on temperature. The (tracer)diffusion coefficient of carbon in cementite,  $D_C^*$ , was determined for only a single temperature. The activation energy for carbon volume diffusion in cementite was then calculated adopting the Arrhenius equation for the diffusion coefficient of carbon in cementite,  $D_C^*$ , employing two different values for the preexponential factor  $D_{0,C}^*$  for general, interstitial diffusion within metals from the literature.

of  $D_C^*$  and its activation energy. In the present work the value of the carbon activity in the solid at the surface is not known directly (cf. section 3.4.2), but can be derived indirectly.

The “apparent” activation energy value equal to  $109 \pm 12$  kJ/mol was determined by Arrhenius-type analysis (see Fig. 3.3 in section 3.3). The slope of the straight line in the plot of the logarithm of the growth constant vs. the inverse treatment temperature (cf. Fig. 3.3) depends on the temperature dependences of both  $D_C^*$  (which is certainly of Arrhenius-type) and  $f(\Delta a_C)$ .  $f(\Delta a_C)$  varies under the present experimental conditions strongly as a function of the treatment temperature due to the treatment temperature-dependent “effective”  $a_C^{\text{surface}}$  (recognising a practically temperature independent  $a_C^{\text{interface}}$ ; see below). Because an Arrhenius-type temperature dependence has been observed for  $k$  (cf. Fig. 3.3), it is suggested that both  $D_C^*$  and (also)  $f_{\text{eff}}$  obey an Arrhenius-type temperature dependence. Thus, it follows from Eq. (3.3):

$$k \propto D_{0,C}^* \exp\left(-\frac{Q_D}{RT}\right) f_{0,\text{eff}} \exp\left(-\frac{Q_{f_{\text{eff}}}}{RT}\right) = D_{0,C}^* f_{0,\text{eff}} \exp\left(-\frac{Q_D + Q_{f_{\text{eff}}}}{RT}\right), \quad (3.17)$$

with  $f_{\text{eff}} = f(\Delta a_C)$  and where  $D_{0,C}^*$  and  $f_{0,\text{eff}}$  are preexponential factors for the (tracer)diffusion coefficient of carbon in cementite and  $f_{\text{eff}}$ , respectively and where  $Q_D$  is the activation energy for the (tracer)diffusion of carbon in cementite and  $Q_{f_{\text{eff}}}$  the energy describing the temperature dependence of  $f_{\text{eff}}$ . The „apparent“ activation energy  $Q_{\text{app}}$  for the cementite-layer growth is composed of the sum of the activation energy for the (tracer)diffusion of carbon in cementite,  $Q_D$ , and the energy  $Q_{f_{\text{eff}}}$  describing the temperature dependence of  $f_{\text{eff}}$ :  $Q_{\text{app}} = Q_D + Q_{f_{\text{eff}}}$ . The discrepancy between the presently determined  $Q_{\text{app}} = 109 \pm 12$  kJ/mol and  $Q_D = 154$  kJ/mol [18] and  $Q_D = 163-185$  kJ/mol [13,14], implies that  $Q_{f_{\text{eff}}}$  must be negative.

Adopting a monotonous increase of  $f_{\text{eff}}$  with  $\Delta a_{\text{C}}$  (cf. section 3.3), a negative value for  $Q_{f_{\text{eff}}}$  implies that the carbon activity difference  $\Delta a_{\text{C}}$  decreases with increasing temperature under the applied cementite-layer growth conditions. The temperature dependence of  $\Delta a_{\text{C}}$  is governed by the temperature dependence of the “effective” carbon activity in the solid at the surface; the influence of the temperature dependence of the carbon activity at the interface cementite layer/ferrite substrate is marginal ( $a_{\text{C}}^{\text{interface}}$  is practically constant<sup>3,6</sup>). Therefore, a decreasing carbon activity difference,  $\Delta a_{\text{C}}$ , with increasing temperature (see above), involves a decreasing “effective” carbon activity in the solid at the surface with increasing temperature.

As compared to the present work, the available experiments reported in the literature [13-15,19] were performed at lower treatment temperatures<sup>3,7</sup>. Therefore, the present experimental data (growth constants for four different temperatures) can only be compared with these literature data (growth constants for various carbon activities in the solid at the surface) by extrapolation of the present experimental data to these lower temperatures. Therefore, in Fig. 3.4, the straight line obtained by least-squares fitting of Eq. (3.2) to the experimental data obtained in this work was extrapolated to lower temperatures (dashed line). In Refs. [13,14] and [15,19] carbon activities in the solid at the surface were adjusted at various values at 723 K and 773 K, and the corresponding  $k$  (growth constant) values were determined. These  $k$  values, corresponding to specific carbon activities as indicated in the figure, lie below the extrapolated dashed line corresponding to the data of the current work (cf. Fig. 3.4). In order to determine the (“effective”) carbon activity in the solid at the surface for the presently applied gas atmosphere at 723 K and 773 K, the literature data pertaining to

---

<sup>3,6</sup> The carbon activity in cementite at the interface cementite layer/ferrite substrate was calculated according to Ref. [33]. It was found that  $a_{\text{C}}^{\text{interface}}$  varies as a function of temperature from 2.88 (at 783 K) to 2.13 (at 843 K). Hence,  $a_{\text{C}}^{\text{interface}}$  can be considered as (nearly) constant.

<sup>3,7</sup> The present authors also performed experiments at lower temperatures (773 K and 723 K) applying the same gas atmosphere as for the other here-reported experiments. The analysis (XRD and optical microscopy) of the resulting compound layers revealed the presence of surface-adjacent Hägg carbide and graphite, additionally to cementite; thus the layers produced were not single-phase cementite.

723 K and 773 K have been (linearly;  $k$  vs.  $a_c^{\text{surface}}$ ) extrapolated up to the dashed line derived from the present experiments. This approach led to relatively high “effective” carbon activities prevailing at the surface:  $a_c = 65$  (at 773 K) and  $a_c = 260$  (at 723 K). Hence, for the presently applied constant gas atmosphere, the “effective” carbon activity at the surface *decreases* with *increasing* treatment temperature. This result is compatible with the negative value obtained for  $Q_{f,\text{eff}}$ .

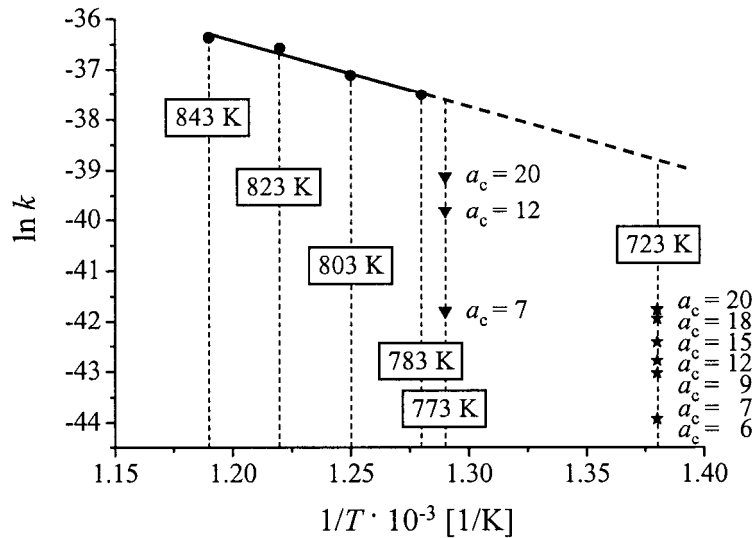


**Fig. 3.4:** Extrapolation of the Arrhenius plot shown in Fig. 3.3: (i) Experimental data of the present work have been indicated by dots: experiments performed at 843 K, 823 K, 803 K and 783 K. (ii) Literature data from Ref. [19] (triangles): experiments performed at 773 K at different carbon activities. (iii) Literature data from Refs. [13] and [14] (stars): experiments performed at 723 K at different carbon activities. The straight bold line was obtained by least-squares fitting of Eq. (3.2) to the experimental data of the present work. The straight dashed line represents the extrapolation of the experimental data of the present work to lower treatment temperatures where the experimental work reported in Refs. [13,14,19] was performed.

This specific temperature dependence of the “effective” carbon activity in the solid at the surface can be understood as follows: As discussed in section 3.4.2, the presently applied  $\text{NH}_3/\text{H}_2/\text{CO}/\text{N}_2$  containing gas atmosphere is not in thermodynamic equilibrium. Several homogeneous and heterogeneous chemical reactions (equilibria) can occur within the gas atmosphere at the surface of the solid (Eqs. (3.5), (3.8), (3.9), (3.14) – (3.16)). In general, chemical equilibria are established faster at elevated temperatures.

Hence, it may be expected that more H<sub>2</sub>O is formed (different stationary state) at higher temperatures according to Eq. (3.15). This leads to an “effective” carbon activity in the solid at the surface which is smaller at higher temperatures.

### 3.5 Conclusions

1. Massive, pure cementite layers can be grown on ferrite substrates in the range of 783 K - 843 K and 5 min - 48 h using a gas atmosphere containing 13 vol.-% NH<sub>3</sub>, 58 vol.-% H<sub>2</sub>, 20 vol.-% CO and 9 vol.-% N<sub>2</sub>. The addition of ammonia to the gas atmosphere is essential to avoid both soot formation and “metal dusting”.
2. Cementite-layer growth in the range of 783 K – 843 K obeys a parabolic growth law for  $t > 1$  h. For  $t < 1$  h ‘bypass/short-circuit’ mechanisms occur leading to relatively fast cementite growth as compared to later stages ( $t > 1$  h).
3. The parabolic growth constant exhibits an Arrhenius-type temperature dependence. It is proportional to the product of the (tracer)diffusion coefficient of carbon in the compound layer and the function  $f(\Delta a_c)$  containing the temperature-dependent activity difference of carbon over the thickness of the compound layer. Both factors separately comply with a temperature dependence according to the Arrhenius formalism.
4. An “apparent“ activation energy,  $Q_{app}$ , of  $109 \pm 12$  kJ/mol was obtained for cementite-layer growth. This “apparent“ activation energy  $Q_{app}$  is composed of a positive contribution  $Q_D$  due to the activation energy for (tracer-)diffusion of carbon in cementite and a negative contribution  $Q_{f_{eff}}$  due to a *decreasing* “effective” carbon activity in the solid at the surface with *increasing* temperature. The formation of a stationary amount of water in the gas atmosphere may induce such a fixed, finite “effective” carbon activity in the solid at the surface.

## References

- [1] Toyota Jidoshi K.K., Toyota, Aichi, JP (H. Nonoyama, T. Fukuizumi, A. Morita), Japanese Patent P58-122201 (1983/07/05)
- [2] H. Mizubayashi, S.J. Li, H. Yumoto, M. Shimotomai: *Scr. Mat.* 40 (1999) 773.
- [3] H.J. Grabke: *Mater. Corr.* 54 (2003) 736.
- [4] A. Schneider, H.J. Grabke: *Mater. Corr.* 54 (2003) 793.
- [5] M. Umemoto, Y. Todaka, T. Takahashi, P. Li, R. Tokumiya, K. Tsuchiya: *J. Metast. Nanocryst. Mater.* 15 (2003) 607.
- [6] T. Gressmann, M. Nikolussi, A. Leineweber, E.J. Mittemeijer: *Scr. Mat.* 55 (2006) 723.
- [7] M.A.J. Somers: *Heat Treat. Met.* 27 (2000) 92.
- [8] D. Liedtke, U. Baudis, J. Boßlet, U. Huchel, H. Klümper-Westkamp, W. Lerche, H.-J. Spieß: *Wärmebehandlung von Eisenwerkstoffen – Nitrieren und Nitrocarburieren*, Expert-Verlag, Renningen-Malmsheim (2006).
- [9] P.M. Unterweiser, A.G. Gray (Eds.): *Source Book on Nitriding*, ASM, Metals Park, OH (1977).
- [10] P.F. Colijn, E.J. Mittemeijer, H.C.F. Rozendaal: *Z. Metallkd.* 74 (1983) 620.
- [11] M.A.J. Somers, E.J. Mittemeijer: *Surf. Eng.* 3 (1987) 123.
- [12] E.J. Mittemeijer: *J. Heat Treating* 3 (1983) 114.
- [13] B. Ozturk, V.L. Fearing, J.A. Ruth, G. Simkovich: *Metall. Trans. A* 13A (1982) 1871.
- [14] B. Ozturk, V.L. Fearing, J.A. Ruth, G. Simkovich: *Solid State Ionics* 12 (1984) 145.
- [15] A. Schneider, G. Inden, H.J. Grabke, in: M. Rühle, H. Gleiter (Eds.): *Interface Controlled Materials (Euromat 99)*, Wiley-VCH, Weinheim (2000).
- [16] A. Schneider: *Corr. Sci.* 44 (2002) 2353.
- [17] W. Arabczyk, W. Konicki, U. Narkiewicz, I. Jasińska, K. Kałucki: *Appl. Cata. A* 266 (2004) 135.
- [18] M. Hillert, L. Höglund, J. Ågren: *J. Appl. Phys.* 98 (2005) 053511.
- [19] A. Schneider, G. Inden: *Comp. Coupl. Phase Diagr. Thermochem.* 31 (2007) 141.



- [20] R. Chatterjee-Fischer, R. Bodenhausen, F.-W. Eysell, R. Hoffmann, D. Liedtke, H. Mallener, W. Rembges, A. Schreiner, G. Welker: *Wärmebehandlung von Eisenwerkstoffen*, Expert-Verlag, Renningen-Malmsheim (1995).
- [21] A. Wells: *J. Mat. Sci.* 20 (1985) 2439.
- [22] G. Petzow: *Metallographic Etching*, ASM International, Materials Park, Ohio (1999).
- [23] K. Schwerdtfeger, P. Grieveson, E.T. Turkdogan: *Trans. TMS AIME* 245 (1969) 2461.
- [24] M.A.J. Somers, E.J. Mittemeijer: *Metall. Mater. Trans. A* 26A (1995) 57.
- [25] C. Middendorf, W. Mader: *Z. Metallkd.* 94 (2003) 333.
- [26] E.J. Mittemeijer, M.A.J. Somers: *Surf. Eng.* 13 (1997) 483.
- [27] C. Wagner, in: *Atom Movements*, ASM, Cleveland (OH) (1951).
- [28] M. Nikolussi, A. Leineweber, E.J. Mittemeijer: *Acta Mat.* in press.
- [29] T.C. Wallace, in: H. Hausner, M.G. Bowman (Eds.): *Fundamentals of refractory compounds*, Plenum Press, New York (1968).
- [30] E. Lehrer: *Z. Elektrochem.* 36 (1930) 383.
- [31] E.J. Mittemeijer, J.T. Slycke: *Surf. Eng.* 12 (1996) 152.
- [32] H.J. Grabke: *Arch. Eisenhüttenw.* 46 (1975) 75.
- [33] J. Kunze: *Nitrogen and Carbon in Iron and Steel*, Akademie-Verlag, Berlin (1990).



***Microstructure and crystallography of massive  
cementite layers on ferrite substrates***

*M. Nikolussi, A. Leineweber, E.J. Mittemeijer*

**Abstract**

Upon gaseous nitrocarburising massive cementite layers were grown on ferrite substrates. Applying Electron Backscatter Diffraction (EBSD) it was shown that the Bagaryatsky orientation relationship holds between the cementite grains of the compound layer and the ferrite grains of the substrate. The experimental data exhibit preference of specific variants of this orientation relationship: those variants corresponding with relatively *low* cementite-ferrite misfit-strain energy are favoured. Furthermore, the orientation relationship of neighbouring cementite grains grown on the same ferrite grain allows the establishment of low-energy grain boundaries between these cementite grains. In contrast, at ferrite-grain boundaries intersecting the substrate surface, high-energy cementite-grain boundaries occur between cementite grains on adjacent ferrite grains. The latter cementite-grain boundaries promote carbon grain-boundary diffusion through the cementite, which was experimentally supported by the observation of relatively large cementite-layer thicknesses at these locations.

## 4.1 Introduction

Gaseous nitriding and gaseous nitrocarburising are thermochemical heat treatments for iron-based ferritic materials, usually performed at temperatures between 773 K and 853 K (i.e. below the binary/ternary eutectoid temperature of the Fe–N/Fe–N–C solid solution), which are of great technological importance since the beginning of the twentieth century [1]. Nitrogen or nitrogen and carbon delivered by gas atmospheres containing  $\text{NH}_3/\text{H}_2$  or  $\text{NH}_3/\text{H}_2/\text{CO}$  are diffusionally incorporated into the surface region of an iron-based workpiece [2]. As a result (i) a surface-adjacent compound layer (up to several 10  $\mu\text{m}$  thick) can be formed, which is responsible for distinct improvement of the corrosion and wear resistances of the workpiece, and (ii) a diffusion zone (up to several 100  $\mu\text{m}$  thick) develops underneath the surface compound layer, which is responsible for a considerable enhancement of the fatigue endurance of the workpiece [3].

Depending on the process parameters (treatment temperature (and pressure), composition of the gas atmosphere and treatment time) the surface compound layer can consist of different phases. Usually, the compound layer is composed of a surface-adjacent  $\varepsilon\text{-Fe}_3(\text{N},\text{C})_{1+x}$  layer and a substrate-adjacent  $\gamma'\text{-Fe}_4\text{N}_{1-y}$  layer [4]. Recently, it has been shown for the first time that, employing a nitrocarburising gas atmosphere and under certain circumstances, pure cementite compound layers can be formed on a ferrite substrate [5] (cf. *chapter 2*).

The present work focuses on microstructural and crystallographic consequences of the growth of such cementite compound layers, as revealed by optical microscopy and Electron Backscatter Diffraction. The results obtained allow drawing conclusions on the role of interstitial diffusion for cementite-layer growth on ferrite which is rather distinct from that for  $\gamma'\text{-Fe}_4\text{N}_{1-y}$ -layer growth on ferrite.

## 4.2 Experimental

### 4.2.1 Specimen preparation and gaseous nitrocarburising

A ferrite cast rod (Alfa Aesar, 99.98 wt.-%) was cold rolled on both sides to a thickness of 1 mm. The resulting sheet was cut into pieces (20 mm × 25 mm), which were ground, polished (final stage 1 μm diamond) and cleaned ultrasonically in ethanol. The specimens were recrystallised at 973 K for 2 h under a hydrogen flow of 200 ml min<sup>-1</sup> and, prior to the thermochemical heat treatment, polished and cleaned ultrasonically in ethanol.

Gaseous nitriding and nitrocarburising was conducted in a vertical quartz-tube furnace. The specimens were positioned by a quartz fibre in the middle of the furnace where the process temperature, controlled by ± 1 K, prevailed. After the desired treatment time the quartz fibre was mechanically destroyed for quenching: the specimens dropped into a water container (flushed with N<sub>2</sub>) to retain states produced at the nitriding/nitrocarburising temperature. The nitriding gas atmosphere was composed of hydrogen (99.999 vol.-%) and ammonia (99.999 vol.-%) as a nitrogen-providing medium. The nitrocarburising gas atmosphere was composed of carbon monoxide (99.97 vol.-%) as a carbon-providing medium, hydrogen (99.999 vol.-%), ammonia (99.999 vol.-%) as a nitrogen-providing medium and nitrogen (99.999 vol.-%) as inert gas. Each gas flux was controlled by a mass-flow controller. An overall linear flow rate of 13.5 mm s<sup>-1</sup> (calculated for the gas volume at room temperature) through the quartz retort (diameter 28 mm) was applied to ensure that ammonia dissociation, which would change the composition of the gas atmosphere, can be neglected.

A cementite compound layer on a ferrite substrate was produced by gaseous nitrocarburising as described above for 48 h at 823 K using a gas atmosphere containing 13 vol.-% NH<sub>3</sub>, 58 vol.-% H<sub>2</sub> (nitriding potential<sup>4.1</sup>  $r_N = 0.3 \text{ atm}^{-1/2}$ ), 20 vol.-% CO and 9 vol.-% N<sub>2</sub> (as inert gas) [5] (cf. *chapter 2*).

---

<sup>4.1</sup> The chemical potential of nitrogen in the gas atmosphere can be related with the nitriding potential [6]. In the present work no carburising potential can be adjusted: the carburising potential for a gas atmosphere composed of NH<sub>3</sub>/H<sub>2</sub>/CO/N<sub>2</sub> is infinite [5] (cf. *chapter 2*).

Further, a  $\gamma'$ -Fe<sub>4</sub>N<sub>1-y</sub> layer, identical to that investigated in another study [7], was prepared by gaseous nitriding at 823 K for 5 h using a gas atmosphere containing 43 vol.-% NH<sub>3</sub> and 57 vol.-% H<sub>2</sub> (nitriding potential<sup>4.1</sup>  $r_N = 1 \text{ atm}^{-1/2}$ ).

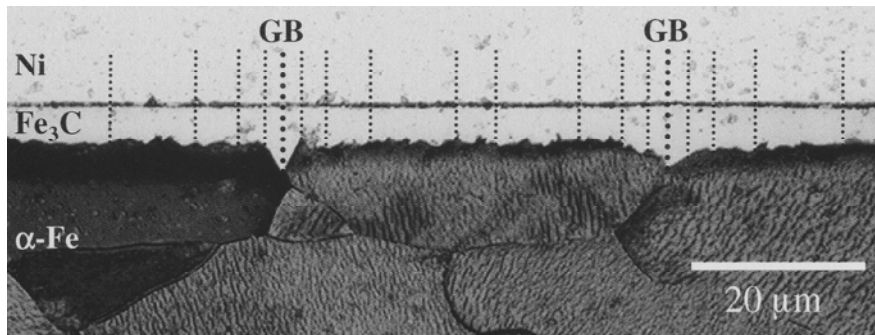
#### 4.2.2 Microstructural and crystallographic analysis

The as-nitrided/as-nitrocarburised specimens were cut into three pieces used for optical and scanning-electron microscopy, X-ray diffraction (XRD) and Electron Backscatter Diffraction (EBSD), respectively.

For optical microscopy the specimens were covered with an electrodeposited protective nickel layer using a Watts bath [4,8] at 333 K. Due to that layer, mechanical damage at the surface of metallographic cross sections can be avoided and a sufficient sharpness at the sample surface in the micrograph can be achieved. After embedding (Polyfast, Buehler GmbH), grinding and polishing (final stage colloidal silica suspension (0.04  $\mu\text{m}$ ) OPS, Struers GmbH) the specimens were stained with Klemm II colour etchant (2 g potassium bisulfite were dissolved in 300 ml Klemm stock solution (1000 g sodium thiosulfate per 300 ml distilled water) at room temperature [9]). Upon inserting the polished cross-sectional specimens into this solution, a dark blue staining of ferrite occurred; the corresponding reaction was stopped after 20 – 30 s by putting the specimens into distilled water. The thickness of the unstained cementite layer was measured as a function of the lateral distance from grain boundaries of the ferrite intersecting the cementite/ferrite interface (cf. Fig. 4.1). The variations in cementite-layer thickness at locations of some distance to such ferrite-grain boundaries (cf. Fig. 4.1) is largely due to variations in the cementite-layer thickness across the whole compound layer.

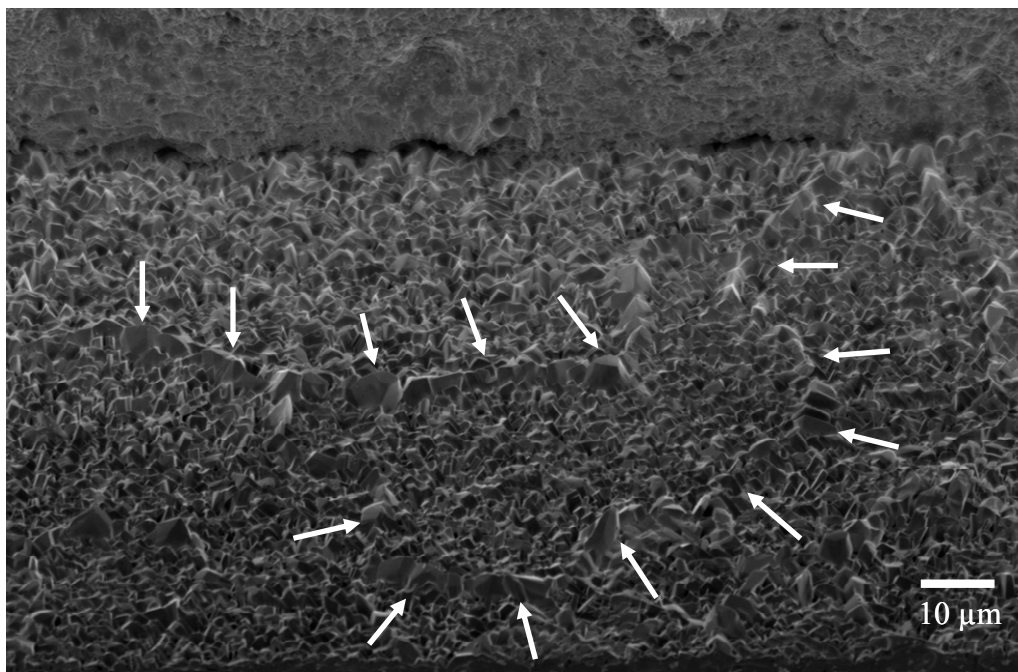
After optical microscopy (Zeiss Axiophot microscope), the cross section was again ground and polished (final stage 1  $\mu\text{m}$  diamond) and the ferrite substrate was removed selectively by deep etching with V2A reagent (100 ml hydrochloric acid, 10 ml nitric acid, 0.3 ml Vogel's special reagent and 100 ml distilled water) at 343 K [9].

Subsequently, the specimen was put into a Scanning Electron Microscope (LEO 438 VP) and tilted so that the bottom side of the cementite layer could be inspected (cf. Figs. 4.2a and 4.2b).



**Fig. 4.1:** Light optical micrograph of a metallographic cross section (a ferrite specimen was nitrocarburised at 823 K for 48 h using a gas atmosphere containing 13 vol.-%  $\text{NH}_3$ , 58 vol.-%  $\text{H}_2$ , 20 vol.-%  $\text{CO}$  and 9 vol.-%  $\text{N}_2$ ) after staining the ferrite substrate with Klemm II colour etchant. The cementite-layer thickness is largest at the location of ferrite-grain boundaries intersecting the substrate surface. The bold, dotted lines indicate the locations of cementite-layer thickness measurements there where ferrite-grain boundaries intersect the substrate surface and the normal, dotted lines indicate the locations of cementite-layer thickness measurements in distances of 2  $\mu\text{m}$ , 5  $\mu\text{m}$ , 10  $\mu\text{m}$  and 20  $\mu\text{m}$  at both sides of a ferrite-grain boundary intersecting the substrate surface (see also Fig. 4.3).

(a)



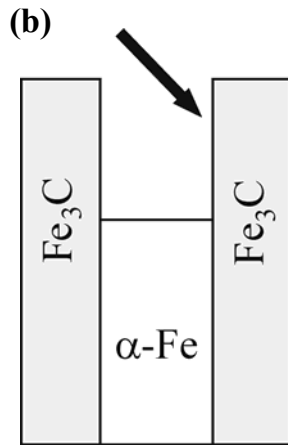


**Fig. 4.2:** Massive cementite compound layer generated on a ferrite substrate by means of nitrocarburising at 823 K for 48 h. After embedding grinding and polishing, the ferrite substrate was removed by deep etching with V2A reagent. (a) Image showing the bottom side of the cementite compound layer exhibiting lots of facets. The cementite-layer thickness is largest at places of former (before deep etching) ferrite grain boundaries (indicated by arrows). (b) Schematic illustration of the sample geometry in the SEM analysis. The arrow indicates the view on the bottom side on the cementite compound layer.

Phase identification was carried out by X-ray diffraction using a PANalytical X'Pert Multi-Purpose Diffractometer utilising  $\text{CoK}\alpha$  radiation and Bragg-Brentano geometry. The diffractometer was equipped with a graphite monochromator in the diffracted beam and the specimens were rotated during the measurements around their surface normal in order to achieve better crystallite statistics.

EBSD measurements on cross sections were conducted in order to determine the orientation of adjacent ferrite and cementite crystals, thereby establishing their relative orientations and the crystal orientation of each crystal with respect to the specimen surface. For EBSD measurements, cross sections polished as described above were additionally polished using colloidal silica suspension ( $0.04\ \mu\text{m}$ ) OPS (Struers GmbH) for several hours. Since mechanical deformation has a pronouncedly negative effect on the quality of the recorded Kikuchi patterns, the quality of the cross-sectional surface preparation is crucial for the obtained results. In general, it appeared much more difficult to obtain sufficiently good Kikuchi patterns from cementite than for ferrite or other iron (carbo)nitrides [10] (cf. *chapter 6*). For the EBSD measurements a Zeiss scanning electron microscope (LEO 438 VP) equipped with an EBSD system (TSL, EDAX, Inc.) and the software OIM 4.5 were used.



## 4.3 Experimental results

### 4.3.1 Morphology of cementite compound layers

The cementite-layer thickness was determined as a function of the lateral distance from ferrite grain boundaries intersecting the cementite layer/ferrite substrate interface (cf. Fig. 4.1). Taking several optical micrographs for the evaluation, the obtained results were arithmetically averaged per each location.

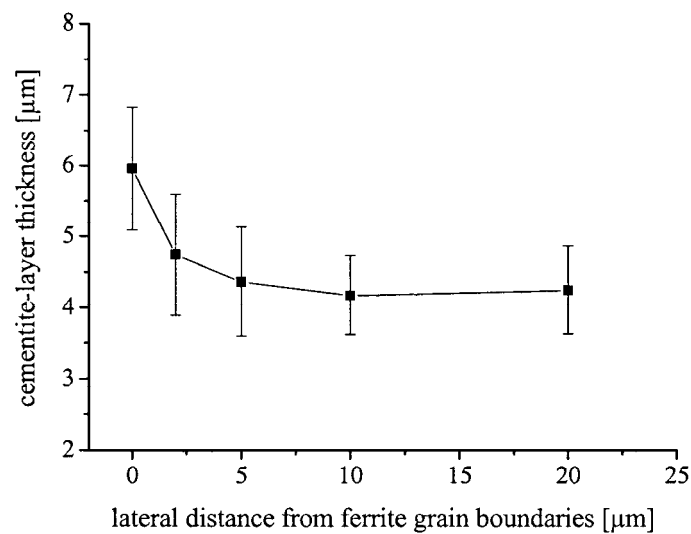


**Fig. 4.3:** The average cementite-layer thickness (for a ferrite specimen nitrocarburised at 823 K for 48 h using a gas atmosphere containing 13 vol.-%  $\text{NH}_3$ , 58 vol.-%  $\text{H}_2$ , 20 vol.-%  $\text{CO}$  and 9 vol.-%  $\text{N}_2$ ) as a function of the lateral distance to the (average) ferrite-grain boundary intersecting the substrate surface. The cementite-layer thickness is largest at the locations of the ferrite-grain boundary intersecting the substrate surface.

Evidently, the cementite-layer thickness is largest *at* the location of the ferrite grain boundaries (cf. Figs. 4.1 and 4.3); with *increasing* distance from a ferrite-grain boundary the cementite-layer thickness *decreases*.

### 4.3.2 Orientation relationship cementite-ferrite

EBSD analysis involves recording Kikuchi patterns generated by back-scattered electrons from the surface region of a crystalline solid as function of the scanning, incident electron beam's lateral position, which leads to determination of<sup>4.2</sup> (a) the crystalline phase and determination of (b) the crystal-orientation in the specimen frame of reference. In the present case, such EBSD analysis was applied to a cross section of the cementite (C) compound layer/ferrite (F) substrate system.

The grain morphology revealed by EBSD (difficult or even impossible to be visualised by optical microscopy) indicates that on a given ferrite-substrate grain several, differently oriented cementite grains grow in a columnar manner (cf. Fig 4.4).



**Fig. 4.4:** Cross-sectional EBSD image of a ferrite specimen nitrocarburised at 823 K for 48 h using a gas atmosphere containing 13 vol.-%  $\text{NH}_3$ , 58 vol.-%  $\text{H}_2$ , 20 vol.-%  $\text{CO}$  and 9 vol.-%  $\text{N}_2$  indicating that on single ferrite-substrate grain several, differently oriented cementite grains grow in a columnar manner (finely dotted areas indicate regions giving rise to insufficiently good Kikuchi patterns from cementite; cf. section 4.2.2).

The observed orientations of the  $[100]_C$ ,  $[010]_C$  and  $[001]_C$  crystallographic directions of the different cementite crystals (here the  $Pnma$  setting for the cementite's crystal structure was adopted, i.e.  $a_C = 0.50890\ \text{nm}$ ,  $b_C = 0.67433\ \text{nm}$ ,  $c_C = 0.45235\ \text{nm}$  [11]; note that in several previous works the  $Pbnm$  setting was employed) growing on a given ferrite grain are compatible – with some scatter – with the Bagaryatsky<sup>4.3</sup> orientation relationship [12] for cementite and ferrite:

<sup>4.2</sup> Provided that the crystal structure or at least the Bravais lattices of the possibly present phases are known.

<sup>4.3</sup> The Bagaryatsky orientation relationship was for the first time observed to occur in pearlite. In the literature [13-17] also other orientation relationships were proposed for pearlite, e.g. the Isaichev [13] and the Pitsch-Petch [14,17] orientation relationships.

$$[100]_C \parallel \langle 111 \rangle_F, [010]_C \parallel \langle \bar{1} \bar{1} 2 \rangle_F \text{ and } [001]_C \parallel \langle 1 \bar{1} 0 \rangle_F. \quad (4.1)$$

A scatter of less than  $3^\circ$  was found for the orientation relationship. Similar scatter was observed before for pearlite exhibiting the Bagaryatsky orientation relationship [18]. This scatter cannot be ascribed to the limited measuring accuracy of the EBSD method.

### 4.3.3 Preference of orientation-relationship variants

Twelve orientation variants of the Bagaryatsky orientation relationship [12] are in principle possible for a ferrite crystal and an adjacent cementite crystal (cf. Eq. (4.1)). These twelve orientation variants for a cementite grain growing on a given ferrite grain need not be equivalent with respect to the substrate surface: e.g. misfit-strain development may lead to preference of variants corresponding to low misfit-strain energy (see discussion in section 4.4.2). It appears likely that, for a cementite crystal growing on a ferrite crystal, those variants of the orientation relationship which can be made identical by rotation around the substrate normal (being the  $e_3^S$  basis vector of the Cartesian specimen frame of reference, S, with the  $e_1^S$  and  $e_2^S$  basis vectors parallel to the substrate surface) are equivalent. Thus, for investigation of preference of certain variants of the Bagaryatsky orientation relationship, it is sufficient to quantify the cementite crystal orientation by the values of the angles made by two (instead of three) specific crystallographic directions  $[uvw]_C$  with respect to the substrate surface, e.g. the angles of the directions  $[100]_C$  and  $[010]_C$  with respect to the substrate surface.

The largest fraction of the investigated ferrite grains are approximately oriented with a  $\langle 100 \rangle_F$  direction (nearly) parallel to the surface normal (due to rolling texture; cf. section 4.2.1). This is consistent with the observation of a (200) ferrite reflection of relatively high intensity in the XRD pattern taken with the surface normal as diffraction vector (i.e. Bragg-Brentano geometry). For such  $\langle 100 \rangle_F$ -oriented ferrite, the majority of the twelve orientation variants is equivalent (in the above sense). As a result, two classes of orientation variants, A and B, can be identified, which in

principle should statistically occur with the frequencies  $2/3$  and  $1/3$ , respectively. Analysis of the experimental data, however, shows that, in comparison with the statistically predicted occurrences, variant A is much more favoured (cf. Table 4.1).

**Table 4.1:** The statistically predicted and experimentally observed frequencies of classes of orientation variants for  $\langle 100 \rangle_{\text{F}}$ - and  $\langle 111 \rangle_{\text{F}}$ -oriented ferrite grains in the substrate surface which are characterised by the values of  $\cos^2 \angle ([100]_{\text{C}}, \mathbf{e}_3^{\text{S}})$  and  $\cos^2 \angle ([010]_{\text{C}}, \mathbf{e}_3^{\text{S}})$ . The corresponding calculated misfit-strain energies have been given too.

new orientation variant	$\cos^2 \angle ([100]_{\text{C}}, \mathbf{e}_3^{\text{S}})$	$\cos^2 \angle ([010]_{\text{C}}, \mathbf{e}_3^{\text{S}})$	statistically predicted frequency	experimentally observed frequency	misfit-strain energy [J/m <sup>3</sup> ]
$\langle 100 \rangle_{\text{F}}$ -oriented ferrite					
A	1/3	1/6	2/3	0.973	$6.8 \cdot 10^7$
B	1/3	2/3	1/3	0.027	$1.3 \cdot 10^9$
$\langle 111 \rangle_{\text{F}}$ -oriented ferrite					
A'	1/9	2/9	1/2	0.917	$6.2 \cdot 10^7$
B'	1/9	8/9	1/4	0.083	$1.1 \cdot 10^9$
C'	1	0	1/4	0	$1.5 \cdot 10^9$

For the minor fraction of ferrite grains with a  $\langle 111 \rangle_F$  direction (nearly) parallel to the surface normal, the twelve theoretically existing orientation variants degenerate to three classes of orientation variants A', B' and C', which should in principle statistically occur with the frequencies 1/2, 1/4 and 1/4, respectively. Analysis of the experimental data shows that, in comparison with the statistically predicted occurrences, variant A' is much more favoured (cf. Table 4.1).

The above results imply that favoured orientation variants are those which have cementite  $[uvw]_C$  directions of relatively large  $w$  value perpendicular to the surface, e.g.  $[213]_C$  for  $\langle 100 \rangle_F$ -oriented ferrite and  $[113]_C$  for  $\langle 111 \rangle_F$ -oriented ferrite. Unfavoured orientation variants are those with  $[uv0]_C$  directions perpendicular to the surface, e.g.  $[110]_C$  for  $\langle 100 \rangle_F$ -oriented ferrite and  $[120]_C$  for  $\langle 111 \rangle_F$ -oriented ferrite.

## 4.4 Discussion

### 4.4.1 The Bagaryatsky orientation relationship; cementite/ferrite misfit

The Bagaryatsky orientation relationship [12] applied to a cementite inclusion surrounded by ferrite would in principle allow a three-dimensional coherency between the cementite-crystal inclusion and the surrounding ferrite crystal, if the following metrical relationship would hold, without specifying the orientation of the interface:

$$\begin{aligned} a_C &= 3^{1/2} a_F \\ b_C &= 6^{1/2} a_F \\ c_C &= 2^{1/2} a_F \end{aligned} \tag{4.2}$$

Eq. (4.2) is not exactly satisfied: a cementite inclusion in hypothetically rigid (see what follows in section 4.4.2) ferrite has to be strained, in order to allow such three-dimensional coherency, according to the misfit-strain tensor  $\boldsymbol{\varepsilon}^{M,C}$  (the superscript C indicates that the tensor is formulated in the Cartesian coordinate system spanned by unit vectors parallel to the lattice basis vectors of the strain-free cementite crystal,  $\mathbf{a}_C$ ,  $\mathbf{b}_C$  and  $\mathbf{c}_C$ ),

$$\boldsymbol{\varepsilon}^{\text{M,C}} = \begin{pmatrix} \varepsilon_{11}^{\text{M,C}} & 0 & 0 \\ 0 & \varepsilon_{22}^{\text{M,C}} & 0 \\ 0 & 0 & \varepsilon_{33}^{\text{M,C}} \end{pmatrix} = \begin{pmatrix} \frac{a_{\text{C}} - 3^{\frac{1}{2}} a_{\text{F}}}{a_{\text{C}}} & 0 & 0 \\ 0 & \frac{b_{\text{C}} - 6^{\frac{1}{2}} a_{\text{F}}}{b_{\text{C}}} & 0 \\ 0 & 0 & \frac{c_{\text{C}} - 2^{\frac{1}{2}} a_{\text{F}}}{c_{\text{C}}} \end{pmatrix} \quad (4.3)$$

where  $a_{\text{F}}$  and  $a_{\text{C}}$ ,  $b_{\text{C}}$ ,  $c_{\text{C}}$  are the lattice parameter of strain-free ferrite and strain-free cementite, respectively.

Adopting experimental values for the strain-free lattice parameters of ferrite and cementite [11,19,20] one obtains for ambient temperature:

$$\varepsilon_{11}^{\text{M,C}} (298 \text{ K}) = 0.025$$

$$\varepsilon_{22}^{\text{M,C}} (298 \text{ K}) = -0.040$$

$$\varepsilon_{33}^{\text{M,C}} (298 \text{ K}) = 0.104$$

and for the carburising temperature:

$$\varepsilon_{11}^{\text{M,C}} (823 \text{ K}) = 0.021$$

$$\varepsilon_{22}^{\text{M,C}} (823 \text{ K}) = -0.041$$

$$\varepsilon_{33}^{\text{M,C}} (823 \text{ K}) = 0.102.$$

These values indicate that the linear misfit values vary only marginally as a function of temperature and that the largest misfit is observed for the **c**-direction of cementite.

#### 4.4.2 Surface misfit-strain energy of cementite grains; orientation favouritism

Preference for a certain (class of) orientation variants could be due to the intrinsic anisotropy of carbon volume diffusion in (orthorhombic) cementite. In that case, a preferred orientation variant is expected to possess a high-diffusivity direction perpendicular to the surface.

Inspection of the orthorhombic crystal structure [21-25] revealed that  $[uvw]_C$  directions with large  $w$  value in cementite, which pertains to the preferred classes of orientation variants (cf. section 4.3.3), are not obvious fast diffusion directions. It is concluded that intrinsic anisotropy of carbon volume diffusion through cementite is *not* responsible for the observed preference of certain classes of orientation variants.

It may be suggested that minimisation of misfit-strain energy provides the driving force for the emergence of a preference of a certain class of orientation variants. The misfit-strain energy is conceived here as an energy density of a cementite crystal strained elastically to accommodate the misfit with the rigid ferrite crystal substrate underneath. In the following calculation of this energy, a flat cementite crystal is considered that (i) satisfies the Bagaryatsky orientation relationship with the underlying ferrite crystal and that (ii) has a cementite/ferrite interface<sup>4.4</sup> parallel to the surface of the specimen.

The misfit-strain energy density  $W$  of the cementite crystal can be given by

$$W = \frac{1}{2} C_{ijkl} \varepsilon_{ij} \varepsilon_{kl}, \quad (4.4)$$

with  $C_{ijkl}$  as the components of the compliance tensor. The occurrence of those types of cementite crystals (subject to the Bagaryatsky orientation relationship with the underlying ferrite grain) would be preferred for which  $W$  is lowest.

---

<sup>4.4</sup> Attempts to characterise for the present cementite compound layers the orientation of the cementite/ferrite interfaces, which are faceted (cf. Fig. 4.2a), using TEM, did not lead to clear and statistically significant results.

To determine  $W$  according to Eq. (4.4), the complete strain tensor  $\boldsymbol{\varepsilon}$  of the cementite crystal has to be calculated. It appears convenient to do this in the specimen frame of reference, S, for which the generalised Hooke's law (adopting Voigt's notation) reads:

$$\begin{pmatrix} \sigma_{11}^S \\ \sigma_{22}^S \\ \sigma_{33}^S \\ \sigma_{23}^S \\ \sigma_{13}^S \\ \sigma_{12}^S \end{pmatrix} = \begin{pmatrix} C_{11}^S & C_{12}^S & C_{13}^S & C_{14}^S & C_{15}^S & C_{16}^S \\ C_{12}^S & C_{22}^S & C_{23}^S & C_{24}^S & C_{25}^S & C_{26}^S \\ C_{13}^S & C_{23}^S & C_{33}^S & C_{34}^S & C_{35}^S & C_{36}^S \\ C_{14}^S & C_{24}^S & C_{34}^S & C_{44}^S & C_{45}^S & C_{46}^S \\ C_{15}^S & C_{25}^S & C_{35}^S & C_{45}^S & C_{55}^S & C_{56}^S \\ C_{16}^S & C_{26}^S & C_{36}^S & C_{46}^S & C_{56}^S & C_{66}^S \end{pmatrix} \begin{pmatrix} \varepsilon_{11}^S \\ \varepsilon_{22}^S \\ \varepsilon_{33}^S \\ 2\varepsilon_{23}^S \\ 2\varepsilon_{13}^S \\ 2\varepsilon_{12}^S \end{pmatrix}, \quad (4.5)$$

where, due to the assumedly biaxial, planar state of stress, it holds that  $\sigma_{33}^S = \sigma_{23}^S = \sigma_{13}^S = 0$ . The components  $\varepsilon_{11}^S$ ,  $\varepsilon_{22}^S$  and  $\varepsilon_{12}^S$  of the strain tensor  $\boldsymbol{\varepsilon}^S$  of the cementite crystal parallel to the surface, are taken equal to the components  $\varepsilon_{11}^{M,S}$ ,  $\varepsilon_{22}^{M,S}$  and  $\varepsilon_{12}^{M,S}$  of the cementite's crystal misfit-strain tensor  $\boldsymbol{\varepsilon}^{M,S}$  defined by Eq. (4.3) (after transformation of the C frame of reference into the S frame of reference). For the stiffnesses,  $C_{ij}^S$ , values of the elastic constants of cementite calculated by first-principles methods were used (after transformation of the values as calculated for the C frame of reference into those pertaining to the S frame of reference) [26] (cf. *chapter 7*).

Calculations of misfit-strain energy density on the basis of Eq. (4.4) have been performed for the cementite crystals on top of  $\langle 100 \rangle_F$ - and  $\langle 111 \rangle_F$ -oriented ferrite grains, and subject to the Bagaryatsky orientation relationship. The results are shown in Table 4.1. It follows that for both the  $\langle 100 \rangle_F$ -oriented as well as for the  $\langle 111 \rangle_F$ -oriented ferrite grains the classes of preferred orientation variants correspond to clearly smaller misfit-strain energy densities (cf. Table 4.1).

It should be noted that the intrinsic elastic anisotropy of cementite is *not* primarily responsible for the observed preference of certain classes of orientation variants (the same preferences were obtained by calculations performed in this work adopting elastic isotropy of cementite). Hence, the anisotropy of the misfit strain is



responsible for the preference of certain classes of orientation variants. The results can be interpreted such that nature prevents that the **c**-direction of the cementite crystal, exhibiting the largest misfit with the ferrite substrate, is (closely) parallel to the surface/interface.

It should be recognised that the above calculation is subject to assumptions. Firstly, the cementite/ferrite interface is not truly flat and parallel to the surface; it is faceted (cf. Fig. 4.2a) and rough (larger cementite-layer thickness at ferrite-ferrite grain boundaries; section 4.3.1; cf. Figs. 4.1 and 4.3). Secondly, ideal coherency of cementite on ferrite is unlikely: the misfit strain can be very high, e.g. 10 % along the **c**-axis, which is unlikely to be accommodated fully elastically. Yet, the success of the above calculations, in explaining the obtained preference of certain classes of orientation variants, strongly suggests that the misfit-strain energy is the dominant factor for selection of the occurring orientation variant.

#### **4.4.3 Orientation relationship of adjacent cementite grains; consequence for the cementite-layer growth**

As indicated in section 4.3.2 the Bagaryatsky orientation relationship includes twelve orientation variants for a cementite grain grown on a given ferrite-substrate crystal. On this basis, possible orientation relationships between two neighbouring cementite grains on a single ferrite grain can be deduced theoretically by selecting one orientation variant, which a cementite grain can adopt on the ferrite-substrate grain, and compare the orientation of this cementite grain with the orientation of a cementite grain that adopts one of the eleven remaining orientation variants.

Adopting the ideal lattice-parameter relationship of cementite and ferrite (cf. Eq. (4.2)), it can be shown that any two different cementite crystallites on a common ferrite grain, subject to the Bagaryatsky orientation relationship, are twin related with their translation lattices giving rise to a coincidence lattice of low<sup>4.5</sup>

---

<sup>4.5</sup> The smallest possible coincidence index of two congruent lattices (i.e. lattices with the same lattice parameters) is  $\Sigma = 1$ , which represents full coincidence of the two considered cementite lattices.

coincidence index  $\Sigma$  [27]. The smaller the coincidence index is, the more energetically beneficial an interface between two crystals can be [28]<sup>4,6</sup>. Hence, favourable low-energy grain boundaries are possible between cementite grains on top of the same ferrite grain. High-energy grain boundaries can be possible between adjacent cementite grains grown on top of adjacent ferrite grains.

High-energy grain boundaries generally provide faster grain-boundary diffusion than low-energy grain boundaries do [29]. Thus, carbon diffusion along (high-energy) cementite-cementite grain boundaries between cementite grains grown on two adjacent ferrite-substrate grains (i.e. at a ferrite-ferrite grain boundary) can be more pronounced than carbon diffusion along (low-energy) cementite-cementite grain boundaries between cementite grains grown on a single common ferrite-substrate grain. Hence, in view of the above discussion, it can be expected that the cementite layer exhibits a deeper penetration (larger thickness) at the location of ferrite-ferrite grain boundaries intersecting the substrate surface, as is experimentally observed (section 4.3.1; cf. Figs. 4.1 and 4.3).

The here observed distinctly larger cementite-layer thickness at ferrite grain boundaries intersecting the substrate surface can thus be considered as experimental evidence for high-energy cementite grain boundaries at these places. These boundaries allow carbon grain-boundary diffusion which is pronouncedly faster than carbon volume diffusion in cementite. This is an untypical result for interstitial compounds, to which compound class cementite is usually considered to belong [30] (see further section 4.4.3).

---

<sup>4,6</sup> This is a crude statement: of course, the interface energy depends also on the type/orientation of the interface, which effect is not considered.

#### 4.4.4 Comparison with $\gamma'$ -Fe<sub>4</sub>N<sub>1-y</sub>

Whereas a specific (Bagaryatsky) orientation relationship holds for cementite grains grown on ferrite, no defined orientation relationship has been observed for  $\gamma'$ -Fe<sub>4</sub>N<sub>1-y</sub> grains grown on ferrite<sup>4.7</sup>. This has been shown by EBSD analysis of the  $\gamma'$ -layer grown on ferrite in the same way as for the cementite layer on ferrite (cf. sections 4.2.1 and 4.2.2).

In general, such  $\gamma'$ -Fe<sub>4</sub>N<sub>1-y</sub> compound layers have a more homogeneous thickness than cementite compound layers, suggesting that faceting at the layer/substrate interface, as it was observed for cementite compound layers (cf. Fig. 4.2a), is less pronounced or even absent in the case of the  $\gamma'$ -Fe<sub>4</sub>N<sub>1-y</sub> compound layers.

Furthermore, in contrast to a growing cementite layer, penetration of  $\gamma'$ -iron nitride along ferrite grain boundaries intersecting the substrate surface has not been observed (cf. Fig. 4.5).

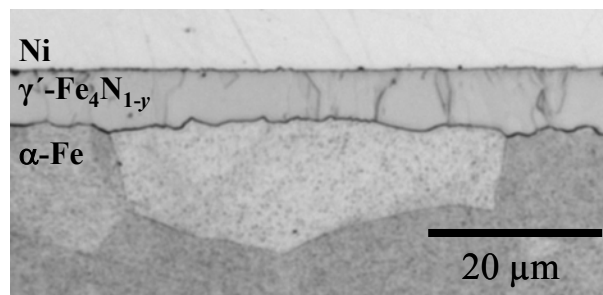


**Fig. 4.5:** Light optical micrograph of a massive  $\gamma'$ -Fe<sub>4</sub>N<sub>1-y</sub> compound layer grown on a ferrite substrate. In contrast with the cementite compound layer, the  $\gamma'$ -Fe<sub>4</sub>N<sub>1-y</sub> compound layer exhibits a less pronounced layer/substrate interface roughness and preferred layer penetration at ferrite-grain boundaries intersecting the substrate surface does not occur.

This indicates, that in contrast to grain-boundary diffusion of carbon in cementite, grain-boundary diffusion of nitrogen in  $\gamma'$ -Fe<sub>4</sub>N<sub>1-y</sub> is not significantly faster than volume diffusion, so that it does not affect the layer morphology. Grain-boundary diffusion is often considered as of subordinate importance for the mass transport of

---

<sup>4.7</sup> However,  $\gamma'$  precipitates developing in a nitrogen supersaturated ferrite matrix exhibit a specific orientation relationship [31].

interstitially dissolved elements, since a large number of vacancies on the interstitial site sublattice facilitate volume diffusion of interstitials in typical interstitial compounds. In general, both cementite and  $\gamma'$ -Fe<sub>4</sub>N<sub>1-y</sub> are regarded as interstitial compounds [30,32]. Definitely,  $\gamma'$ -Fe<sub>4</sub>N<sub>1-y</sub> is a classical interstitial compound, with an fcc-type arrangement of the iron atoms with nitrogen occupying only 1/4 of the octahedral interstitial sites (cf. Table 4.2) in an ordered fashion [33,34]. Interstitial diffusion can readily occur via the octahedral sites, of which one exists per iron atom (cf. Table 4.2).

**Table 4.2:** Number (per Fe atom) and (interstitial) occupied fraction of bicapped trigonal prisms and octahedral interstitial sites in cementite and  $\gamma'$ -Fe<sub>4</sub>N<sub>1-y</sub>.

	cementite		Fe <sub>4</sub> N <sub>1-y</sub>	
	number per iron atom	fraction occupied	number per iron atom	fraction occupied
bicapped trigonal prisms	1/3	1	-	-
octahedral sites	1/3	0	1	1/4

Cementite forms a more complex, orthorhombic iron arrangement with the largest vacancies being bicapped trigonal prisms and octahedral sites, occurring one per three iron atoms for both types of vacancies ([35]; cf. Table 4.2). The carbon atoms occupy all the bicapped trigonal prisms whereas the octahedral sites remain empty (cf. Table 4.2). Thus, carbon volume diffusion in cementite is likely to proceed also via the octahedral sites. Compared to  $\gamma'$ -Fe<sub>4</sub>N<sub>1-y</sub> less (empty) octahedral sites per iron atom exist, therefore, carbon volume diffusion may be more difficult in cementite than volume diffusion of nitrogen in  $\gamma'$ -Fe<sub>4</sub>N<sub>1-y</sub>. On this basis the relatively enhanced diffusion of carbon along high-energy grain boundaries in cementite may be understood leading to the larger cementite-layer thickness at the location of ferrite grain boundaries intersecting the specimen surface, in contrast to a more homogeneous  $\gamma'$ -layer-thickness across the whole cross section (cf. Fig 4.5).

## 4.5 Conclusions

1. The Bagaryatsky orientation relationship [12] holds for cementite grains grown on ferrite-substrate grains.
2. As a consequence of the Bagaryatsky orientation relationship twelve different orientation variants can be discerned for a cementite grain on a ferrite-substrate grain. Depending on the orientation of the underlying ferrite grain, the twelve orientation variants for the cementite grain can be subdivided into classes, where the orientation variants contained in one class differ only with respect to a rotation around the normal of the specimen surface. The experimental EBSD data indicate that those orientation variants (classes) are preferred which are associated with the development of low misfit-strain energy at the cementite/ferrite interface.
3. As a consequence of satisfying the Bagaryatsky orientation relationship, low-energy grain boundaries are expected between adjacent cementite grains on the same ferrite-substrate grain, whereas high-energy grain boundaries can occur between cementite grains on adjacent ferrite-substrate grains. Such high-energy cementite grain boundaries allow relatively fast (carbon) grain-boundary diffusion through cementite, as compared to volume diffusion of carbon in cementite, which is experimentally indicated by a larger cementite-layer thickness at the location of ferrite-grain boundaries intersecting the substrate surface.
4. Enhanced diffusion of nitrogen through high-energy grain boundaries of  $\gamma'$ -Fe<sub>4</sub>N<sub>1-y</sub>, which is a pendant of cementite in the Fe–N system, leading to penetration of  $\gamma'$ -iron nitride along ferrite-grain boundaries intersecting the substrate surface, does not occur. This may be a consequence of interstitial diffusion of nitrogen in  $\gamma'$ -Fe<sub>4</sub>N<sub>1-y</sub> readily occurring via the octahedral interstitial sites, of which, compared to cementite, more exist in  $\gamma'$ -Fe<sub>4</sub>N<sub>1-y</sub>.

## Acknowledgement

We are grateful to Dr. E. Bischoff (Max Planck Institute for Metals Research, Stuttgart, Germany) for performing the EBSD measurements and to Dr. Th. Gressmann (Max Planck Institute for Metals Research, Stuttgart, Germany) for providing the specimens containing a  $\gamma'$ -Fe<sub>4</sub>N<sub>1-y</sub> compound layer on a ferrite substrate and the corresponding EBSD data.

## References

- [1] D. Liedtke, U. Baudis, J. Boßlet, U. Huchel, H. Klümper-Westkamp, W. Lerche, H.-J. Spieß: Wärmebehandlung von Eisenwerkstoffen – Nitrieren und Nitrocarburieren, Expert-Verlag, Renningen-Malmsheim (2006).
- [2] C.H. Knerr, T.C. Rose, J.H. Filkowski, in: J.R. Davis, G.M. Davidson, S.R. Lampman, T.B. Zorc, J.L. Daquila, A.W. Ronke, et al. (Eds.): ASM Handbook, vol. 4, Heat Treating, ASM International, Metals Park (OH) (1991), p. 387..
- [3] E.J. Mittemeijer: J. Heat Treating 3 (1983) 114.
- [4] P.F. Colijn, E.J. Mittemeijer, H.C.F. Rozendaal: Z. Metallkd. 74 (1983) 620.
- [5] T. Gressmann, M. Nikolussi, A. Leineweber, E.J. Mittemeijer: Scr. Mat. 55 (2006) 723.
- [6] E.J. Mittemeijer, J.T. Slycke: Surf. Eng. 12 (1996) 152.
- [7] T. Gressmann, M. Wohlschlägel, S. Shang, U. Welzel, A. Leineweber, E.J. Mittemeijer, Z.-K. Liu: Acta Mat. 55 (2007) 5833.
- [8] R. Chatterjee-Fischer, R. Bodenhausen, F.-W. Eysell, R. Hoffmann, D. Liedtke, H. Mallener, W. Rembges, A. Schreiner, G. Welker: Wärmebehandlung von Eisenwerkstoffen, Expert-Verlag, Renningen-Malmsheim (1995).
- [9] G. Petzow: Metallographic Etching, ASM International, Materials Park (OH) (1999).
- [10] M. Nikolussi, A. Leineweber, E. Bischoff, E.J. Mittemeijer: Int. J. Mat. Res. 98 (2007) 1086.

- [11] P. Villars, L.D. Calvert, in: Pearson's Handbook of Crystallographic Data for Intermetallic Phases, ASM International, Metals Park (OH) (1985), p. 2162 and p.1520.
- [12] Y.A. Bagaryatsky: Dokl. Akad. Nauk. SSSR 73 (1950) 1161.
- [13] I.V. Isaichev: Zh. Tekh. Fiz. 17 (1947) 835.
- [14] N.J. Petch: Acta Cryst. 6 (1953) 96.
- [15] A.J. Baker, P.M. Kelly, J. Nutting: Electron Microscopy and Strength of Crystals, Interscience, New York (1961), p.899.
- [16] L.S. Darken, R.M. Fisher, in: V.F. Zackay, H.I. Aaronson (Eds.): Decomposition of Austenite by Diffusional Processes, Interscience, New York (1962), p.249.
- [17] W. Pitsch: Acta Metall. 10 (1962) 79.
- [18] D.S. Zhou, G.J. Shiflet: Metall. Trans. A 23A (1992) 1259.
- [19] H. Stuart, N. Ridley: J. Iron Steel Inst. 204 (1966) 711.
- [20] R.C. Reed, J.H. Root: Scr. Mat. 38 (1998) 95.
- [21] A. Westgren, G. Phragmén. J. Iron Steel Inst. I (1922) 241.
- [22] S. B. Hendricks: Z. Kristall. 74 (1930) 534.
- [23] H. Lipson, N.J. Petch: J. Iron Steel Inst. 142 (1940) 95.
- [24] D. Meinhardt, O. Krisement: Arch. Eisenhüttenwesen 33 (1962) 493.
- [25] E.J. Fasiska, G.A. Jeffrey: Acta Cryst. 19 (1965) 463.
- [26] M. Nikolussi, S.L. Shang, T. Gressmann, A. Leineweber, E.J. Mittemeijer, Y. Wang, Z.-K. Liu: Scr. Mat. 59 (2008) 814.
- [27] A. Authier (Ed.): International Tables for Crystallography, Volume D: Physical Properties of crystals, Kluwer Academic Publishers, Dordrecht, The Netherlands (2003).
- [28] G. Gottstein, L.S. Shvindlerman: Grain Boundary Migration in Metals, CRC Press, Boca Raton (FLA) (1999).
- [29] P.G. Shewmon: Diffusion in Solids, The Minerals, Metals & Materials Society, Warrendale (PA) (1989).
- [30] M. Hillert, L. Höglund, J. Ågren: J. Appl. Phys. 98 (2005) 053511.
- [31] U. Dahmen, P. Ferguson, K.H. Westmacott: Acta Metall. 35 (1987) 1037.
- [32] H.J. Goldschmidt: Interstitial alloys, Butterworths, London (1967).

- [33] K.H. Jack: Proc. Roy. Soc. A 195 (1948) 34.
- [34] H. Jacobs, D. Rechenbach, U. Zachwieja: J. Alloys Compd. 227 (1995) 10.
- [35] I.G. Wood, L. Vočadlo, K.S. Knight, D.P. Dobson, W.G. Marshall, G.D. Price, J. Brodholt: J. Appl. Crystallogr. 37 (2004) 82.



## *Nitrogen diffusion through cementite layers*

*M. Nikolussi, A. Leineweber, E.J. Mittemeijer*

### **Abstract**

Massive cementite layers with a time-dependent thickness were grown on ferrite substrates by nitrocarburising in a dedicated  $\text{NH}_3/\text{H}_2/\text{CO}/\text{N}_2$  containing gas atmosphere at 783 K, 823 K and 843 K. Nitrogen diffusion through the cementite layer into the ferrite substrate took place in conjunction with growth of the cementite layer; a significant, i.e. measurable solubility of nitrogen in cementite was not observed. The nitrogen concentration-depth profiles in the substrate, underneath the growing cementite layer, were quantitatively determined using a calibrated microhardness-measurement technique. The nitrogen concentration-depth profiles were simulated on the basis of a model using an implicit finite-difference method. The simulation yielded values for the diffusivity of nitrogen through cementite, including the activation energy.

## 5.1 Introduction

The corrosion and wear resistances of iron-based workpieces as well as the fatigue endurance can be improved pronouncedly by thermochemical heat treatments such as nitriding and nitrocarburising which are of great technological importance [1,2].

Gaseous nitriding and gaseous nitrocarburising are usually performed at temperatures between 773 K and 853 K. Thus, the process temperature is located below the binary/ternary eutectoid temperature of the Fe–N/Fe–N–C solid solution [3,4]. The nitriding/nitrocarburising gas atmosphere provides nitrogen or nitrogen and carbon, which are taken up by the surface-region of the iron-based workpieces [5].

The incorporation of nitrogen or nitrogen and carbon results in (i) the formation of a compound layer (several 10  $\mu\text{m}$  thick) and/or (ii) the formation of a diffusion zone (several 100  $\mu\text{m}$  thick). The compound layer is responsible for a considerable enhancement of the corrosion and wear resistance. Depending on the treatment temperature, the pressure and the composition of the gas atmosphere, the compound layer can consist of different phases. Typically  $\gamma'$ -Fe<sub>4</sub>N<sub>1-y</sub> and  $\epsilon$ -Fe<sub>3</sub>(N,C)<sub>1+x</sub> are constituents of the compound layer [6] but also cementite can occur in the compound layer [7,8] (cf. *chapter 2*). The diffusion zone is responsible for a considerable enhancement of the fatigue endurance [9]. Nitrogen or nitrogen and carbon are dissolved (at the treatment temperature) as solid solution in the octahedral interstices of the iron *bcc*-lattice.

It was shown recently that, under certain conditions, also pure, massive cementite layers can form on the ferrite substrate [8] (cf. *chapter 2*). In that case the nitrogen (and carbon) diffusion into the substrate is strongly decelerated; cementite acts as a diffusion barrier for nitrogen (and carbon [10]). Nonetheless, although nitrogen transport through cementite is decelerated, it is shown in this paper that a certain time-dependent amount of nitrogen is transported through the cementite into the ferrite substrate, leading to an increase of the nitrogen content in (and the hardness of) the ferrite substrate.

The solubility of nitrogen in the ferrite is much higher than for carbon at the temperatures of interest (783 K – 843 K) [11-13], e.g.  $\approx 0.3$  at.-% for nitrogen vs.  $\approx 0.002$  at.-% for carbon at 823 K. Furthermore, most of the carbon incorporated in the solid is used to build up the cementite layer, whereas nitrogen passes through the cementite layer to be dissolved in the ferrite.

The present work focuses on the diffusion of nitrogen through cementite. Hardness-depth profile measurements in the ferrite substrate are used to determine the nitrogen concentration-depth profiles. A model is proposed that enables the simulation of such nitrogen concentration-depth profiles. On this basis, for the first time, information about the diffusivity of nitrogen *through* cementite, including the corresponding activation energy of nitrogen diffusion in cementite, is obtained.

## 5.2 Experimental

### 5.2.1 Specimen preparation and gaseous nitriding/nitrocarburising

Two differently produced types of specimens were investigated in this study: “Thick-plate” specimens for *nitrocarburising* experiments were produced by cold-rolling a ferrite cast rod (Alfa Aesar, 99.98 wt.-% Fe) on both sides to a thickness of 1 mm. From the resulting cold-rolled sheet, rectangular pieces (20 mm  $\times$  25 mm) were cut, ground, polished (final stage 1  $\mu$ m diamond suspension) and cleaned ultrasonically in ethanol. “Thin-plate” specimens for *nitriding* experiments were produced by cutting from a 10 cm  $\times$  10 cm iron sheet (Alfa Aesar, 99.98 wt.-% Fe) of 0.1 mm thickness rectangular pieces of 20 mm  $\times$  25 mm which were ground, polished (final stage 1  $\mu$ m diamond suspension) and cleaned ultrasonically in ethanol. Both types of specimens were, prior to gaseous nitriding/nitrocarburising, recrystallised at 973 K for 2 h under a reductive hydrogen flow of 200 ml min<sup>-1</sup>, polished (final stage 1  $\mu$ m diamond suspension) and cleaned ultrasonically in ethanol.

The nitriding/nitrocarburising facility had to ensure the desired gas environment and the desired temperature during treatment. Moreover, it was necessary to quench the specimens after treatment in order to retain the microstructure as at the treatment temperature. Thus, the nitriding/nitrocarburising facility was composed of a vertical

quartz-tube furnace which was at its end equipped with a water (flushed with  $N_2$ ) container for quenching the specimens to room temperature. Using a quartz fibre, which, to realise quenching, can mechanically be destroyed after the nitriding/nitrocarburising treatment, the specimens prepared as described above were positioned in the middle of the quartz-tube furnace where the process temperature (controlled within  $\pm 1$  K) prevailed.

Two types of treatments were conducted in the present work: (i) *Nitrocarburising* experiments to study nitrogen diffusion through growing cementite layers, and (ii) *nitriding* experiments to prepare specimens of homogeneous nitrogen content and without compound layer. For these experiments, ammonia (99.999 vol.-%) as nitrogen supply, carbon monoxide (99.97 vol.-%) as carbon supply, hydrogen (99.999 vol.-%), and nitrogen (99.999 vol.-%), as inert gas, were employed. Each gas flux was controlled by a separate mass-flow controller. An overall linear flow rate of  $13.5 \text{ mm s}^{-1}$  (calculated for the gas volume at room temperature) through the quartz retort (diameter 28 mm) was maintained. Such a flow rate ensures that ammonia dissociation, which would change the composition of the gas atmosphere, can be neglected.

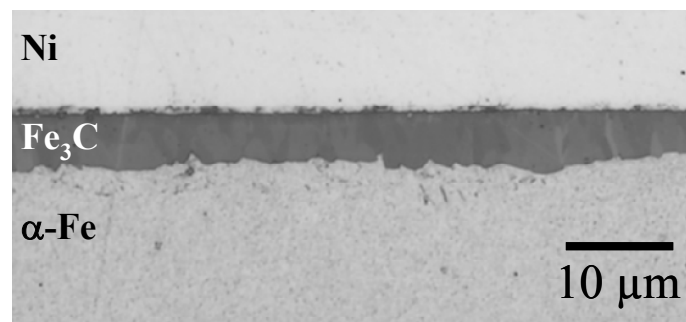


**Fig. 5.1:** Light optical micrograph (cross-sectional view; bright field) of a massive cementite layer (stained) on iron (unstained). The massive cementite layer was generated on ferrite by gaseous nitrocarburising at 823 K for 48 h. The metallographic cross-section was etched with 1 vol.-% Nital containing 1 vol.-% HCl and stained with an alkaline sodium picrate solution (cf. section 5.2).

For gaseous *nitrocarburising* the gas atmosphere was composed of 13 vol.-% NH<sub>3</sub>, 58 vol.-% H<sub>2</sub> (nitriding potential<sup>5.1</sup>  $r_N = 0.3 \text{ atm}^{-1/2}$ ), 20 vol.-% CO and 9 vol.-% N<sub>2</sub> (as inert gas). The experiments were performed at  $T = 783 \text{ K}$ ,  $823 \text{ K}$  and  $843 \text{ K}$ , for treatment times of 0.5 h, 2 h, 6 h, 14 h, 24 h and 48 h, leading always to massive cementite layers on ferrite substrates [8,15] (cf. Fig. 5.1 and *chapter 2* and *3*). For these experiments “thick-plate” specimens with a thickness of 1 mm, produced as described above, were used.

Gaseous *nitriding* experiments were performed at 823 K using different NH<sub>3</sub>/H<sub>2</sub>-containing gas atmospheres yielding different nitriding potentials<sup>5.1</sup> (cf. Table 5.1). The applied experimental conditions ensured the formation of compound-layer free specimens in accordance with the Lehrer diagram [16]. Gaseous *nitriding* was performed for 42 h in order that the ferrite substrates were saturated with interstitial nitrogen with respect to the nitriding gas atmosphere. For these experiments “thin-plate” specimens with a thickness of 0.1 mm, produced as described above, were used.

## 5.2.2 Microstructural and hardness analysis

The specimens after both the *nitriding* and the *nitrocarburising* experiments were cut into four pieces, used for light optical microscopy, hardness measurements, chemical analysis and X-ray diffraction (XRD), respectively.

For light-optical microscopy and hardness measurements the nitrocarburised specimens were covered with an electrodeposited protective nickel layer using a Watts bath [6,17] at 333 K. The protective nickel layer avoids mechanical damage at the surface of the metallographic cross sections and guarantees the required sharpness at the sample surface in the cross sections. All specimens (nitriding and nitrocarburising experiments) were embedded using a Struers LaboPress 3. Embedding was performed with 15 ml Polyfast (Buehler GmbH), a load of 15 kN, an annealing time of 5 min at

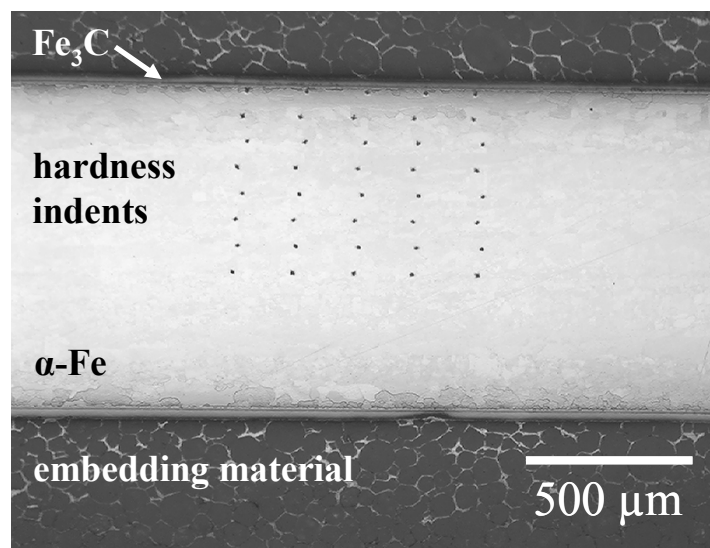
---

<sup>5.1</sup> The chemical potential of nitrogen in the gas atmosphere can be related with the nitriding potential [14]. In the present work no carburising potential can be adjusted: the carburising potential for a gas atmosphere composed of NH<sub>3</sub>/H<sub>2</sub>/CO/N<sub>2</sub> is (hypothetically) infinite [8] (cf. *chapter 2*) although an “effective” carburising potential acts at the specimen surface [15] (cf. *chapter 3*).

453 K and a cooling time of 3 min down to room temperature. After embedding, the specimens were ground, polished (final stage 1  $\mu\text{m}$  diamond suspension) and etched using 1 vol.-% Nital containing 0.1 vol.-% HCl [18]. In order to differentiate between the massive cementite layer and the ferrite substrate, the cross-sectional specimens were stained using either (i) an alkaline potassium permanganate solution (1 g NaOH, 1 g KOH and 4 g  $\text{KMnO}_4$  per 100 ml distilled water) at 328 K [8,19] (cf. *chapter 2*) of which the effect is similar to that of a Murakami solution [6,19] or (ii) an alkaline sodium picrate solution (25 g NaOH and 2 g picric acid per 75 ml distilled water) at room temperature [19]. In both cases the massive cementite layer gets, due to its high carbon content, severely stained. The ferrite substrate remains unstained and can therefore easily be distinguished from the cementite layer upon light optical microscopy (Zeiss Axiophot microscope).

Hardness measurements (micro-Vickers) were performed with a Leica VMHT MOT microhardness indenter using a load of 25 gf ( $\cong 0.245$  N) for 10 s. Hardness-depth profile measurements in the ferrite substrates were performed for all specimens of the *nitrocarburising* experiments. Hardness indents were set at selected distances from the interface cementite/ferrite until the middle of the specimen was reached (cf. Fig. 5.2a).

(a)



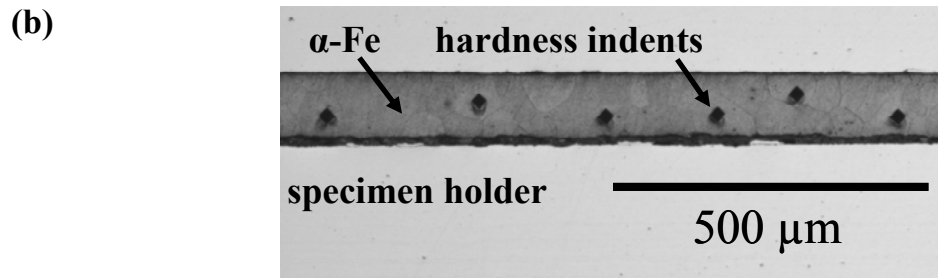


**Fig. 5.2:** Hardness indents in the ferrite substrate (light-optical micrograph; cross sectional view) for the investigation of the dependence between nitrogen content in and hardness of the ferrite substrate. (a) Specimen with a massive cementite layer of time-dependent thickness on ferrite (nitrocarburising experiment). Several hardness indents were set, starting at the interface and ending until the middle of the specimen was reached. (b) Hardness indents in ferrite of a compound-layer free specimen (nitriding experiment).

The exact distance values of the hardness indents from the interface cementite/ferrite were determined by light optical microscopy using the software “analySIS” (Soft Imaging System GmbH). For each specific distance value from the interface cementite/ferrite five hardness measurements were made; the average value was taken as the local hardness and the standard deviation was taken as indication of the experimental error. For all specimens of the *nitriding* experiments, which should have – due to the small specimen thickness and due to the long treatment time - a homogeneous nitrogen content, 10 hardness measurements were made across the cross-sectional specimen (cf. Fig. 5.2b); their average value and their standard deviation was calculated.

Chemical analysis was performed by carrier-gas hot extraction to determine the nitrogen content in the ferrite substrates of all nitrided specimens, in order to relate the determined nitrogen content to the hardness of the ferrite substrates (see section 5.3). For the *nitrided* specimens, the reliability of the results of the chemical analysis was verified by an additional nitrogen-content determination via weighing [20]: The ferrite substrates were weighted before and after gaseous nitriding using a Mettler Toledo UMX2 precision balance. Additionally, such chemical analysis was performed for specimens which were *nitrocarburised* at 823 K with a treatment time of 6 h, 14 h, 24 h and 48 h, since these specimens do *not* exhibit a nitrogen concentration (hardness) gradient across the ferrite substrate in the cross section (cf. Fig. 5.3b).

Prior to chemical analysis, the massive cementite layer was removed by grinding so that only the nitrogen-enriched substrate was analysed. After completion of the grinding procedure, it was checked by X-ray diffraction whether the entire cementite layer had been removed.

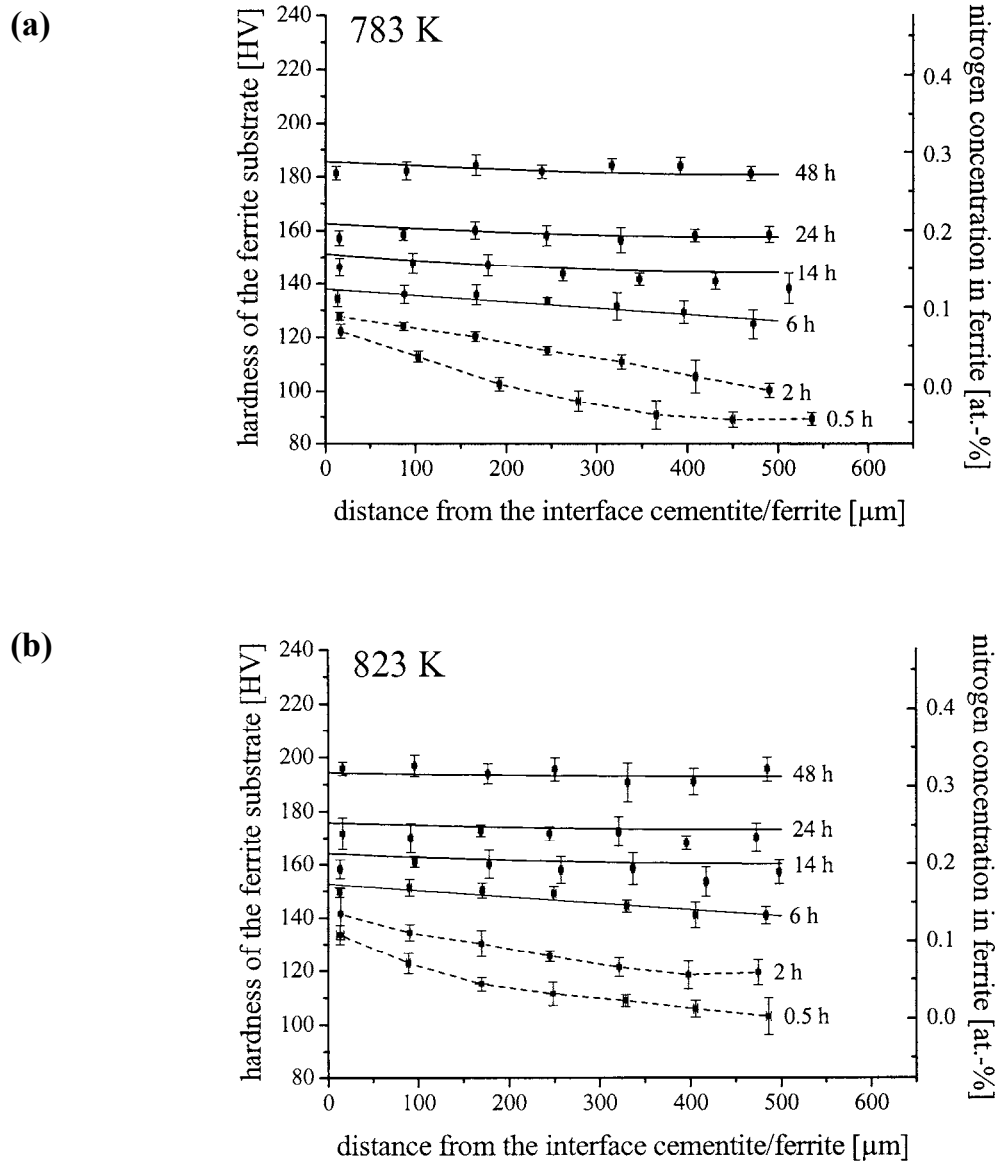
To verify the presence or absence of a (cementite) compound layer, phase identification was carried out by X-ray diffractometry. A PANalytical X'Pert Multi-Purpose Diffractometer, which was equipped with a graphite monochromator in the diffracted beam, was used. The diffractometer was operated with  $\text{CoK}\alpha$  radiation in Bragg-Brentano geometry. Each specimen was rotated around its surface normal during the measurements to achieve better crystallite statistics.

### **5.3 Experimental results and evaluation: hardness measurements and chemical analysis**

Each *nitrocarburising* experiment performed at 783 K, 823 K and 843 K led to the formation of a massive cementite layer on the ferrite substrates (cf. Fig. 5.1) [8,15] (cf. *chapter 2* and *3*). The cementite layers exhibit a characteristic microstructure (partially rough ferrite-cementite interface) and a specific orientation relationship with the ferrite substrate [21] (cf. *chapter 4*). After cross-sectional metallographic preparation, hardness-depth profile measurements were performed in the ferrite substrate (cf. Figs. 5.2a and 5.3a – 5.3c).



In order to transform hardness-depth profiles into nitrogen concentration-depth profiles (cf. Figs. 5.3a – 5.3c), the dependence of hardness on nitrogen content in ferrite has to be known. Such a dependence was obtained on the basis of the results for hardness and nitrogen content in homogeneously nitrated/nitrocarburised ferrite given in Table 5.1 and shown in Fig. 5.4.



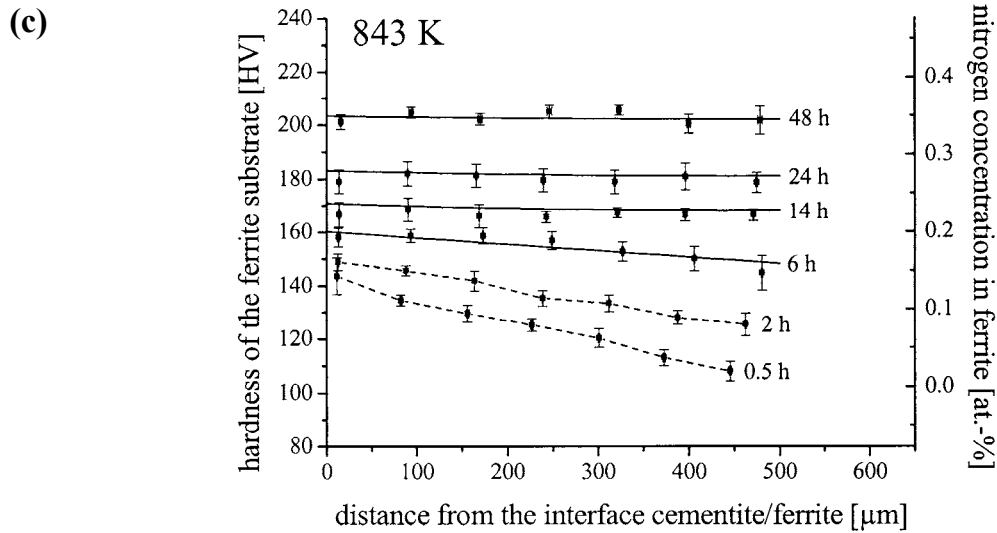


**Fig. 5.3:** Experimentally determined hardness-depth profiles in the ferrite substrate with a massive cementite layer of time-dependent thickness at the surface of the ferrite substrate (dots; cf. hardness axes). Hardness-depth profiles were transformed into nitrogen concentration-depth profiles (dots; cf. nitrogen-concentration axes) applying the calibrated hardness-nitrogen concentration relation (cf. Fig. 5.4). The simulated nitrogen concentration-depth profiles are shown by the continuous curves. The dashed curves indicate experimentally determined hardness/nitrogen concentration-depth profiles (0.5 h and 2 h) which were not considered for the simulation. Experiments as well as simulations were performed at (a) 783 K, (b) 823 K and (c) 843 K.

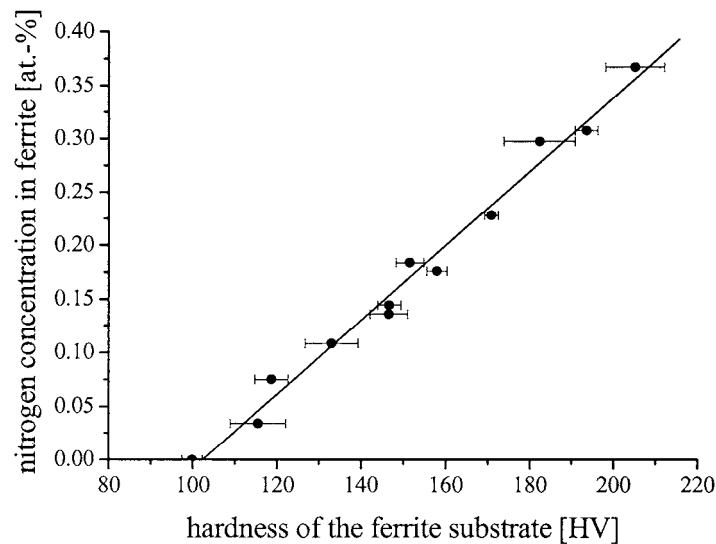


**Fig. 5.4:** Calibration line: Nitrogen concentration (determined by chemical analysis/weighing; the error is smaller than the size of the dots) vs. the hardness for homogeneous ferrite substrates (determined by micro-Vickers hardness indentations). The straight line was determined by least-squares fitting of Eq. (5.1) to the experimental data.

**Table 5.1:** The experimentally determined (average) hardness values and (average) nitrogen contents (chemical analysis) of all *nitrided* specimens. Composition (NH<sub>3</sub> and H<sub>2</sub> contents and corresponding nitriding potential) of the *nitriding* gas atmosphere, yielding compound-layer free specimens, have been indicated. The experiments were performed for 42 h at 823 K leading to a homogeneous solid solution of interstitial nitrogen in the ferrite substrate. Nitrogen-content determination of *nitrided* specimens via weighing showed similar results. The hardness of pure iron without any nitrogen dissolved determined in this work equals  $100 \pm 2$  HV. Similar results obtained for some selected (see text) *nitrocarburising* experiments at 823 K have been given as well.

<i>nitriding</i> experiments							
NH <sub>3</sub> content [vol.-%]	2	4	6	7	9	12	13
H <sub>2</sub> content [vol.-%]	98	96	94	93	91	88	87
nitriding potential, $r_N$ [atm <sup>-1/2</sup> ]	0.02	0.04	0.06	0.08	0.1	0.14	0.16
hardness [HV]	116 ± 7	119 ± 4	133 ± 6	147 ± 3	152 ± 3	182 ± 9	205 ± 7
nitrogen concentration [at.-%]	0.034	0.075	0.108	0.144	0.184	0.297	0.367
<i>nitrocarburising</i> experiments							
treatment time [h]	6	14	24	48			
hardness [HV]	147 ± 4	158 ± 2	171 ± 2	194 ± 3			
nitrogen concentration [at.-%]	0.136	0.176	0.228	0.307			

It follows that a linear dependence exists between nitrogen content and hardness of the ferrite substrate:

$$C_N^{\alpha\text{-Fe}} = mh + b, \quad (5.1)$$

where  $C_N^{\alpha\text{-Fe}}$  denotes the nitrogen concentration in the ferrite substrate, and  $h$  its hardness.

Least-squares fitting of a straight line to the experimental data in Fig. 5.4 yielded the following values for  $m$  (slope of the straight line in Fig. 5.4) and  $b$  (part cut from the ordinate):  $m = (3.46 \pm 0.1) \cdot 10^{-3} \frac{\text{at.}\%}{\text{HV}}$  and  $b = -0.354 \pm 0.02 \text{ at.}\%$ . On this basis, the experimentally determined hardness-depth profiles can be transformed into nitrogen concentration-depth profiles (cf. Figs. 5.3a – 5.3c). This was done for all considered treatment temperatures (783 K, 823 K and 843 K) and treatment times.

Such quantitative information on the nitrogen concentration in ferrite cannot be obtained by other techniques. Whereas e.g. chemical analysis can only provide an average nitrogen concentration across the whole specimen (instead of a location-resolved nitrogen concentration), the sensitivity of electron probe microanalysis (EPMA) is too low for the presently determined nitrogen concentrations.

## 5.4 Modelling nitrogen concentration-depth profile development

### 5.4.1 General assumptions

The experimentally determined nitrogen concentration-depth profiles will be simulated to analyse, on the basis of comparison with the experimentally determined nitrogen concentration-depth profiles, the diffusivity of nitrogen through cementite.

Consider a laterally infinitely extended iron plate of finite thickness. Nitrogen can enter this plate from both sides; a symmetrical (with respect to the centre plane of the plate) nitrogen concentration-depth profile is built up.

The process of gaseous nitrocarburising can be subdivided into four different steps: (i) diffusion of ammonia from the gas phase to the surface of the specimen, (ii) dissociation of ammonia at the surface, (iii) nitrogen diffusion through the growing cementite layer of time-dependent thickness, (iv) nitrogen diffusion within ferrite (after having diffused through the cementite layer) from the interface cementite/ferrite to the core of the specimen. Ad (i): In the present experiments the gas-flow through the quartz-tube furnace is large; the gas composition at the sample surface can be taken constant for a constant treatment temperature [15] (cf. *chapter 3*).

Ad (ii): Already after very short treatment time dissociation of ammonia at the surface of the specimen is *not* rate determining for the nitrogen uptake; instead nitrogen diffusion through the growing cementite layer is rate-determining (in contrast with the case of nitriding pure ferrite [22]). The conditions indicated under ad (i) and ad (ii) imply that local equilibrium prevails at the interface of the gas atmosphere and the specimen. Furthermore, local equilibrium is assumed to hold at the interface cementite/ferrite.

Nitrogen diffusion within ferrite is governed by Fick's second law

$$\frac{\partial C_N^{\alpha\text{-Fe}}}{\partial t} = D_N^{\alpha\text{-Fe}} \frac{\partial^2 C_N^{\alpha\text{-Fe}}}{\partial x^2}, \quad (5.2)$$

where  $D_N^{\alpha\text{-Fe}}$  is the diffusion coefficient of nitrogen in ferrite (taken as concentration independent),  $C_N^{\alpha\text{-Fe}}$  the nitrogen concentration at depth  $x$  (measured from the interface cementite/ferrite<sup>5.2</sup>) and  $t$  the time of diffusion.

The flux of nitrogen through cementite at the interface cementite/ferrite,  $J_N^{\text{Fe}_3\text{C}}|_{x=0}$ , is equal to the flux of nitrogen into ferrite at this interface  $J_N^{\alpha\text{-Fe}}|_{x=0}$  which, using Fick's first law, can be expressed as follows

$$J_N^{\text{Fe}_3\text{C}}|_{x=0} = J_N^{\alpha\text{-Fe}}|_{x=0} = -D_N^{\alpha\text{-Fe}} \frac{\partial C_N^{\alpha\text{-Fe}}}{\partial x}|_{x=0}, \quad (5.3)$$

where  $x = 0$  denotes the location coordinate which represents the interface cementite/ferrite.

---

<sup>5.2</sup> The cementite layer is thin compared to the ferrite substrate at all considered treatment times and the cementite layer grows much slower than the extent of the nitrogen concentration-depth profile in the substrate. Therefore, the consumption of a part of the ferrite upon formation of the cementite is neglected in the modelling of the diffusion of nitrogen in ferrite.

Nitrogen enters the ferrite substrate at both sides. Hence, a symmetrical nitrogen concentration-depth profile results and no net flux of nitrogen through the middle of the sample occurs, leading to the second boundary condition

$$\left. \frac{\partial C_N^{\alpha\text{-Fe}}}{\partial x} \right|_{x=Z} = 0, \quad (5.4)$$

where  $x = Z$  denotes the position of the centre plane.

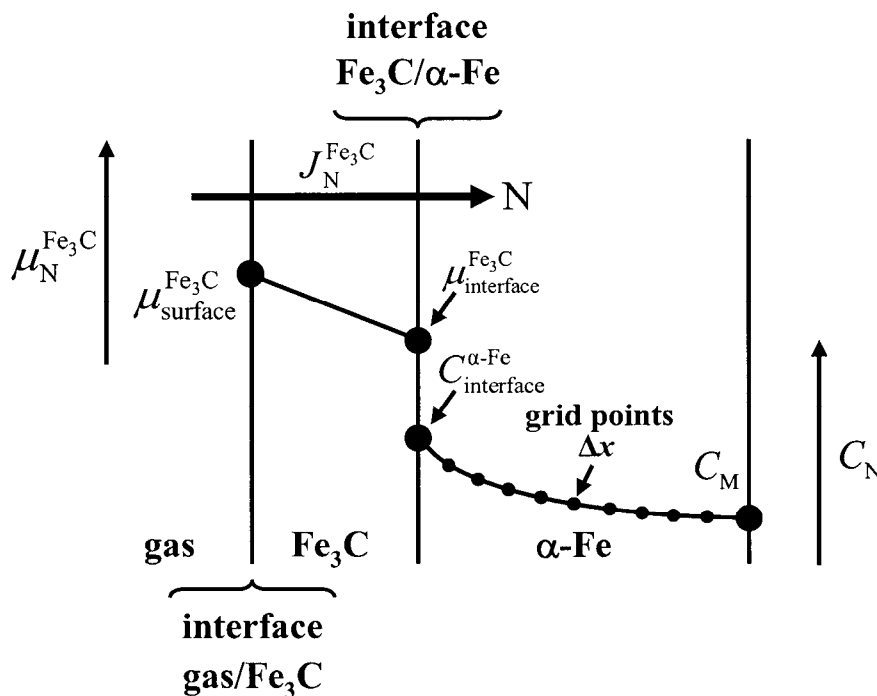


**Fig. 5.5:** Schematic drawing of a cementite layer on a ferrite substrate (cross-sectional view). A gradient of the chemical potential of nitrogen in cementite provokes the flux of nitrogen through cementite. Consequently, a nitrogen concentration-depth profile develops in the ferrite substrate, which can be calculated for different time steps and grid points using the model described in section 5.4 applying the implicit finite-difference method. Local equilibrium at the gas-solid interface and at the cementite/ferrite interface is assumed.

Before nitrogen can pass the interface cementite/ferrite and can diffuse through ferrite, it must be transported through the cementite layer<sup>5.3</sup>. Nitrogen diffusion through cementite is provoked by a gradient of the chemical potential of nitrogen across the cementite layer (cf. Fig. 5.5)

$$F = - \left( \frac{\partial \mu_{\text{N}}^{\text{Fe}_3\text{C}}}{\partial x} \right)_{p,T}, \quad (5.5)$$

where  $F$  is the thermodynamic force,  $\mu_{\text{N}}^{\text{Fe}_3\text{C}}$  the chemical potential of nitrogen in cementite and  $x$  the location coordinate,  $T$  the treatment temperature and  $p$  the pressure.

For the nitrogen flux through cementite,  $J_{\text{N}}^{\text{Fe}_3\text{C}}$ , it holds that [24]

$$\begin{aligned} J_{\text{N}}^{\text{Fe}_3\text{C}} &= v_{\text{N}}^{\text{Fe}_3\text{C}} C_{\text{N}}^{\text{Fe}_3\text{C}} = M_{\text{N}}^{\text{Fe}_3\text{C}} F C_{\text{N}}^{\text{Fe}_3\text{C}} \\ &= -M_{\text{N}}^{\text{Fe}_3\text{C}} C_{\text{N}}^{\text{Fe}_3\text{C}} \left( \frac{\partial \mu_{\text{N}}^{\text{Fe}_3\text{C}}}{\partial x} \right)_{p,T} = -D_{\text{N}}^{\text{Fe}_3\text{C}} \left( \frac{\partial C_{\text{N}}^{\text{Fe}_3\text{C}}}{\partial x} \right)_{p,T}, \end{aligned} \quad (5.6)$$

where  $v_{\text{N}}^{\text{Fe}_3\text{C}}$  denotes the drift velocity of nitrogen in cementite,  $M_{\text{N}}^{\text{Fe}_3\text{C}}$  is the mobility of nitrogen in cementite,  $D_{\text{N}}^{\text{Fe}_3\text{C}}$  represents the diffusion coefficient of nitrogen in cementite and  $C_{\text{N}}^{\text{Fe}_3\text{C}}$  is the nitrogen concentration in cementite. The diffusion coefficient of nitrogen in cementite can be expressed by

$$D_{\text{N}}^{\text{Fe}_3\text{C}} = M_{\text{N}}^{\text{Fe}_3\text{C}} RT \left( 1 + \frac{\partial \ln \gamma_{\text{N}}^{\text{Fe}_3\text{C}}}{\partial \ln C_{\text{N}}^{\text{Fe}_3\text{C}}} \right), \quad (5.7)$$

where  $\left( 1 + \frac{\partial \ln \gamma_{\text{N}}^{\text{Fe}_3\text{C}}}{\partial \ln C_{\text{N}}^{\text{Fe}_3\text{C}}} \right)$  is the thermodynamic factor, with  $\gamma_{\text{N}}^{\text{Fe}_3\text{C}}$  as the activity coefficient of nitrogen in cementite.

---

<sup>5.3</sup> Since the solubility of nitrogen in cementite is negligible [23], all nitrogen entering cementite is passed through cementite.

The solubility of nitrogen in cementite is extremely small, e.g. for 1593 K a solubility of about 0.064 at.-% was reported [23]. Due to this extremely limited solubility, Henry's law [25,26] is assumed for nitrogen in cementite. Consequently, the thermodynamic factor equals one and  $D_N^{\text{Fe}_3\text{C}}$  reduces to

$$D_N^{\text{Fe}_3\text{C}} = M_N^{\text{Fe}_3\text{C}} RT = D_N^{*,\text{Fe}_3\text{C}}, \quad (5.8)$$

where  $D_N^{*,\text{Fe}_3\text{C}}$  is the (tracer-)diffusion coefficient of nitrogen in cementite. Thus,

$$J_N^{\text{Fe}_3\text{C}} = -D_N^{*,\text{Fe}_3\text{C}} \left( \frac{\partial C_N^{\text{Fe}_3\text{C}}}{\partial x} \right)_{p,T}. \quad (5.6b)$$

A linear concentration profile of nitrogen across cementite is assumed. The concentration difference of nitrogen across the cementite layer is given by the difference of the nitrogen concentration in cementite at the interface gas atmosphere/cementite,  $C_{\text{surface}}^{\text{Fe}_3\text{C}}$ , and the nitrogen concentration in cementite at the interface cementite/ferrite,  $C_{\text{interface}}^{\text{Fe}_3\text{C}}$ . Then Eq. (5.6b) can be given as

$$J_N^{\text{Fe}_3\text{C}} = -\frac{D_N^{*,\text{Fe}_3\text{C}} (C_{\text{surface}}^{\text{Fe}_3\text{C}} - C_{\text{interface}}^{\text{Fe}_3\text{C}})}{S_{\text{Fe}_3\text{C}}}, \quad (5.9)$$

where  $S_{\text{Fe}_3\text{C}}$  is the cementite-layer thickness.



The nitrogen concentrations in cementite at the interface gas atmosphere/cementite and at the interface cementite/ferrite will be expressed in terms of “corresponding” (see what follows) nitrogen concentrations in ferrite. For both, cementite and ferrite, Henry’s law can be adopted. Therefore, for cementite and ferrite in (hypothetical) equilibrium with each other and, possibly additionally, with the same outer gas atmosphere, the concentrations of nitrogen in cementite,  $C_N^{\text{Fe}_3\text{C}}$ , and in ferrite,  $C_N^{\alpha\text{-Fe}}$ , are related by<sup>5.4</sup>

$$C_N^{\text{Fe}_3\text{C}} = \varphi C_N^{\alpha\text{-Fe}}, \quad (5.10)$$

where  $\varphi$  is the partition coefficient. Hence, the nitrogen concentration in ferrite at the cementite/ferrite interface in (real, local) equilibrium with cementite at the same interface corresponds to  $C_{\text{interface}}^{\alpha\text{-Fe}} = C_{\text{interface}}^{\text{Fe}_3\text{C}} / \varphi$  and thus  $C_{\text{interface}}^{\text{Fe}_3\text{C}} = \varphi C_{\text{interface}}^{\alpha\text{-Fe}}$ . Diffusion of nitrogen through the cementite will come to a halt if the nitrogen concentration in the ferrite corresponds to the nitrogen concentration which would prevail in ferrite in (hypothetical) equilibrium with the gas atmosphere,  $C_{\text{eq}}^{\alpha\text{-Fe}}$ . Hence, the concentration of nitrogen in cementite at the surface in (real, local) equilibrium with the gas atmosphere,  $C_{\text{surface}}^{\text{Fe}_3\text{C}}$ , is given by  $C_{\text{surface}}^{\text{Fe}_3\text{C}} = \varphi C_{\text{eq}}^{\alpha\text{-Fe}}$ .

The above consideration implies that Eq. (5.9) can be written as

$$J_N^{\text{Fe}_3\text{C}} = \frac{\varphi D_N^{*\text{Fe}_3\text{C}} (C_{\text{eq}}^{\alpha\text{-Fe}} - C_{\text{interface}}^{\alpha\text{-Fe}})}{S_{\text{Fe}_3\text{C}}}. \quad (5.11)$$

---

<sup>5.4</sup> For the chemical potential of nitrogen in cementite it holds that  $\mu_N^{\text{Fe}_3\text{C}} = \mu_N^0 + RT \ln \gamma_N^{\text{Fe}_3\text{C}} x_N^{\text{Fe}_3\text{C}}$  and for the chemical potential of nitrogen in ferrite it holds that  $\mu_N^{\alpha\text{-Fe}} = \mu_N^0 + RT \ln \gamma_N^{\alpha\text{-Fe}} x_N^{\alpha\text{-Fe}}$ . Assuming for both, cementite and ferrite, the same reference state and Henry’s law (constant activity coefficient of nitrogen), the mole fractions of nitrogen in cementite and ferrite in equilibrium with each other are related by a partition coefficient,  $\varphi$ , according to  $\varphi = \frac{\gamma_N^{\alpha\text{-Fe}}}{\gamma_N^{\text{Fe}_3\text{C}}}$ . It will be assumed that for the minute range of nitrogen concentration in cementite  $\varphi$  does not depend on nitrogen concentration.

The cementite-layer thickness  $S_{\text{Fe}_3\text{C}}$  has been determined experimentally for the present samples. The layer thickness could be described for each temperature by adopting a modified parabolic growth law [8,15] (cf. *chapter 2* and 3)

$$S_{\text{Fe}_3\text{C}}^2(t) = k(T)t + S_0^2(T), \quad (5.12)$$

where  $k$  denotes the parabolic growth constant and  $S_0$  a (hypothetical) initial cementite-layer thickness at  $t = 0$  (see discussion in Ref. [8]; cf. *chapter 2*). Combining

Eqs. (5.11) and (5.12) leads to 
$$J_{\text{N}}^{\text{Fe}_3\text{C}} = \frac{\varphi D_{\text{N}}^{*\text{Fe}_3\text{C}} (C_{\text{eq}}^{\alpha\text{-Fe}} - C_{\text{interface}}^{\alpha\text{-Fe}})}{(kt + S_0^2)^{1/2}}.$$

#### 5.4.2 Simulation of nitrogen concentration-depth profiles; numerical procedure

For the simulation of the nitrogen concentration-depth profiles, Fick's first and second law have to be solved subject to the boundary conditions given by Eqs. (5.3) and (5.4). This can be done numerically on the basis of the method after Crank and Nicolson [22,27] using the implicit finite-difference method. For that purpose the nitrogen concentration profile within ferrite was calculated for equidistant grid points in space (distance  $\Delta x$ ) (cf. Fig. 5.5) at different time steps (see what follows in section 5.5). Details of the numerical procedure are described in the Appendix.

### 5.5 Results of the simulation

The simulation was performed with  $M = 100$  grid points (up to the middle of the specimen) and different time steps. The increment of time was increased by 0.5 % after each generation of a nitrogen concentration profile [22], recognising the decrease of the nitrogen-concentration gradients with time, in order to reduce calculation time.

Doing this, the condition  $r = \frac{D_{\text{N}}^{*\text{Fe}_3\text{C}} \Delta t}{(\Delta x)^2} \leq 1/2$  has to be fulfilled [27], where  $\Delta t$  denotes

the increment of the time and  $\Delta x$  denotes the grid-point distance. The simulation was

started at the respective treatment temperatures on the basis of the nitrogen concentration-depth profile determined after 6 h, since for smaller treatment times the diffusion geometry and mechanism is incompatible with the model (see section 5.6.2).

The following parameters were known: (i) the diffusion coefficient of nitrogen in ferrite, which was calculated for the respective treatment temperature according to Ref. [28] (cf. Table 5.2) and (ii) the cementite-layer thickness, which was determined experimentally. Hence, the fitting parameters were: the equilibrium nitrogen concentration in ferrite,  $C_{\text{eq}}^{\alpha\text{-Fe}}(T)$ , and the product of the partition coefficient and the (tracer-)diffusion coefficient of nitrogen in cementite,  $\phi D_{\text{N}}^{*\text{Fe}_3\text{C}}$ . Values for these parameters were determined (for each considered treatment temperature) by minimising the sum of the squared differences of simulated and experimental nitrogen concentrations for all treatment times *simultaneously* (cf. Figs. 5.3a – 5.3c). The results obtained for  $C_{\text{eq}}^{\alpha\text{-Fe}}$  and  $\phi D_{\text{N}}^{*\text{Fe}_3\text{C}}$  have been gathered in Fig. 5.6 and Table 5.2.

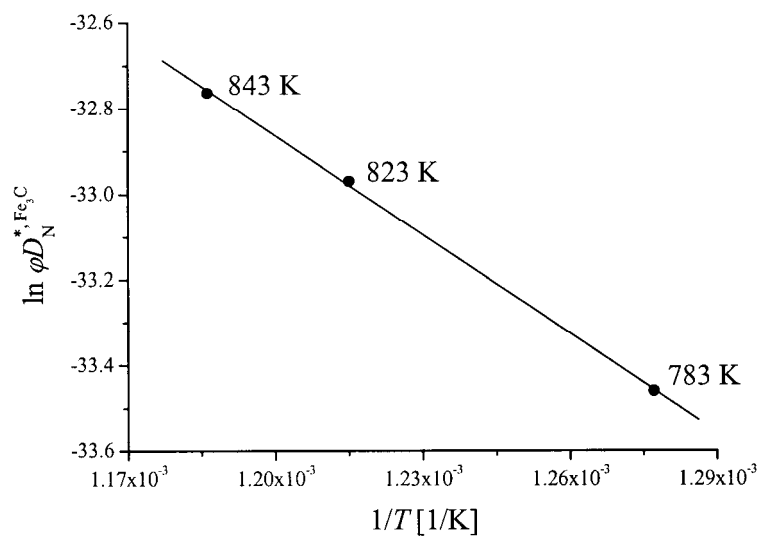


**Fig. 5.6:** Arrhenius plot: natural logarithm of the product of the partition coefficient and the (tracer-)diffusion coefficient of nitrogen through cementite,  $\phi D_{\text{N}}^{*\text{Fe}_3\text{C}}$ , versus the reciprocal temperature  $1/T$ .

**Table 5.2:** Results of the simulation of nitrogen concentration-depth profiles. The equilibrium nitrogen concentration in ferrite, and the product of the partition coefficient and the (tracer-)diffusion coefficient of nitrogen through cementite were refined by matching of the simulated data and the experimental data by least-squares fitting. Furthermore, the diffusion coefficient of nitrogen in ferrite has been given according to Ref. [28].

treatment temperature, $T$ [K]	783	823	843
equilibrium nitrogen concentration in ferrite, $C_{\text{eq}}^{\alpha\text{-Fe}}$ [at.-%]	0.599	0.613	0.700
product of the partition coefficient and the (tracer-)diffusion coefficient of nitrogen through cementite, $\varphi D_{\text{N}}^{*\text{Fe}_3\text{C}}$ [m <sup>2</sup> /s]	$2.9 \cdot 10^{-15}$	$4.8 \cdot 10^{-15}$	$5.9 \cdot 10^{-15}$
diffusion coefficient of nitrogen in ferrite, $D_{\text{N}}^{\alpha\text{-Fe}}$ [m <sup>2</sup> /s]	$7.4 \cdot 10^{-12}$	$1.3 \cdot 10^{-11}$	$1.8 \cdot 10^{-11}$

Adopting an Arrhenius-type temperature dependence for the (tracer-)diffusion coefficient of nitrogen in cementite and taken the partition coefficient  $\varphi$  as temperature independent, a plot of the logarithm of  $\varphi D_{\text{N}}^{*\text{Fe}_3\text{C}}$  vs.  $1/T$  should yield a straight line. This is observed indeed; see Fig. 5.6. The slope of the straight line obtained equals  $m = -Q/R$ , with  $Q$  as the activation energy of nitrogen diffusion in cementite and  $R$  as the gas constant. It follows:  $Q = 65 \pm 2$  kJ/mol.

## 5.6 Concluding discussion

### 5.6.1 Hardness/concentration-depth profiles

The hardness of the ferrite substrates increases linearly with the nitrogen concentration. Upon embedding (cf. section 5.2), which has to be considered as a heat treatment, the nitrogen in the ferrite forms (semi-)coherent  $\alpha''$ -Fe<sub>16</sub>N<sub>2</sub> precipitates [29-33], which are responsible for the hardness increase as measured at room temperature. In order to guarantee comparability of the hardness measurements, the embedding has to be performed in a reproducible way. Therefore, a special standard embedding procedure was developed, which has been described in section 5.2.

The calibration line shown in Fig. 5.4 was determined on the basis of experiments performed at 823 K. This calibration line was also applied to the data obtained at 783 K and 843 K. The true relation between hardness and nitrogen content at 783 K and 843 K may differ slightly from that pertaining at 823 K. This may be the origin of the slightly negative nitrogen-concentration values in the ferrite substrate for some data points at very short treatment times (0.5 h and 2 h) at 783 K (cf. Fig. 5.3a).

The data obtained for the nitrogen concentration-depth profiles at the three different considered treatment temperatures indicate pronounced nitrogen concentration gradients in the ferrite matrix at short treatment times as 0.5 h and 2 h; the concentration gradients level off with increasing treatment time. The development of the nitrogen concentration-depth profile in the ferrite substrate is dominated by two processes: (i) nitrogen transport through the cementite layer via diffusion. The cementite-layer thickness increases as a function of the treatment time (according to a modified parabolic growth law [8,15]; cf. *chapter 2* and *3*). Therefore, the nitrogen flux through cementite *decreases* with *increasing* treatment time. (ii) The inward-diffusion of nitrogen into the ferrite substrate remains relatively fast. From (i) and (ii) it is concluded that the initially large nitrogen concentration gradient in the ferrite substrate decreases with time, as observed.

### 5.6.2 Simulation of nitrogen concentration-depth profiles

In the present work, nitrogen concentration-depth profiles in the ferrite substrate with a growing cementite layer at the surface were simulated. In the literature [22] such an approach was already applied for the calculation of nitrogen concentration-depth profiles of compound-layer free ferrite specimens. In that case local equilibrium between gas atmosphere and the surface of the specimen was not immediately established. Therefore, nitrogen absorption and/or ammonia dissociation and nitrogen transfer through the surface contributed significantly to the process kinetics. In fact, nitrogen transfer through the cementite layer in the present case and nitrogen transfer through the surface in case of nitriding ferrite without compound layer at the surface (Ref. [22]) can be conceived as analogues. However, different dependences on  $(C_{\text{eq}}^{\alpha\text{-Fe}} - C_{\text{interface}}^{\alpha\text{-Fe}})$  occur in both cases: In Ref. [22]:  $J_{\text{N}}^{\text{surf}} \sim k(C_{\text{eq}}^{\alpha\text{-Fe}} - C_{\text{interface}}^{\alpha\text{-Fe}})$  and here:  $J_{\text{N}}^{\text{Fe}_3\text{C}} \sim \frac{D_{\text{N}}^{\text{Fe}_3\text{C}}(C_{\text{eq}}^{\alpha\text{-Fe}} - C_{\text{interface}}^{\alpha\text{-Fe}})}{S^{\text{Fe}_3\text{C}}}$ , i.e. in the present, last case an extra time dependence, through  $S^{\text{Fe}_3\text{C}}$ , is introduced.

Treatment times of 0.5 h and 2 h were not considered in the simulation procedure. In the early stage of cementite formation ( $t < 6$  h), cementite-layer growth proceeded faster than as predicted by the developed model. This can be explained as follows: (i) in the early stage of cementite formation an incompletely closed cementite layer is present [8,15] (cf. *chapter 2* and *3*). Nitrogen diffusion from the surface of the specimen into ferrite proceeds directly, i.e. bypassing cementite<sup>5.5</sup>. (ii) Further, just after the formation of a closed cementite layer, short-circuit diffusion of nitrogen through thin and defect-rich parts of the cementite layer occurs. In this stage of cementite formation, cementite is expected to exhibit a relatively high grain-boundary density; for data demonstrating grain-boundary diffusion in cementite, see Ref. [21] (cf. *chapter 4*).

---

<sup>5.5</sup> Transport of nitrogen in ferrite is much faster than transport of nitrogen through cementite. See what follows in section 5.6.2.

Due to such a ‘bypass/short-circuit’ mechanism, nitrogen can be transported relatively fast through the cementite layer in the early stage of cementite formation<sup>5,6</sup>. Therefore, treatment times < 6 h were not used in the data evaluation on the basis of the model developed in section 5.4.1.

Literature data for the equilibrium nitrogen concentration in ferrite vary considerably: e.g. the values reported in Ref. [34] are distinctly lower than the values reported in Ref. [13]. The values of  $C_{\text{eq}}^{\alpha\text{-Fe}}$  obtained in the present work are generally larger than those compatible with the data from Refs. [13] and [34]. These differences can be understood recognising that the nitrogen concentration in the ferrite substrate,  $C_{\text{eq}}^{\alpha\text{-Fe}}$ , as determined in the present work, pertains to the (hypothetical) equilibrium of ferrite with the present nitrocarburising gas atmosphere. In reality such an equilibrium cannot occur: for such high nitrogen concentrations, solubility limits for nitrogen in ferrite in equilibrium with iron (carbo-)nitrides are surpassed, and formation of  $\gamma\text{'-Fe}_4\text{N}$  below 833 K or of  $\varepsilon\text{-Fe}_3(\text{N,C})_{1+x}$  above 843 K [35] (cf. *chapter 6*) occurs. Indeed, in the present work, treatment times  $\gg$  48 h at 853 K occasionally led to the formation of these (carbo-)nitride phases at the cementite/ferrite interface.

According to the knowledge of the present authors, diffusion data of nitrogen in cementite have not been reported, before. The values obtained for the product of the partition coefficient and the (tracer-)diffusion coefficient of nitrogen through cementite are considerably lower than values for the diffusion coefficients of nitrogen in ferrite [28,36] (cf. Table 5.2) and iron nitrides [37-41] at similar treatment temperatures. The role of the cementite layer as diffusion barrier for nitrogen can be illustrated by assuming that the cementite layer would instead consist of ferrite. In that case, in Eq. (5.11)  $\phi D_{\text{N}}^{*\text{,Fe}_3\text{C}}$  should be substituted by  $D_{\text{N}}^{\alpha\text{-Fe}}$ . Hence, the nitrogen flux through the (cementite) surface layer,  $J_{\text{N}}^{\text{Fe}_3\text{C}}$ , would increase by a factor  $D_{\text{N}}^{\alpha\text{-Fe}} / \phi D_{\text{N}}^{*\text{,Fe}_3\text{C}}$ , i.e. a factor of about 2500 - 3000 (cf. Table 5.2).

---

<sup>5,6</sup> A similar explanation was used for the observed enhanced initial growth rate during carbon-diffusion controlled cementite-layer growth on ferrite [8,15] (cf. *chapter 2* and 3).

This clearly demonstrates the diffusion-barrier behaviour of the cementite layer for nitrogen, which then could be due in particular to the very low solubility of nitrogen in cementite, leading to very small values of  $\varphi$ ; further, the pre-exponential factors contained in  $D_N^{\alpha\text{-Fe}}$  and  $D_N^{*\text{,Fe}_3\text{C}}$  may differ considerably.

The activation energy of nitrogen diffusion through cementite (here determined as  $65 \pm 2$  kJ/mol) is relatively low as compared to real or “apparent” activation energies for carbon diffusion through cementite which are in the range of 110 – 185 kJ/mol [15,42-44] (cf. *chapter 3*), and for nitrogen diffusion in iron nitrides, which are in the range of 92 – 144 kJ/mol [39,41,45]. The activation energy for nitrogen diffusion in cementite appears to be as low as the activation energy for nitrogen (or carbon) diffusion in ferrite, which is about 78 – 79 kJ/mol [28,36]. One possibility is that  $\varphi$ , although very small, depends significantly on temperature and thus affects the activation energy value determined. Another possibility is that the low activation energy for  $D_N^{*\text{,Fe}_3\text{C}}$  may hint at nitrogen transport favourably occurring via cementite grain boundaries; preferred diffusion of carbon along grain boundaries in cementite was reported very recently [21] (cf. *chapter 4*).

## 5.7 Conclusions

1. Hardness-depth profile measurements provide a powerful method to quantitatively determine nitrogen-concentration depth profiles in ferrite (maximal nitrogen content:  $\approx 0.4$  at.-%) on the basis of a calibrated, found to be linear relation between hardness and nitrogen content.
2. Massive cementite layers with a time-dependent thickness can be generated on ferrite substrates by gaseous nitrocarburising at 783 K, 813 K and 843 K. The nitrogen concentration-depth profile in the ferrite substrate underneath the growing cementite layer can be simulated on the basis of a developed model using the implicit finite-difference method, yielding values for the diffusivity of nitrogen through cementite.
3. The effective activation energy of nitrogen diffusion through cementite is about as large as the activation energy of nitrogen diffusion in ferrite. This may hint at



nitrogen grain-boundary diffusion as dominant transport mechanism of nitrogen through cementite. The cementite layer acts as a diffusion barrier for nitrogen in particular because of the very low solubility of nitrogen in cementite.

## Appendix

### Numerical procedure for nitrogen concentration-depth profile calculation

The finite-difference expressions of the derivatives  $\partial C/\partial t$  and  $\partial^2 C/\partial x^2$  read [27]:

$$\frac{\partial C_N^{\alpha\text{-Fe}}}{\partial t} = \frac{C_i^{j+1} - C_i^j}{\Delta t}, \quad (5.13)$$

and

$$\frac{\partial^2 C_N^{\alpha\text{-Fe}}}{\partial x^2} \cong \frac{1}{2} \left[ \frac{C_{i+1}^j - 2C_i^j + C_{i-1}^j}{(\Delta x)^2} + \frac{C_{i+1}^{j+1} - 2C_i^{j+1} + C_{i-1}^{j+1}}{(\Delta x)^2} \right], \quad (5.14)$$

where  $j$  and  $i$  denote a time step and a grid point, respectively<sup>5.7</sup> and  $C_i^j$  indicates the nitrogen concentration in ferrite for a time step  $j$  at a grid point  $i$ . The combination of Eqs. (5.2), (5.13) and (5.14) yields

$$C_i^{j+1} - C_i^j = \frac{1}{2} \frac{D_N^{\alpha\text{-Fe}}(\Delta t)}{(\Delta x)^2} \left\{ (C_{i+1}^j + C_{i+1}^{j+1}) - 2(C_i^j + C_i^{j+1}) + (C_{i-1}^j + C_{i-1}^{j+1}) \right\}. \quad (5.15)$$

The nitrogen concentration at the interface can be expressed as the concentration which prevails at grid point '1'; it can be calculated as the arithmetic mean of the nitrogen concentration at grid point '1' at the beginning and at the end of a time interval  $\Delta t$ :

$$C_{\text{interface}}^{\alpha\text{-Fe}} = \frac{1}{2} (C_1^j + C_1^{j+1}). \quad (5.16)$$

---

<sup>5.7</sup> Eq. (5.14) represents the arithmetic mean of  $\partial^2 C_N^{\alpha\text{-Fe}}/\partial x^2$  at the beginning and the end of a time interval  $\Delta t$ .

In order to express the derivative  $\partial C_N^{\alpha\text{-Fe}} / \partial x|_{x=0}$  by a finite-difference expression a “fictitious” concentration  $C_0$  at an external grid point ‘0’ has to be introduced:

$$\left. \frac{\partial C_N^{\alpha\text{-Fe}}}{\partial x} \right|_{x=0} \cong \frac{1}{2} \left\{ \frac{C_2^j - C_0^j}{2(\Delta x)} + \frac{C_2^{j+1} - C_0^{j+1}}{2(\Delta x)} \right\}. \quad (5.17)$$

Combining Eqs. (5.6b) and (5.11) and inserting Eqs. (5.16) and (5.17) leads to the reformulated first boundary condition (cf. Eq. (5.3))

$$-D_N^{\alpha\text{-Fe}} \frac{1}{4(\Delta x)} \left\{ (C_2^j - C_0^j) + (C_2^{j+1} - C_0^{j+1}) \right\} = \frac{\varphi D_N^{*\text{Fe}_3\text{C}} \left( C_{\text{eq}}^{\alpha\text{-Fe}} - \frac{1}{2}(C_1^j + C_1^{j+1}) \right)}{(kt + S_0^2)^{1/2}}. \quad (5.18)$$

The terms  $C_0^j$  and  $C_0^{j+1}$  in Eq. (5.18) are unknown, but they can be eliminated as follows. First Eq. (5.18) is rewritten:

$$C_0^j + C_0^{j+1} = \frac{\frac{\varphi D_N^{*\text{Fe}_3\text{C}}}{(kt + S_0^2)^{1/2}} 4(\Delta x) \left\{ C_{\text{eq}}^{\alpha\text{-Fe}} - \frac{1}{2}(C_1^j + C_1^{j+1}) \right\}}{D_N^{\alpha\text{-Fe}}} + (C_2^j + C_2^{j+1}). \quad (5.18b)$$

Then Eq. (5.18b) can be inserted into Eq. (5.15) for  $i = 1$ . This leads to

$$C_1^{j+1} - C_1^j = \frac{D_N^{\alpha\text{-Fe}} \cdot (\Delta t)}{(\Delta x)^2} \left\{ (C_2^j + C_2^{j+1}) - (C_1^j + C_1^{j+1}) + \frac{\varphi D_N^{*\text{Fe}_3\text{C}} (\Delta x)}{D_N^{\alpha\text{-Fe}} (kt + S_0^2)^{1/2}} \left[ 2C_{\text{eq}}^{\alpha\text{-Fe}} - (C_1^j + C_1^{j+1}) \right] \right\} \quad (5.19)$$

In order to calculate the concentration  $C_1^{j+1}$  at grid point '1' and time step  $j+1$ , Eq. (5.19) has to be transformed into

$$C_1^{j+1} = \frac{\frac{D_N^{\alpha-Fe}(\Delta t)}{(\Delta x)^2} (C_2^j + C_2^{j+1} - C_1^j) + \frac{\varphi D_N^{*Fe_3C}(\Delta t)}{(\Delta x)(kt+S_0^2)^{1/2}} (2C_{eq}^{\alpha-Fe} - C_1^j) + C_1^j}{1 + \frac{D_N^{\alpha-Fe}(\Delta t)}{(\Delta x)^2} + \frac{\varphi D_N^{*Fe_3C}(\Delta t)}{(\Delta x)(kt+S_0^2)^{1/2}}}. \quad (5.19b)$$

The concentrations  $C_i^{j+1}$  at the grid points  $i = 2 \dots (M-1)$  at the time step  $j+1$  can be calculated by transforming the expression given by Eq. (5.15) into

$$C_i^{j+1} = \frac{\frac{D_N^{\alpha-Fe}(\Delta t)}{(\Delta x)^2} \left( \frac{1}{2} (C_{i+1}^j + C_{i+1}^{j+1}) - C_i^j + \frac{1}{2} (C_{i-1}^j + C_{i-1}^{j+1}) \right) + C_i^j}{1 + \frac{D_N^{\alpha-Fe}(\Delta t)}{(\Delta x)^2}}. \quad (5.15b)$$

The concentration  $C_M^{j+1}$  at the half of the thickness of the sample,  $Z$ , at time step  $j+1$  can be calculated using the second boundary condition given by Eq. (5.4). The second boundary condition is satisfied when it holds that  $C_{M-1} = C_{M+1}$ . Thus, from Eq. (5.15) for  $i = M$  (grid point at the half of the thickness  $Z$  of the sample;  $M\Delta x = Z$ ) it follows

$$C_M^{j+1} = \frac{\frac{D_N^{\alpha-Fe}(\Delta t)}{(\Delta x)^2} (C_{M-1}^j + C_{M-1}^{j+1} - C_M^j) + C_M^j}{1 + \frac{D_N^{\alpha-Fe}(\Delta t)}{(\Delta x)^2}}. \quad (5.20)$$

From Eqs. (5.19b) for  $i = 1$ , (5.20) for  $i = M$ , and (5.15b) for  $i = 2 \dots (M-1)$  a system of  $M$  equations results which has  $M$  unknowns ( $C_1^{j+1}, \dots, C_M^{j+1}$ ). For each time step these unknowns can be deduced iteratively. The known set of concentrations of the previous time step ( $C_1^j, \dots, C_M^j$ ) is taken as a first approximation to the unknown set of new concentrations ( $C_1^{j+1}, \dots, C_M^{j+1}$ ).

## References

- [1] P.M. Unterweiser, A.G. Gray (Eds.): Source Book on Nitriding, ASM, Metals Park (OH) (1977).
- [2] D. Liedtke, U. Baudis, J. Boßlet, U. Huchel, H. Klümper-Westkamp, W. Lerche, H.-J. Spieß: Wärmebehandlung von Eisenwerkstoffen – Nitrieren und Nitrocarburieren, Expert-Verlag, Renningen-Malmsheim (2006).
- [3] T.B. Massalski, H. Okamoto (Eds.): Binary Alloy Phase Diagrams, ASM International, Metals Park (OH) (1990).
- [4] H. Du, M. Hillert: Z. Metallkde. 82 (1991) 310.
- [5] C.H. Knerr, T.C. Rose, J.H. Filkowski, in: J.R. Davis, G.M. Davidson, S.R. Lampman, T.B. Zorc, J.L. Daquila, A.W. Ronke, et al. (Eds.): ASM Handbook, vol. 4, Heat Treating, ASM International, Metals Park (OH) (1991), p. 387.
- [6] P.F. Colijn, E.J. Mittemeijer, H.C.F. Rozendaal: Z. Metallkd. 74 (1983) 620.
- [7] M.A.J. Somers, E.J. Mittemeijer: Surf. Eng. 3 (1987) 123.
- [8] T. Gressmann, M. Nikolussi, A. Leineweber, E.J. Mittemeijer: Scr. Mat. 55 (2006) 723.
- [9] E.J. Mittemeijer: J. Heat. Treating. 3 (1983) 114.
- [10] A. Schneider, H.J. Grabke: Mater. Corr. 54 (2003) 793.
- [11] O. Kubaschewski: Iron-Binary Phase Diagrams, Springer-Verlag, Berlin; Verlag Stahleisen, Düsseldorf (1982).
- [12] H.A. Wriedt, N.A. Gokcen, R.H. Nafziger: Bull. Alloy. Phase. Diagr. 8 (1987) 355.
- [13] J. Kunze: Nitrogen and Carbon in Iron and Steel, Akademie-Verlag, Berlin (1990).
- [14] E.J. Mittemeijer, J.T. Slycke: Surf. Eng. 12 (1996) 152.
- [15] M. Nikolussi, A. Leineweber, E.J. Mittemeijer: submitted for publication.
- [16] E. Lehrer: Z. Elektrochem. 36 (1930) 383.
- [17] R. Chatterjee-Fischer, R. Bodenhagen, F.-W. Eysell, R. Hoffmann, D. Liedtke, H. Mallener, W. Rembges, A. Schreiner, G. Welker: Wärmebehandlung von Eisenwerkstoffen, Expert-Verlag, Renningen-Malmsheim (1995).
- [18] A. Wells: J. Mat. Sci. 20 (1985) 2439.

- [19] G. Petzow: *Metallographic Etching*, ASM International, Materials Park, Ohio (1999).
- [20] S.S. Hosmani, R.E. Schacherl, E.J. Mittemeijer: *Acta Mat.* 54 (2006) 2783.
- [21] M. Nikolussi, A. Leineweber, E.J. Mittemeijer: *Acta Mat.* in press.
- [22] H.C.F. Rozendaal, E.J. Mittemeijer, P.F. Colijn, P.J. van der Schaaf: *Metall. Trans. A* 14A (1983) 395.
- [23] A. Kagawa, T. Okamoto: *Trans. Japan Inst. Met.* 22 (1981) 137.
- [24] P.G. Shewmon: *Diffusion in solids*, 2<sup>nd</sup> edition, The Minerals, Metals & Materials Society, Warrendale (PA) (1989).
- [25] P.W. Atkins: *Physikalische Chemie*, Wiley-VCH, Weinheim (2001).
- [26] G. Wedler: *Lehrbuch der physikalischen Chemie*, Wiley-VCH, Weinheim (2007).
- [27] J. Crank: *The Mathematics of Diffusion*, 2<sup>nd</sup> edition, Oxford Science Publications (1975).
- [28] M. Weller: *Mechanical Spectroscopy Q<sup>-1</sup> 2001*, in: R. Schaller, G. Fantozzi, G. Gremaud (Eds.): *Mater. Sci. Forum* 366-368 (2001) 95.
- [29] E. Kubalek: *Härtereit Tech. Mitt.* 23 (1968) 177.
- [30] D.H. Jack, K.H. Jack: *Mat. Sci. Eng.* 11 (1973) 1.
- [31] Y. Inokuti, N. Nishida, N. Ōhashi: *Metall. Trans. A* 6A (1975) 773.
- [32] U. Dahmen, P. Ferguson, K.H. Westmacott: *Acta Metall.* 35 (1987) 1037.
- [33] Z.Q. Liu, Y.X. Chen, Z.K. Hei, D.X. Li, H. Hashimoto: *Metall. Mater. Trans. A* 32A (2001) 2681.
- [34] B.J. Kooi, M.A.J. Somers, E.J. Mittemeijer: *Metall. Mater. Trans. A* 27A (1996) 1055.
- [35] M. Nikolussi, A. Leineweber, E.J. Mittemeijer: *Int. J. Mat. Res.* 98 (2007) 1086.
- [36] J.D. Fast, M.B. Verrijb: *J. Iron Steel Inst.* 176 (1954) 24.
- [37] K. Schwerdtfeger, P. Grieveson, E.T. Turkdogan: *Trans. TMS AIME* 245 (1969) 2461.
- [38] M.A.J. Somers, E.J. Mittemeijer: *Metall. Mater. Trans. A* 26A (1995) 57.
- [39] E.J. Mittemeijer, M.A.J. Somers: *Surf. Eng.* 13 (1997) 483.
- [40] C. Middendorf, W. Mader: *Z. Metallkd.* 94 (2003) 333.

- [41] T. Liapina, A. Leineweber, E.J. Mittemeijer: *Metall. Mater. Trans. A* 37A (2006) 319.
- [42] B. Ozturk, V.L. Fearing, J.A. Ruth, G. Simkovich: *Metall. Trans. A* 13A (1982) 1871.
- [43] B. Ozturk, V.L. Fearing, J.A. Ruth, G. Simkovich: *Solid State Ionics* 12 (1984) 145.
- [44] M. Hillert, L. Höglund, J. Ågren: *J. Appl. Phys.* 98 (2005) 053511.
- [45] A. Leineweber: *Acta Mat.* 55 (2007) 6651.





*Examination of phase transformations in the system  
Fe–N–C by means of nitrocarburising reactions and  
secondary annealing experiments; the  $\alpha + \varepsilon$   
two-phase equilibrium*

*M. Nikolussi, A. Leineweber, E. Bischoff, E.J. Mittemeijer*

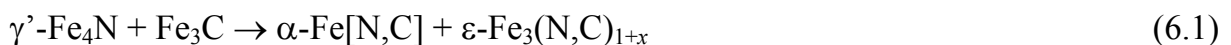
**Abstract**

The until now controversially discussed existence of the two-phase equilibrium  $\alpha\text{-Fe} + \varepsilon\text{-Fe}_3(\text{N,C})_{1+x}$  in the ternary system Fe–N–C was proven by the investigation (optical microscopy, X-ray diffraction, Electron Backscattering Diffraction) of compound-layer microstructures generated by gaseous nitrocarburising of pure iron and subsequent secondary annealing experiments under static inert-gas atmosphere. The invariant transition reaction  $\gamma'\text{-Fe}_4\text{N} + \text{Fe}_3\text{C} \rightarrow \alpha\text{-Fe} + \varepsilon\text{-Fe}_3(\text{N,C})_{1+x}$  could be shown to proceed at a (single) temperature (at constant pressure of 1 atm) between 833 K and 843 K.

## 6.1 Introduction

Thermochemical heat treatments such as nitriding and nitrocarburising of iron-based alloys, usually performed between 773 K and 853 K (below the binary/ternary eutectoid temperature of the Fe–N/Fe–N–C solid solution) are of great technological interest [1]: (i) The nitride/carbonitride compound layers (several tens of  $\mu\text{m}$  thick) can cause distinct improvement in chemical (corrosion) and mechanical (wear) properties of the workpieces [2]. (ii) Underneath the compound layer a diffusion zone (several hundreds of  $\mu\text{m}$  thick) develops, enriched with interstitial nitrogen and carbon which is responsible for great enhancement of the fatigue endurance [2].

Although nitriding/nitrocarburising treatments have been widely applied since the beginning of the twentieth century, fundamental understanding of important phase transformations and phase equilibria occurring in the metastable<sup>6.1</sup> Fe–N–C system is lacking. One controversially discussed aspect of the Fe–N–C system (the metastable Fe–N–C system is meant throughout) is the possible existence of the two-phase equilibrium  $\alpha$  ( $\alpha$ -Fe, ferrite) +  $\varepsilon$  ( $\varepsilon$ -Fe<sub>3</sub>(N,C)<sub>1+x</sub>) ( $\alpha$  +  $\varepsilon$  two-phase regions do *not* exist in the binary systems Fe–N and Fe–C) and, if this equilibrium occurs, in which temperature range it can be met. The possible occurrence of an  $\alpha$  +  $\varepsilon$  two-phase equilibrium is closely related with the possible occurrence of an invariant (fixed temperature at constant pressure) transition reaction



at a temperature  $T_i$ .

Numerous studies on the constitution of the ternary phase diagram Fe–N–C have been carried out (e.g. Refs. [5-13]). These studies were usually directly based on experiments but also on evaluations of experimental data adopting thermodynamic models. The earliest work by Jack [5] was based on the examination of nitrocarburised iron powders leading to proposals for homogeneity ranges of various phases in the Fe–N–C system. Later, Naumann and Langenscheid [6] presented the first “real”

---

<sup>6.1</sup> Metastable means that all solid-state equilibria considered are metastable with respect to decomposition in Fe, N<sub>2</sub> and graphitic C, e.g. see Refs. [3,4].

phase diagrams. These were derived from experiments performed with iron powders and iron foils nitrocarburised in NH<sub>3</sub>/H<sub>2</sub>/CO gas mixtures and investigated by chemical and X-ray diffraction (XRD) analyses. The interpretation by Naumann and Langenscheid [6] relies on the occurrence of an invariant eutectoid reaction



at 838 K. A two-phase equilibrium  $\alpha + \varepsilon$  and/or the invariant transition reaction given by Eq. (6.1) were not reported in this work [6]. A newer compilation by Raghavan [7] is compatible with this interpretation.

Apparently inconsistent with the above results, in a number of works the growth of  $\varepsilon$  grains (or even monophase  $\varepsilon$ ) on  $\alpha$  substrates or adjacent to the surface of pearlitic substrates (conversion of cementite into  $\varepsilon$ ) was observed upon nitriding or nitrocarburising at  $T_1 = 843 \text{ K} - 853 \text{ K}$  [14-22]. This could in principle be taken as evidence for the occurrence of an  $\alpha + \varepsilon$  two-phase equilibrium at the applied nitrocarburising temperatures, provided local (near) equilibrium holds between the solid phases at the  $\alpha/\varepsilon$  interface. This interpretation, which would be in contradiction to that of Naumann and Langenscheid [6], was rejected by several authors. These authors instead brought forward sometimes unclear, kinetic arguments, without going into detail, in order to reconcile the obtained results with the phase equilibria of the Fe–N–C system reported by Naumann and Langenscheid [6]: One example is Gérardin et al. [14,15] who produced monophase  $\varepsilon$  layers on  $\alpha$  by plasma nitrocarburising departing from a N<sub>2</sub>/H<sub>2</sub>/CH<sub>4</sub> gas mixture in a small temperature range of 843 K – 848 K. Matauschek and Trenkler [16] as well as Somers et al. [17] observed  $\varepsilon$  grains in contact with  $\alpha$  after salt-bath nitrocarburising at 843 K [16] and 853 K [17]. Upon nitriding a pearlitic substrate at 843 K using a NH<sub>3</sub>/H<sub>2</sub> gas mixture, Mittemeijer et al. [18] reported on the direct conversion of cementite lamellae into  $\varepsilon$ . Performing gas-nitrocarburising experiments at 843 K [19] and 853 K [20], Somers and Mittemeijer [19] and Wells and Bell [20] reported, in particular, a remarkably low nitrogen content in the observed  $\varepsilon$  phase at the interface  $\alpha/\varepsilon$ . Later, on the basis of gas-nitrocarburising experiments conducted at 843 K and 853 K using a N<sub>2</sub>/NH<sub>3</sub>/CO gas mixture, Wells reported [21,22] for lower CO contents an  $\varepsilon/\gamma'$  double layer and for higher CO

contents a monophasic  $\varepsilon$  layer on the substrate. Thermodynamic calculations by Zuyao and Lin [8]<sup>6.2</sup> indeed resulted in an extended (with respect to Naumann and Langenscheid [6]) solid solubility region of the  $\varepsilon$  phase at 853 K. They partially comprise the low N + C contents reported for pure  $\varepsilon$ -phase layers by Wells and Bell [20]. However, the phase diagram reported by Zuyao and Lin [8] does not contain a two-phase equilibrium  $\alpha + \varepsilon$ .

Other authors, however, interpreted the occurrence of monophasic  $\varepsilon$  in contact with  $\alpha$  as indicative for the occurrence of an  $\alpha + \varepsilon$  equilibrium. The occurrence of local equilibrium at the interface was taken for granted, and it was concluded that the ternary phase diagram Fe–N–C proposed by Naumann and Langenscheid [6] should be revised. Phase-diagram calculations by Slycke et al. [9] resulted in a phase diagram containing for the first time the two-phase region  $\alpha + \varepsilon$ . This work is based on experimental observations (among others, Wells and Bell [20] and Wells [21,22]) and adopts a tentative temperature of  $T_t = 823$  K for the transition reaction given by Eq. (6.1). Below this  $T_t$  the three-phase equilibrium  $\alpha + \gamma' + \text{cementite}$ , as reported by Naumann and Langenscheid for 773 K [6], occurs. Furthermore, in contrast to Eq. (6.2), the formation of the  $\gamma$  phase, from  $\alpha + \varepsilon + \gamma'$  at a single temperature of 858 K was assumed to occur. As a consequence, in the proposed phase diagram a two-phase field  $\alpha + \varepsilon$  occurs between 823 K and 858 K. Later, thermodynamic calculations by Du and Hillert [10] and Du [12] predicted the invariant transition reaction given by Eq. (6.1) to occur at lower temperatures:  $T_t = 820.6$  K [10] and even as low as  $T_t = 782$  K [12]. The thermodynamic calculations are mainly based on experimental phase boundaries for several two-phase and three-phase equilibria at various temperatures. The data pertaining to these calculations were taken from among others Somers et al. [17]. Specific values for the temperatures of invariant reactions, e.g. of  $T_t$  were not a priori adopted. Independent thermodynamic calculations by Huchel and Kunze [11] and by Kunze [13], using experimental observations from gas-nitrocarburising experiments with steels at 863 K (using a  $\text{NH}_3/\text{N}_2/\text{CO}_2$  gas mixture), suggested the

---

<sup>6.2</sup> It is beyond the scope of the present paper to discuss details of the thermodynamic models employed in the different thermodynamic calculations.

occurrence of the two-phase equilibrium  $\alpha + \varepsilon$  in the temperature range of at least 851 K – 871 K. The invariant transition reaction given by Eq. (6.1) was not discussed in Refs. [11,13].

All the experimental research reported in the literature was performed by solely analysing the compound layers resulting from nitrocarburising treatments of pure  $\alpha$  or iron-carbon alloys or of ferritic steels or of iron powders<sup>6.3</sup>. Whereas it is often assumed that at the interface compound layer/ $\alpha$  substrate equilibrium states are practically realised, the composition at the sample surface and therewith the average composition of N and C within the specimen is often observed to change treatment-time dependently [17,19,24,25]. This may hint at a large effect of reaction kinetics (at least at the surface, cf. Refs. [26,27]) on the evolving microstructure of the Fe–N–C compound layers. Hence, it may be difficult, if not even impossible, to draw unambiguous conclusions concerning the constitution of the equilibrium Fe–N–C phase diagram from experiments based on (only, simple) nitrocarburising of iron-based substrates.

In order to circumvent the above indicated effects of reaction kinetics and to conclude the discussion on the (meta) stability of the  $\alpha + \varepsilon$  two-phase equilibrium another experimental strategy has been followed by the present authors. After nitrocarburising of pure iron substrates at  $T_1$  (considered to be the *primary* (thermochemical) *annealing* treatment), *secondary annealing* experiments under inert-gas atmosphere were performed at various annealing temperatures  $T_2$ . The purpose of

---

<sup>6.3</sup> Nitrocarburising of bulk materials leads to more or less textured compound layers at the surface, containing stresses and concentration gradients. In contrast, nitrocarburising of iron powder can lead to (macro)stress free and homogeneous single-phase powder samples [23]. Such nitride, carbonitride or carbide powders can be studied very well by powder diffraction techniques without that effects like texture, (macro)stresses and concentration gradients have to be taken into account in the interpretation of the diffraction patterns. Furthermore, such powders are well suited for conventional chemical-analysis techniques, which are especially very valuable to characterise the composition and temperature ranges of single-phase regions of different phases. Compound layers, in particular annealed (after nitrocarburising) ones, as demonstrated in this paper, are, however, better suited for studying (solid-state) phase equilibria. This is due to the fact that the arrangement of different solid phases in equilibrium with each other can be observed better in a massive microstructure.

the secondary annealing experiments is to establish chemical equilibrium states (neglecting, in the specimens studied, possible effects of macrostress variations on the application of the phase rule) by levelling off concentration/chemical potential gradients in the compound layer and thereby to establish equilibrium between the different compound-layer phases and the (ferritic) substrate (saturated or nearly saturated with interstitial N and C [28]). Thus, a dependence on the nitrocarburising process used to produce the compound layer, which involves mass transfer into/out of the solid, is excluded. As a result of the observed developing microstructures and their discussion in terms of constitution rules for the ternary phase diagram Fe–N–C, for the first time the existence of the two-phase equilibrium  $\alpha + \varepsilon$  could unambiguously be proven by tracing the appearance of the invariant transition reaction given by Eq. (6.1).

## 6.2 Experimental

An  $\alpha$ -iron cast rod (Alfa Aesar, 99.98 wt.%) was cold rolled on both sides to a thickness of 1 mm. Rectangular pieces of 20 mm  $\times$  25 mm were cut, ground, polished (final stage 1  $\mu$ m diamond), cleaned ultrasonically in ethanol and recrystallised at 973 K for 2 h under a hydrogen flow of 200 ml min<sup>-1</sup> followed by polishing and cleaning ultrasonically in ethanol.

Nitrocarburising of the foils prepared as described above was carried out in a vertical quartz-tube furnace equipped with a water (flushed with N<sub>2</sub>) container for quenching. Using a quartz fibre, which can be mechanically destroyed before quenching, the specimen was suspended in the middle of the furnace where the process temperature was controlled within  $\pm 1$  K. The gas atmosphere was composed of carbon monoxide (99.97 vol.%) as a carbon-providing medium, hydrogen (99.999 vol.%), ammonia (99.999 vol.%) as a nitrogen-providing medium and nitrogen (99.999 vol.%) as inert gas. The gas fluxes were controlled by mass-flow controllers, adjusting an overall linear flow rate of 13.5 mm s<sup>-1</sup> (calculated for the gas volume at room temperature) through the quartz retort (diameter 28 mm). This flow rate was chosen such that ammonia dissociation, which would change the composition of the gas atmosphere, can be neglected.

In order to investigate the treatment-time dependent evolution of the microstructure, two sets of nitrocarburising experiments (variable treatment time) were conducted using different nitrocarburising parameters: (a)  $T_1 = 823$  K, 22 vol.%  $\text{NH}_3$ , 58 vol.%  $\text{H}_2$  and 20 vol.%  $\text{CO}$  (nitriding potential<sup>6.4</sup>  $r_{\text{N}} = 0.5 \text{ atm}^{-1/2}$ ); (b)  $T_1 = 853$  K, 18 vol.%  $\text{NH}_3$ , 58 vol.%  $\text{H}_2$ , 20 vol.%  $\text{CO}$  and 4 vol.%  $\text{N}_2$  (nitriding potential  $r_{\text{N}} = 0.4 \text{ atm}^{-1/2}$ ). Two nitrocarburised specimens were investigated in particular: Sample A was treated for 10 h employing condition (a) and sample B was treated for 1 h employing condition (b).

Parts of both sample A and sample B were sealed in an evacuated quartz ampule under an argon pressure of 300 mbar and were subjected to secondary annealing experiments performed in a resistance furnace for 2 h (additionally some experiments with 24 h annealing time) at  $T_2 = 823$  K, 833 K, 843 K or 853 K (controlled within  $\pm 3$  K). After annealing, the specimens were quenched in water by crushing the quartz ampule.

Both the as-nitrocarburised specimens and the secondary-annealed specimens were cut into three pieces used for optical microscopy, X-ray diffraction (XRD) and Electron Backscattering Diffraction (EBSD), respectively.

For optical microscopy (Zeiss AxioPhot microscope) some specimens were covered with an electrodeposited protective nickel layer using a Watts bath [30,31] at 333 K in order to avoid mechanical damage at the surface and to achieve a sufficient sharpness at the sample surface in the micrograph. After embedding (Polyfast, Buehler GmbH), grinding and polishing (final stage 1  $\mu\text{m}$  diamond) the specimens were etched using 1 vol.% Nital containing 0.1 vol.%  $\text{HCl}$  [22]. For phase identification, some specimens were additionally stained using an alkaline potassium permanganate solution (1 g  $\text{NaOH}$ , 1 g  $\text{KOH}$  and 4 g  $\text{KMnO}_4$  per 100 ml distilled water) at 328 K as described elsewhere [29,32] (cf. *chapter 2*) of which the effect is similar to that of a Murakami solution [30,32]. Since the degree of staining increases with the carbon

---

<sup>6.4</sup> The nitriding potential determines the chemical potential of nitrogen in the gas atmosphere [4]. Considering gas atmospheres composed of  $\text{NH}_3/\text{H}_2/\text{CO}/(\text{N}_2)$ , as used in the present work, no value for a carburising potential can be given, as the usually employed formulation for the carburising potential yields infinity [29] (cf. *chapter 2*).

content of the respective phase, it is possible to distinguish  $\gamma'$ ,  $\epsilon$  and cementite. Whereas  $\gamma'$  remains unstained (indicating the very low solubility of carbon in  $\gamma'$  [6]), slight staining of  $\epsilon$  occurs, indicated by a brown colour in the micrograph, and cementite, due to its high carbon content, becomes severely stained indicated by a dark brown or even blue colour in the micrograph.

Phase identification was conducted by means of X-ray diffraction using a PANalytical X'Pert Multi-Purpose Diffractometer equipped with a graphite monochromator in the diffracted beam utilising  $\text{CoK}_\alpha$  radiation and Bragg–Brentano geometry. During the measurements the specimens were rotated around their surface normal in order to achieve better crystallite statistics. For lattice-parameter determination a thin layer of Si standard powder (suspended in isopropanol) was deposited on the sample surface for (internal) calibration of the diffraction-peak positions in the XRD pattern.

EBSD measurements were carried out on cross-sections in order to identify the different phases which are present in the microstructure. The specimens were embedded, ground and polished (final stage colloidal silica suspension OPS, Struers GmbH, for several hours). The quality of the cross-sectional surface preparation is crucial for the obtained results since mechanical deformation has a negative effect on the quality of the recorded Kikuchi patterns which have to be indexed for phase identification. For the EBSD measurements a Zeiss scanning electron microscope (LEO 438 VP) equipped with an EBSD system (TSL, EDAX, Inc.) and the software OIM 4.5 were used.

## 6.3 Results

### 6.3.1 Nitrocarburising experiments of set (a) ( $T_1 = 823 \text{ K}$ )

Nitrocarburising experiments of set (a) yielded a treatment-time dependent microstructure of the compound layer on the  $\alpha$ -Fe substrate. Whereas after 4 h a completely substrate-covering, massive cementite layer had formed, after 24 h a massive  $\gamma'$  layer was obtained.



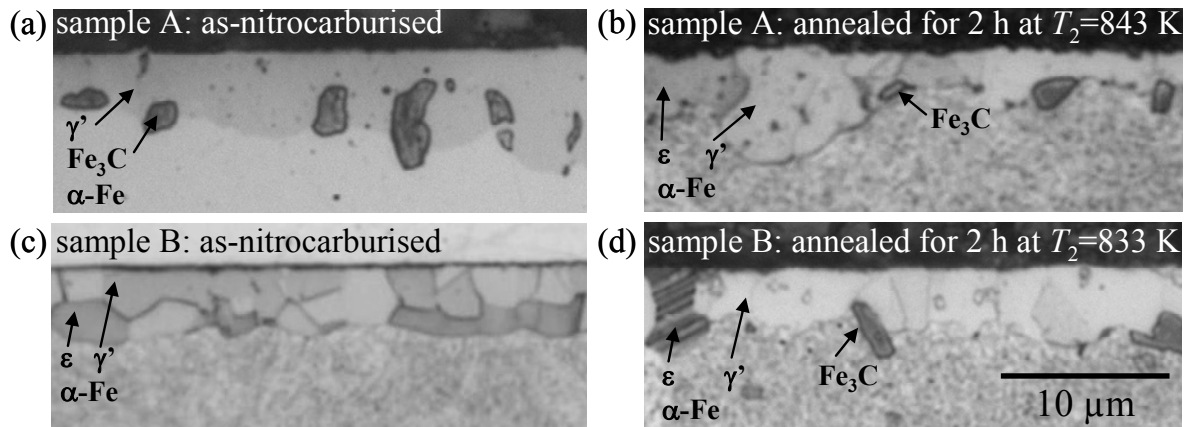


**Fig. 6.1:** Light optical microscopic images of metallographic cross-sections after etching with 1 vol.% Nital containing 1 vol.% HCl [22] and staining C-rich phases with an alkaline potassium permanganate solution [29,32]. (a) sample A nitrocarburised at  $T_1 = 823$  K (i.e. below the temperature  $T_i$  of the invariant transition reaction given by Eq. (6.1)) for 10 h with a gas atmosphere containing 22 vol.%  $\text{NH}_3$ , 58 vol.%  $\text{H}_2$  and 20 vol.% CO (nitriding potential  $r_N = 0.5 \text{ atm}^{-1/2}$ ). (b) sample A annealed for 2 h at  $T_2 = 843$  K (i.e. above  $T_i$ ). (c) sample B nitrocarburised at  $T_1 = 853$  K (i.e. above  $T_i$ ) for 1 h with a gas atmosphere containing 18 vol.%  $\text{NH}_3$ , 58 vol.%  $\text{H}_2$  and 20 vol.% CO and 4 vol.%  $\text{N}_2$  (nitriding potential  $r_N = 0.4 \text{ atm}^{-1/2}$ ). (d) sample B annealed for 2 h at  $T_2 = 833$  K (i.e. below  $T_i$ ).

For intermediate treatment times the compound layer consisted of both  $\gamma'$  and cementite. Such a sample as obtained after 10 h at  $T_1 = 823$  K, i.e. with a compound layer constituted of  $\gamma'$  and cementite, served as a sample A (Figs. 6.1a and 6.4a).

### 6.3.2 Secondary annealing experiments of sample A

Secondary annealing experiments on sample A at  $T_2 = T_1 = 823$  K and  $T_2 = T_1 + 10$  K = 833 K for 2 h showed that the microstructure remained practically unaffected. However, upon secondary annealing for 2 h at  $T_2 = T_1 + 20$  K = 843 K and for 2 h at  $T_2 = T_1 + 30$  K = 853 K besides  $\gamma'$  and cementite new,  $\epsilon$  was formed in the compound layer. This was demonstrated by means of optical microscopy (Fig. 6.1b) and XRD measurements (Fig. 6.4b). Secondary annealing experiments performed at  $T_2 = T_1 + 20$  K = 843 K and  $T_2 = T_1 + 30$  K = 853 K with a longer annealing time of 24 h instead of 2 h showed that only  $\epsilon$  and  $\gamma'$  remained as constituents of the compound layer on the  $\alpha$  substrate, i.e. cementite was completely consumed.

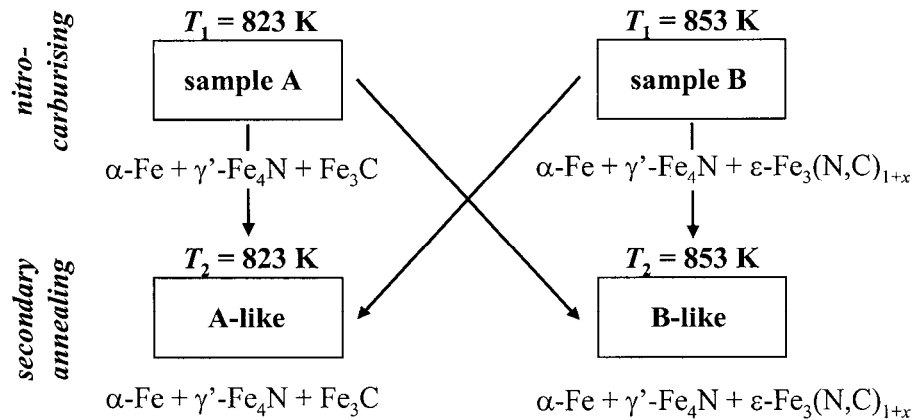


**Fig. 6.2:** Scheme summarising the states (phase constituents) observed for samples A and B in the as-nitrocarburised state and after secondary annealing experiments conducted at different temperatures  $T_2$  establishing three-phase equilibria. Upon secondary annealing above  $T_t$ , the microstructure of sample A is transformed into one similar to that of sample B. Vice versa, upon annealing below  $T_t$ , the microstructure of sample B is transformed into one similar to that of sample A.

Thus, by secondary annealing of sample A at the nitrocarburising temperature of sample B (853 K) a specimen with a microstructure similar to that of sample B was obtained (Fig. 6.2).

### 6.3.3 Nitrocarburising experiments of set (b) ( $T_1 = 853 \text{ K}$ )

Nitrocarburising experiments of set (b) yielded a treatment-time dependent microstructure evolution of the compound layer on the  $\alpha$  substrate. Whereas after 0.17 h a massive cementite layer had formed, after 0.5 h a microstructure containing cementite and  $\varepsilon$  (with  $a$  and  $c$  lattice parameters:  $a = 4.610 \text{ \AA}$ ,  $c = 4.350 \text{ \AA}$ ) was obtained. After 24 h the compound layer consisted only of  $\gamma'$ . For intermediate treatment times (1 h – 24 h) the compound layer was composed of both  $\varepsilon$  and  $\gamma'$ <sup>6.5</sup> with the phase fraction of  $\varepsilon$  in the compound layer decreasing with increasing treatment time. Such a sample as obtained after 1 h at  $T_1 = 853 \text{ K}$ , i.e. with a compound layer constituted of  $\varepsilon$  and  $\gamma'$ , served as a sample B (Figs. 6.1c, 6.3a and 6.4c).

<sup>6.5</sup>  $\varepsilon$  in contact with both  $\alpha\text{-Fe}$  substrate and  $\gamma'$  (adjacent to the sample surface) (Fig. 6.1c), which morphology is never observed for pure iron nitride layers; see also introduction.

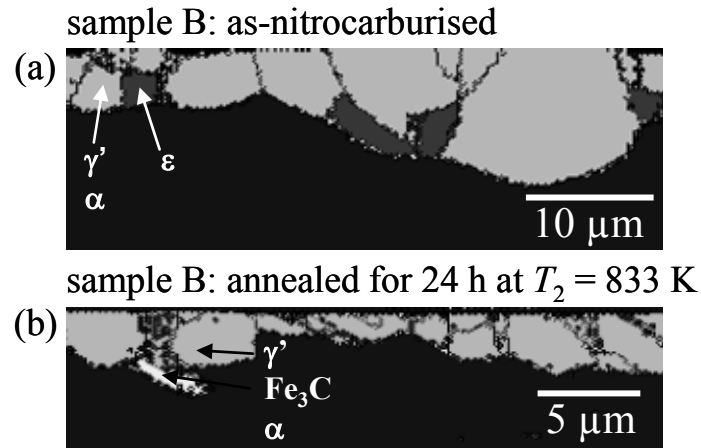


**Fig. 6.3:** Cross-sectional EBSD images of sample B (a) as-nitrocarburised and (b) annealed for 24 h at  $T_2 = 833$  K (below  $T_1$ ). The different greyscales in the micrographs represent the different phases present in the microstructure,  $\alpha$  (black),  $\gamma'$  (grey),  $\epsilon$  (dark grey) and cementite (light grey) (as identified by EBSD; spatial resolution is about  $0.2 \mu\text{m}$ ; phase identification along grain boundaries (black lines) is difficult as indicated by dots of different colours in these regions).

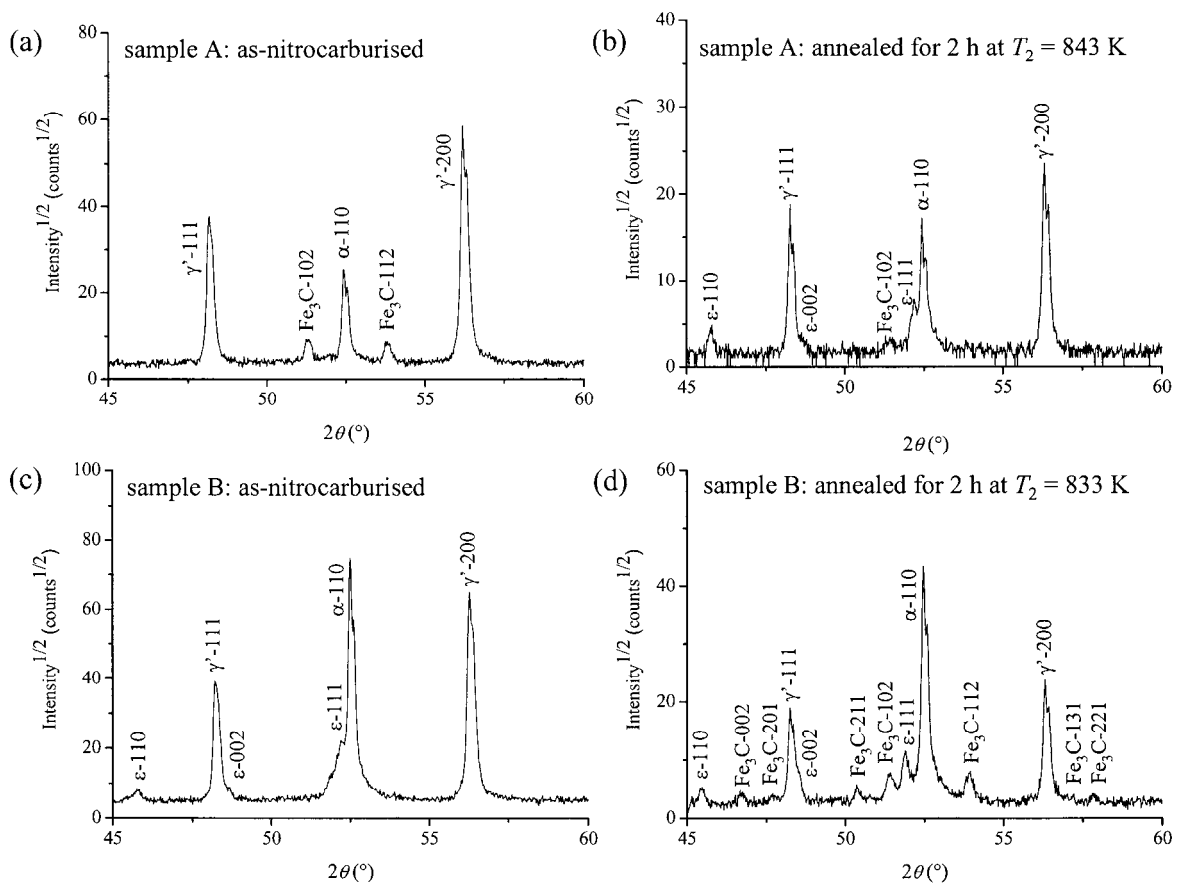


**Fig. 6.4:** X-ray diffraction patterns (a) sample A, as-nitrocarburised, (b) sample A after secondary annealing at  $T_2 = 843$  K (above  $T_1$ ), (c) sample B, as-nitrocarburised, (d) sample B after secondary annealing at  $T_2 = 833$  K (below  $T_1$ ).

### 6.3.4 Secondary annealing experiments of sample B

The microstructure of sample B remained unchanged upon annealing for 2 h at  $T_2 = T_1 = 853$  K and  $T_2 = T_1 - 10$  K = 843 K. However, upon annealing for 2 h at  $T_2 = T_1 - 20$  K = 833 K and for 2 h at  $T_2 = T_1 - 30$  K = 823 K new cementite phase was formed in the compound layer which was originally composed of  $\gamma'$  and  $\epsilon$  only. This was demonstrated by optical microscopy (Fig. 6.1d) and XRD measurements (Fig. 6.4d). Phase identification performed by means of EBSD after secondary annealing for a longer annealing time of 24 h at  $T_2 = T_1 - 20$  K = 833 K revealed that only cementite and  $\gamma'$  remained as constituents of the compound layer on the  $\alpha$  substrate, i.e.  $\epsilon$  was completely consumed (Fig. 6.3b). Thus, by secondary annealing of sample B at the nitrocarburising temperature of sample A (823 K) a specimen with a microstructure similar to that of sample A was obtained (Fig. 6.2).

## 6.4 Discussion

### 6.4.1 Nitrocarburising experiments at $T_1 = 823$ K and $T_1 = 853$ K

Nitrocarburising of pure iron at both  $T_1 = 823$  K and  $T_1 = 853$  K showed that the microstructure of the compound layer varies as a function of the treatment time. At very short treatment times, a pure cementite layer was obtained at both  $T_1 = 823$  K and  $T_1 = 853$  K. For very long treatment times, a massive, pure  $\gamma'$  compound layer resulted for both treatment temperatures. Whereas for  $T_1 = 823$  K as an intermediate state a compound layer composed of cementite and  $\gamma'$  was obtained, for  $T_1 = 853$  K a compound layer in the intermediate state was composed of  $\epsilon$  and  $\gamma'$ . Evidently, the nitrocarburising treatment-time dependent microstructural evolution starts with carbon-rich phases and develops into the direction of carbon-poor phases<sup>6.6</sup>, which agrees with some observations made previously [17,24,25].

---

<sup>6.6</sup> Apparently, upon nitrocarburising for longer treatment times, carbon, initially absorbed (possibly because the nitrogen uptake starts slowly [3,24]), and incorporated in cementite and  $\epsilon$ , re-escapes the specimen through its outer surface.

A treatment-time dependent microstructural (phase-constitutional) evolution of the compound layer indicates that under (the present) nitrocarburising conditions no (near) local equilibrium is established between the gas atmosphere and the sample surface for the treatment-time range considered. Thus, complicated concentration-profile developments and associated diffusion processes are expected to occur in the compound layer, which warns against an overhasty assumption of local solid-state equilibria (see section 6.4.2).

By means of XRD measurements, lattice parameters for  $\epsilon$  in the compound layer of sample B, as-nitrocarburised, were determined:  $a = 4.610 \text{ \AA}$  and  $c = 4.350 \text{ \AA}$  (referring to the hexagonal superstructure with  $a = 3^{1/2}a_{\text{hcp}}$  and  $c = c_{\text{hcp}}$  when  $a_{\text{hcp}}$  and  $c_{\text{hcp}}$  pertain to the hcp arrangement of Fe atoms; superstructure reflections were not detected, probably due to a too low intensity). The total interstitial content may be calculated from the observed lattice-parameter values preliminary adopting equations for the N-content dependence of  $a$  and  $c$  determined from quenched powder specimens [33]. This involves a considerable extrapolation with respect to the composition of the  $\epsilon$  phase. The equations were only determined for N contents larger than 25 at.% N. Moreover, as an approximation, carbon is then supposed to have the same effect on the iron-lattice expansion due to interstitial dissolution. On this basis, according to the lattice parameter  $a$ , a total interstitial content (N + C) of 17.9 at.% and according to the lattice parameter  $c$  a total interstitial content of 20.9 at.% was calculated. It was observed previously for pure nitride compound layers [34] that the interstitial content calculated using the equations from Ref. [33] is systematically higher for results obtained from lattice parameter  $c$  than from lattice parameter  $a$ . This can be ascribed to the effects of residual, internal stresses and concentration gradients within the  $\epsilon$ -nitride phase in compound layers, as compared to homogeneous  $\epsilon$ -nitride powders used to derive the equations in Ref. [33].

The extremely low interstitial content (N + C) of the  $\epsilon$  phase in the compound layer as determined here (17.9/20.9. at.%) is even lower than the one pertaining to  $\gamma'$ . In the *binary* Fe–N system [35]  $\epsilon$  phase with such a low amount of N is metastable (at  $T < 923 \text{ K} - 953 \text{ K}$ ); its composition at the nitrocarburising temperature is well outside the  $\epsilon$  field. However, the result obtained here for the interstitial content in the

ternary  $\varepsilon$  phase in the compound layer is in good agreement with values for the interstitial content determined for  $\varepsilon$ -carbonitride in compound layers produced at similar treatment temperatures as in the present work. These compound layers were produced for example by gaseous nitrocarburising at 853 K [20] resulting in 20.4 at.% (N + C), determined by Auger Electron Spectroscopy (AES) or by salt-bath nitrocarburising at 853 K [17] resulting in 16.4 at.% N and 4.24 at.% C (20.6 at.% N + C), determined by Electron Probe Microanalyses (EPMA).

#### 6.4.2 Secondary annealing experiments

The principle of the secondary annealing experiments can be understood as follows [36]: In the *as-nitrocarburised* state, the phases in the quenched compound layer exhibit concentration gradients of N and C due to the diffusion processes during the nitrocarburising reaction. Upon secondary annealing for sufficiently long time<sup>6,7</sup>, solid-state equilibria can be established in the microstructure composed of the  $\alpha$  substrate (saturated or nearly saturated with interstitial N and C [28]) and the compound layer. Concentration gradients of N and C then are also eliminated. The eventual equilibrium state is determined by the secondary annealing temperature  $T_2$  and the average N and C content of the specimen, including both the phases of the compound layer and the  $\alpha$  substrate which is saturated (or nearly saturated) with N and C [28].

For the present specimens the estimated average Fe, N, C contents of the whole specimen are located in the Fe-rich corner of the ternary system Fe–N–C, with  $\alpha$  being most probable always one of the resulting equilibrium phases of the prevailing two- or three-phase equilibrium.

Secondary annealing at  $T_2 \approx T_1$  for both sample A (823 K – 833 K) and B (853 K – 843 K) showed that the phase constitution of the microstructure remained in principle the same. This indicates that (near) local equilibrium at the solid–solid

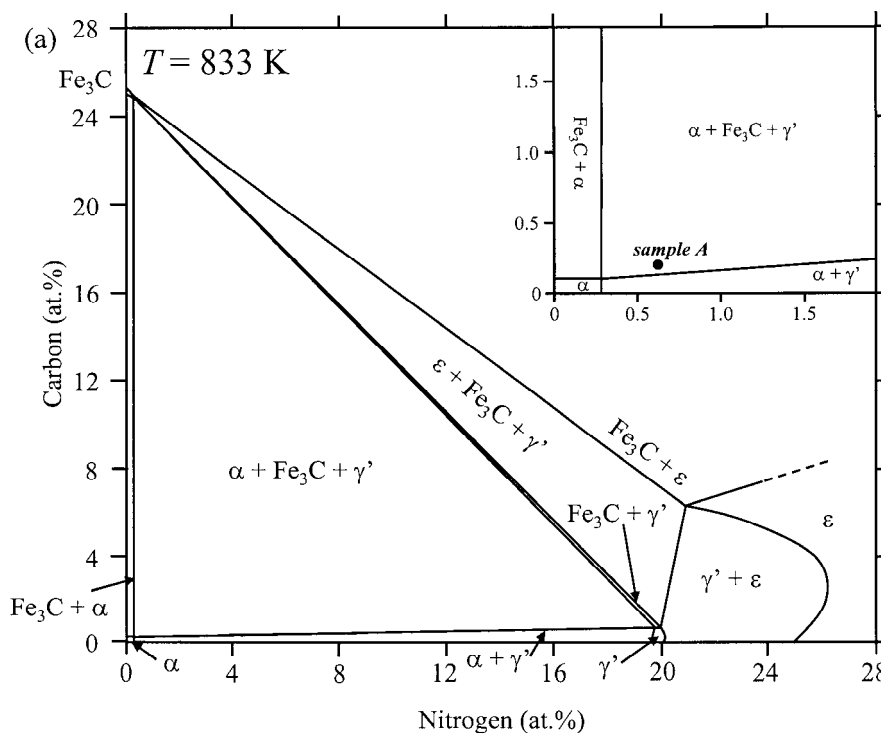
---

<sup>6,7</sup> N loss to the atmosphere, changing the overall composition of the specimen, becomes significant for relatively long-time secondary annealing. For very short secondary annealing times, equilibrium states cannot fully be established, due to diffusion/reactions rates of finite magnitudes.

interfaces in the specimen (compound layer/ $\alpha$  substrate) was established upon nitrocarburising and before secondary annealing. The secondary annealing at a temperature close to the nitrocarburising temperature then causes a compositional homogenisation of the phases present in the compound layer. Eventually, genuine three-phase equilibria,  $\alpha + \gamma' + \text{cementite}$  at 823 K – 833 K (sample A) and  $\alpha + \gamma' + \varepsilon$  at 853 K – 843 K (sample B), are established.

Examination of states produced by secondary annealing experiments of both sample A and B at  $|T_2 - T_1| \geq 20$  K for 2 h showed the formation of new  $\varepsilon$  phase above 843 K for sample A and the formation of new cementite phase below 833 K for sample B. These results confirm the equilibrium-phase constitutions indicated above and demonstrate that the invariant transition reaction given by Eq. (6.1) occurs at a single temperature in the narrow temperature range of 833 K  $< T_i <$  843 K.

After an annealing time of 2 h the invariant transition reaction has proceeded incompletely, only the onset of the formation of the new phases was observed. However, the very observation of the onset of the invariant transition reaction demonstrates that (by variation of  $T_2$ )  $T_i$  was indeed passed. Applying longer annealing times (24 h) completed the reaction.



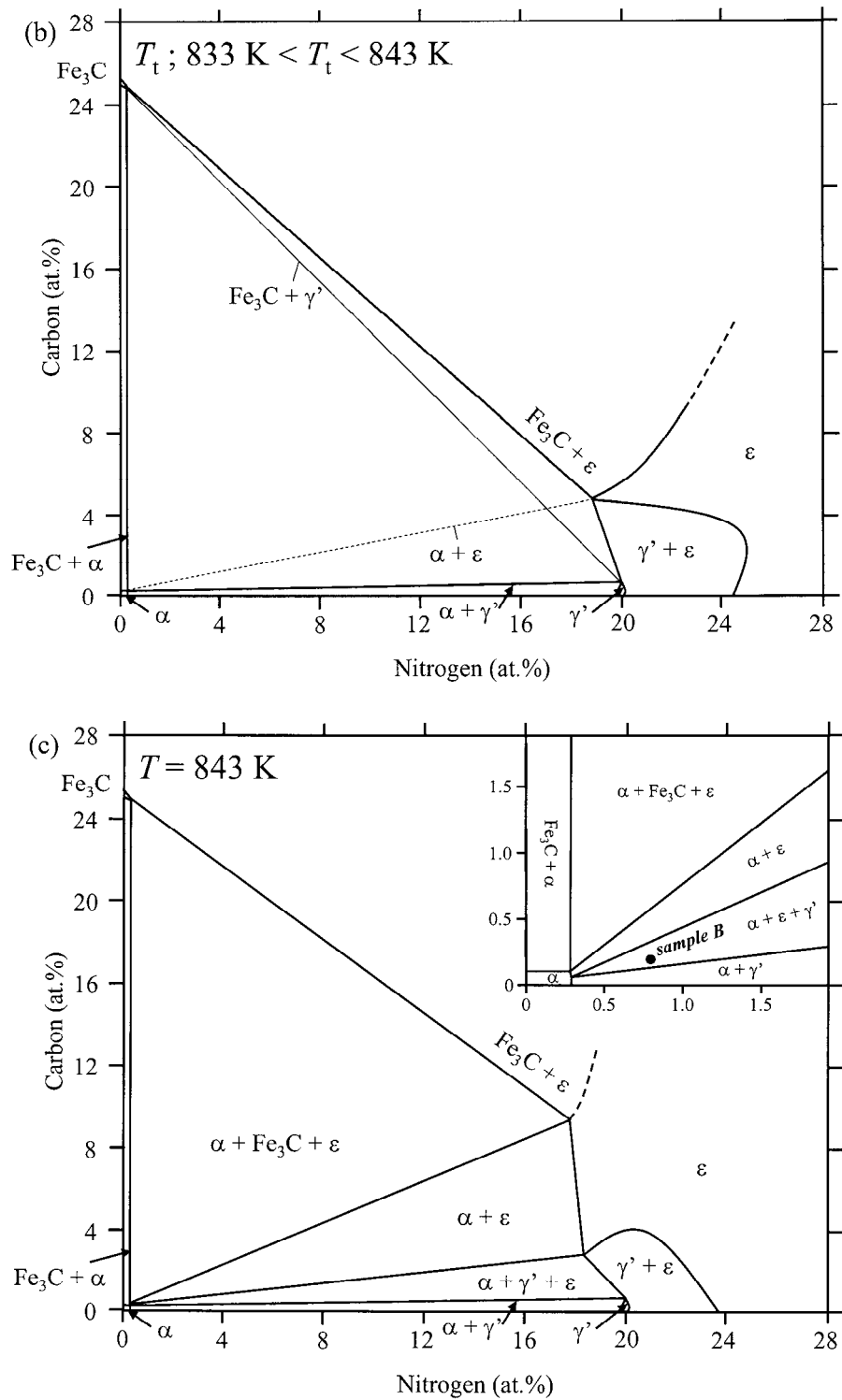


**Fig. 6.5:** Isothermal sections of the Fe–N–C ternary phase diagram at 1 atm (enlarged part in the upper right corner). (a) 833 K, below  $T_t$  (phase boundaries deduced approximately according to the isothermal section at 773 K of Ref. [12]). (b)  $T_t$  ( $833 \text{ K} < T_t < 843 \text{ K}$ ) (phase boundaries estimated). The thin continuous line and the thin dashed line indicate the invariant transition reaction given by Eq. (6.1). (c) 843 K, above  $T_t$  (phase boundaries deduced approximately according to the isothermal section at 843 K – 853 K of Ref. [9]).



The occurrence of a genuine three-phase equilibrium of the ternary Fe–N–C system at a certain temperature (and at constant pressure) implies, at the same temperature (and at the same pressure), the existence of the three adjoining two-phase equilibria which can be constructed out of the phases of the observed three-phase equilibria [37]. Hence, the two-phase equilibrium  $\alpha + \varepsilon$  is shown to exist above  $T_t$  due to the experimental observation of the three-phase equilibrium  $\alpha + \varepsilon + \gamma'$  above  $T_t$  as an equilibrium state. This leads to the proposed schematic isothermal sections of the system Fe–N–C in Fig. 6.5.

According to the present work,  $T_t$  is located between 833 K and 843 K. This agrees well with Ref. [9] where the invariant transition reaction given by Eq. (6.1) has been proposed to occur tentatively at 823 K. The result obtained in Ref. [10] where  $T_t$  has been given as 820.6 K also agrees fairly with the experimental result of this work, whereas the result obtained in Ref. [12] where  $T_t$  has been given at 782 K is considered to be erroneous. In Refs. [11,13] it has been mentioned that monophasic  $\varepsilon$  layers can be produced at about 851 K – 871 K employing a carbon activity of  $a_C = 1.2$ . The results of the present work indicate that pure  $\varepsilon$  in direct contact with  $\alpha$  can be obtained at even lower temperatures, but above  $T_t$ .

As a final remark it is concluded that explanations for the observation of  $\varepsilon$ -carbonitride grains, or even monophasic  $\varepsilon$ -carbonitride layers on ferritic ( $\alpha$ -Fe) substrates [14-22], on a kinetic basis, not recognising the occurrence of a genuine two-phase equilibrium  $\alpha + \varepsilon$ , are incorrect. However, an exemplary reinterpretation of the experimental data in Ref. [18] by the present authors showed that these results can be accommodated to the calculated potential phase diagram in Ref. [13]. This indicates that experimental results which were originally explained by the authors on a kinetic basis can be reconciled with calculated phase diagrams containing a genuine  $\alpha + \varepsilon$  two-phase equilibrium [9-13].

## 6.5 Conclusions

1. Secondary annealing experiments after a thermochemical heat treatment, such as nitrocarburising, are a powerful method for the study of solid-state phase equilibria, here for the Fe–N–C system.
2. By means of systematic secondary annealing experiments at  $T_2$  it was shown experimentally that the invariant transition reaction  $\gamma' + \text{cementite} \rightarrow \alpha + \varepsilon$  occurs at a specific temperature  $T_t$  (at 1 atm) which lies in the range  $833 \text{ K} < T_t < 843 \text{ K}$ . Below  $T_t$  the three-phase equilibrium  $\alpha + \gamma' + \text{cementite}$  occurs; above  $T_t$  the three-phase equilibrium  $\alpha + \varepsilon + \gamma'$  occurs.
3. The existence of the two-phase equilibrium  $\alpha + \varepsilon$  in the Fe–N–C system was demonstrated by the observation above  $T_t$  of the three-phase equilibrium  $\alpha + \varepsilon + \gamma'$  which has to adjoin to this two-phase equilibrium in the ternary phase diagram.
4. The results presented in the present paper can have a pronounced technological importance. Often, the production of pure and massive  $\varepsilon$  surface layers on iron-based workpieces is desired, e.g. in view of demands concerning the adhesion and corrosion properties [38] as well as for the tribological performance of a workpiece [38,39]. The present results indicate that such layers can in principle be produced by nitrocarburising above  $T_t$  ( $833 \text{ K} < T_t < 843 \text{ K}$ ). The low interstitial content of such  $\varepsilon$  layers is also advantageous because then the thermodynamic driving force for dissociation in Fe,  $\text{N}_2$  (pore formation) and C, is relatively small.

## References

- [1] M.A.J. Somers: Heat Treat. Met. 27 (2000) 92.
- [2] P.M. Unterweiser, A.G. Gray (Eds.): Source Book on Nitriding, ASM, Metals Park, OH (1977).
- [3] W. Schröter: Wiss. Z. d. Techn. Hochsch. Karl-Marx-Stadt 24 (1982) 795.
- [4] E.J. Mittemeijer, J.T. Slycke: Surf. Eng. 12 (1996) 152.
- [5] K.H. Jack: Proc. Roy. Soc. A 195 (1948) 41.

- [6] F. K. Naumann, G. Langenscheid: *Arch. Eisenhüttenwesen* 36 (1965) 583.
- [7] V. Raghavan: *Trans. Indian Inst. Met.* 37 (1984) 293.
- [8] X. Zuyao, L. Lin: *Mat. Sci. Tec.* 3 (1987) 325.
- [9] J. Slycke, L. Sproge, J. Ågren: *Scand. J. Metallurgy* 17 (1988) 122.
- [10] H. Du, M. Hillert: *Z. Metallkde.* 82 (1991) 310.
- [11] U. Huchel, J. Kunze: *Härterei-Tech. Mitt.* 46 (1991) 351.
- [12] H. Du: *J. Phase Eq.* 14 (1993) 682.
- [13] J. Kunze: *Härterei-Tech. Mitt.* 51 (1996) 348.
- [14] D. Gérardin, H. Michel, J.P. Morniroli, M. Gantois: *Mémoires Sci. Rev. Mét.* 77 (1977) 457.
- [15] D. Gérardin, H. Michel, M. Gantois: *Scr. Metall.* 11 (1977) 557.
- [16] J. Matauschek, H. Trenkler: *Härterei-Tech. Mitt.* 32 (1977) 4.
- [17] M.A.J. Somers, P.F. Colijn, W.G. Sloof, E.J. Mittemeijer: *Z. Metallkd.* 81 (1990) 33.
- [18] E.J. Mittemeijer, W.T.M. Straver, P.F. Colijn, P.J. van der Schaaf, J.A. van der Hoeven: *Scr. Metall.* 14 (1980) 1189.
- [19] M.A.J. Somers, E.J. Mittemeijer: *Surf. Eng.* 3 (1987) 123.
- [20] A. Wells, T. Bell: *Heat Treat. Metals* (1983) 39.
- [21] A. Wells: *Thin Sol. Films* 128 (1985) L33.
- [22] A. Wells: *J. Mat. Sci.* 20 (1985) 2439.
- [23] A. Leineweber, J. Aufrecht, E.J. Mittemeijer: *Int. J. Mat. Res.* 97 (2006) 753.
- [24] M.A.J. Somers, E.J. Mittemeijer: *Härterei-Tech. Mitt.* 47 (1992) 5.
- [25] H. Du, M.A.J. Somers, J. Ågren: *Metall. Mater. Trans. A* 31A (2000) 195.
- [26] H.C.F. Rozendaal, E.J. Mittemeijer, P.F. Colijn, P.J. van der Schaaf: *Met. Trans. A* 14A (1983) 395.
- [27] E.J. Mittemeijer, M.A.J. Somers: *Surf. Eng.* 13 (1997) 483.
- [28] T. Liapina, A. Leineweber, E.J. Mittemeijer: *Scr. Mat.* 48 (2003) 1643.
- [29] T. Gressmann, M. Nikolussi, A. Leineweber, E.J. Mittemeijer: *Scr. Mat.* 55 (2006) 723.
- [30] P.F. Colijn, E.J. Mittemeijer, H.C.F. Rozendaal: *Z. Metallkd.* 74 (1983) 620.

- [31] R. Chatterjee-Fischer, R. Bodenhausen, F.-W. Eysell, R. Hoffmann, D. Liedtke, H. Mallener, W. Rembges, A. Schreiner, G. Welker: *Wärmebehandlung von Eisenwerkstoffen*, Expert-Verlag, Renningen-Malmsheim (1995).
- [32] G. Petzow: *Metallographic Etching*, ASM International, Materials Park, Ohio (1999).
- [33] T. Liapina, A. Leineweber, E.J. Mittemeijer, W. Kockelmann: *Acta Mat.* 52 (2004) 173.
- [34] T. Liapina, A. Leineweber, E.J. Mittemeijer: *Metall. Mater. Trans. A* 37A (2006) 319.
- [35] H.A. Wriedt, N.A. Gokcen, R.H. Nafziger: *Bull. Alloy Phase Diagr.* 8 (1987) 355.
- [36] A. Leineweber, T. Liapina, T. Gressmann, M. Nikolussi, E.J. Mittemeijer.: *Adv. Sci. Tec.* 46 (2006) 32.
- [37] B. Predel, M. Hoch, M. Pool: *Phase diagrams and heterogeneous equilibria*, Springer-Verlag Berlin (2004).
- [38] H.-J. Spies, S. Böhmer: *VDI – Ber. Nr. 797* (1990) 245.
- [39] T. Bell, in: L.E. Alban (Ed.): *Metals Handbook*, ASM International, Metals Park, Ohio (1981) 264.

***Extreme elastic anisotropy of cementite, Fe<sub>3</sub>C:  
First-principles calculations and experimental evidence by  
X-ray diffraction stress measurements***

*M. Nikolussi, S.L. Shang, T. Greßmann, A. Leineweber,  
E.J. Mittemeijer, Y. Wang, Z.-K. Liu*

**Abstract**

First-principles results for the full set of elastic constants (stiffnesses)  $c_{ij}$  of cementite, Fe<sub>3</sub>C, revealed an extreme elastic anisotropy with a very small  $c_{44}$  amounting to only about 1/10 of  $c_{55}$  and  $c_{66}$ . Synchrotron X-ray diffraction stress measurements were performed on Fe<sub>3</sub>C layers grown on  $\alpha$ -Fe exhibiting a planar state of compressive residual stress. These data exhibit a characteristic  $hkl$ -dependence of the stress-induced reflection shifts providing experimental proof for the extreme elastic anisotropy of Fe<sub>3</sub>C.

Cementite,  $\text{Fe}_3\text{C}$  (as a mineral also known as cohenite), has an orthorhombic crystal structure and is ferromagnetic [1-4]. It is one of the most important phases present in the majority of steels and, therefore,  $\text{Fe}_3\text{C}$  is of great industrial and – e.g. in view of the interstitial-type of incorporation of the carbon atoms - scientific interest. For instance, the extraordinary mechanical properties and the exceptionally sharp cutting edge of an ancient Damascus sabre was recently ascribed to the growth of carbon nanotubes, which initiate formation of cementite nanowires and coarse cementite particles [5]. Notwithstanding the enormously numerous applications of steels, their properties are far from fully understood mainly owing to the dearth of fundamental data of  $\text{Fe}_3\text{C}$ . Until now, the experimental elastic constants of  $\text{Fe}_3\text{C}$  are unknown, which inhibits a fundamental analysis of the elastic response of  $\text{Fe}_3\text{C}$  but in particular also of  $\text{Fe}_3\text{C}$ -containing steels to mechanical deformation. This is due to the difficulty in preparing single-phase polycrystalline  $\text{Fe}_3\text{C}$  specimens or single crystals of  $\text{Fe}_3\text{C}$  suitable for measurement of e.g. (anisotropic) mechanical properties. In particular, the full set (nine independent) of single-crystal elastic constants<sup>7.1</sup>, SECs, of orthorhombic  $\text{Fe}_3\text{C}$  has not been reported experimentally. Only partial (experimental) information is available related with SECs of  $\text{Fe}_3\text{C}$  [6-9]. None of these works suggests an extraordinarily large elastic anisotropy. Very recently the full set of nine independent elastic constants of  $\text{Fe}_3\text{C}$ , only at a pressure of 0 atm, was provided by first-principles calculations [10] during the preparation of the present manuscript; an experimental verification was not given.

The present work aims at getting more insight into the extremely anisotropic elastic properties of  $\text{Fe}_3\text{C}$ : Firstly, the SECs of  $\text{Fe}_3\text{C}$  were calculated by first-principles methods *as a function of pressure*. Secondly, the observed anisotropy was confirmed experimentally by X-ray diffraction stress measurements, using synchrotron radiation, on macrostressed, massive, polycrystalline  $\text{Fe}_3\text{C}$  layers grown on  $\alpha$ -Fe substrates.

---

<sup>7.1</sup> The SECs of  $\text{Fe}_3\text{C}$  are given in terms of the constants  $c_{ij}$  resp.  $s_{ij}$  as given using Voigt matrix notation for the stiffness or compliancy tensors. The constants are defined with respect to a Cartesian coordinate system with the basis axes parallel to [100], [010], and [001]. The latter crystallographic directions refer to a choice of axes with  $a = 5.09 \text{ \AA}$ ,  $b = 6.74 \text{ \AA}$ ,  $c = 4.52 \text{ \AA}$  [1], i.e.,  $Pnma$  space group setting.

First-principles calculations were performed by the projector-augmented wave method [11] and the generalized gradient approximation [12] as implemented in the VASP code [13] by employing a plane-wave energy cutoff of 500 eV and a reciprocal space  $k$ -point sampling of  $10 \times 7 \times 11$  in the first Brillouin zone. The elastic constants were determined applying the stress vs. strain method with strains of  $\pm 0.007$  (see details in [14]). To this end, for a given strained  $Fe_3C$  structure, the atomic arrangement (given by fractional coordinates) was relaxed; in these calculations reciprocal-space energy integration was performed using the Methfessel-Paxton technique [15]. Afterwards, for that relaxed strained  $Fe_3C$  structure, definitive stresses were calculated by reciprocal-space integration using the tetrahedron method incorporating Blöchl corrections [16]. The thus obtained stress-strain relationships were used to calculate the elastic constants of  $Fe_3C$ , essentially pertaining to a temperature of 0 K. Due to the magnetic nature of Fe, all the first-principles calculations were performed with the spin polarization approximation.

The calculated stiffnesses  $c_{ij}$  of  $Fe_3C$ , together with a couple of derived mechanical properties for a quasi-isotropic polycrystalline aggregate are presented in Table 7.1 for different unit cell volumes (the theoretically predicted equilibrium unit cell volume is  $V_0 = 151.7 \text{ \AA}^3$ ) and external pressures. For ambient pressure ( $p \approx 0 \text{ GPa}$ ) the results comply largely with those of Ref. [10]. Evidently, a relatively, extremely small value for the shear modulus  $c_{44}$ , amounting to only about 1/10 of  $c_{55}$  or  $c_{66}$  (at  $V_0$ ), occurs. This extent of anisotropy may e.g. be compared with the anisotropy ratio of cubic materials, which is basically the ratio of the maximal and minimal shear moduli,  $2c_{44}/(c_{11} - c_{12})$ . For example, for fcc-type metals an extreme anisotropy ratio of 7 is found for  $\delta$ -plutonium [17], implying that in this already extreme case anisotropy occurs that is still smaller than that predicted here for  $Fe_3C$  (a factor of 7 for  $\delta$ -plutonium compared to a factor of 10 for  $Fe_3C$  for the ratio of the extreme shear moduli of these materials). The small value of  $c_{44}$  of  $Fe_3C$  indicates a small shear resistance on (001) planes in the [010] direction, corresponding to a change of the orthorhombic lattice angle  $\alpha$  away from  $90^\circ$ . The anisotropy manifests itself also in a plot of reciprocal Young's modulus [18],  $1/E^{hkl}$ , in the (100) plane;  $1/E^{hkl}$  has its

maxima approximately along the bisectors of the  $\langle 010 \rangle$  and  $\langle 001 \rangle$  directions (approximately in  $[023]$  directions; Fig. 7.1). It must be noted that according to Born-Huang's elastic stability criterion [18-20]  $c_{44} > 0$  must hold.

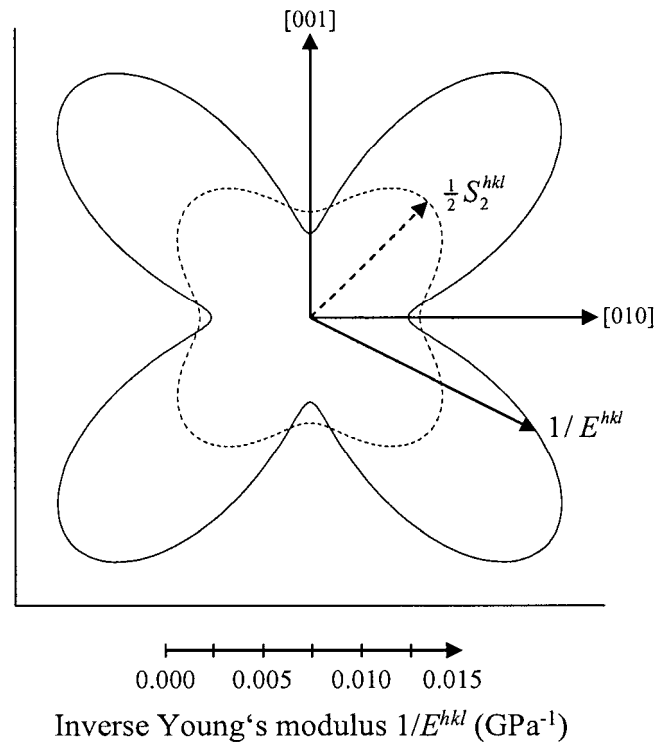


**Fig. 7.1:** Direction dependence of the inverse Young's modulus  $1/E^{hkl}$  (continuous line) and of the XEC  $\frac{1}{2}S_2^{hkl} \triangleq \left[\frac{1+\nu}{E}\right]^{hkl}$  (dashed line) in the (100) plane for  $[0kl]$  directions. The high compliances in the bisectors are the effect of the extremely small  $c_{44}$  (large  $s_{44}$ ). For a given direction,  $1/E^{hkl}$  is given by the length of an arrow (see scale at bottom) from the origin to the curve.

With increasing unit cell volume ( $V/V_0 > 1.03$ ; cf. Table 7.1),  $c_{44}$  becomes even negative, indicating an elastic instability, which could hint at a ferroelastic phase transition [21] or at melting [22], assuming that the value of  $c_{44}$  is also negative at  $T > 0$  K. In reality, such negative values for  $c_{44}$  for  $\text{Fe}_3\text{C}$  may be achieved at high temperatures (after thermal expansion) or at artificially applied negative pressures (state of tensile (hydrostatic) stress). However, no observations of this kind, hinting at an unusual effect due to a negative  $c_{44}$  of  $\text{Fe}_3\text{C}$ , have been reported in the literature.



**Table 7.1:** Single-crystal elastic stiffnesses  $c_{ij}$  (in GPa) of Fe<sub>3</sub>C (*Pnma*) and magnetic moment  $M$  (in  $\mu_B$ ) per Fe atom as obtained by first-principles calculations for different values of unit cell volume  $V$  (in  $\text{\AA}^3$ ) and external pressure  $p$  (in GPa) and at 0 K. The corresponding bulk modulus  $B$  and shear modulus  $G$  for textureless polycrystals of Fe<sub>3</sub>C according to Voigt and Reuss (in parentheses) extreme cases of grain interaction are shown in the last two columns. In the last row available experimental data pertaining to room temperature are given.

$V$	$p$	$M$	$c_{11}$	$c_{22}$	$c_{33}$	$c_{44}$	$c_{55}$	$c_{66}$	$c_{12}$	$c_{13}$	$c_{23}$	$B$	$G$
142.8	15	1.68	459	413	353	25	148	158	216	177	238	276 (272)	106 (67)
151.7 <sup>a</sup>	0	1.87	385	341	316	13	131	131	157	162	167	224 (223)	92 (43)
156.3	-6	1.93	358	299	285	-3	122	118	131	145	137	196 (195)	83 (-15)
161.0	-11	1.98	305	260	234	-13	112	104	104	108	110	160 (159)	72 (-142)
155.3 [1]	10 <sup>-4</sup>	1.87 [2]										174 [7]	74 [27]

<sup>a</sup>This row corresponds to the theoretically predicted equilibrium unit cell volume ( $=V_0$ ) at zero pressure and at 0 K. The stiffnesses  $c_{ij}$  were used for the analyses of the X-ray diffraction stress measurement data. The compliances  $s_{ij}$  can be calculated by inversion of the matrix made up by the  $c_{ij}$  values. Thus, for  $V_0$  (zero pressure, 0 K):  $s_{11} = 0.0035$ ,  $s_{22} = 0.0042$ ,  $s_{33} = 0.0047$ ,  $s_{44} = 0.077$ ,  $s_{55} = 0.0076$ ,  $s_{66} = 0.0076$ ,  $s_{12} = -0.001$ ,  $s_{13} = -0.0013$ ,  $s_{23} = -0.0017$  (all in  $\text{GPa}^{-1}$ ).

The theoretically predicted equilibrium volume ( $V_0 = 151.7 \text{\AA}^3$ ) and associated lattice parameters  $a$ ,  $b$ , and  $c$  (5.036  $\text{\AA}$ , 6.724  $\text{\AA}$ , and 4.480  $\text{\AA}$ , respectively), pertaining to 0 K, are somewhat smaller than the measured ones at room temperature (155.3  $\text{\AA}^3$ , 5.09  $\text{\AA}$ , 6.74  $\text{\AA}$ , and 4.52  $\text{\AA}$  [1]). Further, the predicted magnetic moment of 1.87  $\mu_B$  per Fe atom (Table 7.1), indicating that Fe in Fe<sub>3</sub>C is in high spin state, matches within experimental accuracy the value determined from magnetisation measurements [2]. The here predicted value for the bulk modulus (224 GPa in Voigt approximation [23]) is in good agreement with the previous first-principles results of 212 GPa [24], 229 GPa [25] and 235 GPa [26], and is somewhat larger than the experimental value obtained from the equation-of-state fitting (volume vs. pressure) applied to high

pressure X-ray powder diffraction data (174 GPa [7,9]). The experimental value for the shear modulus of textureless, polycrystalline Fe<sub>3</sub>C [27] agrees well with the calculated value (Table 7.1), considering also the large difference between the values calculated for the two extreme types (Voigt and Reuss) of elastic grain interaction [23]. Further available experimental data concern the anisotropic compressibility [7,9], as determined from lattice-parameter data at high pressures, and the Young's moduli along the [100], [010] and [001] directions [6]<sup>7.2</sup>. None of the previously obtained experimental partial data on SECs of Fe<sub>3</sub>C hint at an extreme elastic anisotropy due to a relatively very small  $c_{44}$  value as predicted by first-principles calculations in Ref. [10] and in the present work.

Experimental evidence for the predicted extremely small  $c_{44}$  was obtained by X-ray diffraction analysis of (macro)stress in polycrystalline Fe<sub>3</sub>C layers grown on  $\alpha$ -Fe substrates. The  $hkl$ -dependent stress-induced shift of peak maxima observed in such measurements provides information on the state-of-stress, but the data also contain information about the material's anisotropic elastic properties [28,29]. Although direct determination of the SECs on the basis of stress measurements is not straightforward, because (elastic) grain interaction and possible effects due to texture (in association with orientation relationships substrate-layer [30] may influence the results, the anisotropy expressed in the diffraction stress measurements is likely dominated by the character of the intrinsic (single-crystal) elastic anisotropy, in particular in the current case of extreme single-crystal elastic anisotropy [31-33]; moreover the effect of grain interaction is taken into account (see below).

In the experiments, massive Fe<sub>3</sub>C compound layers on polycrystalline  $\alpha$ -Fe substrates were produced by a recently developed gaseous carburizing process in the additional presence of ammonia (NH<sub>3</sub>) [34] (cf. *chapter 2*). The substrates were exposed in a vertical quartz-tube furnace to a gas mixture containing 13 vol. % NH<sub>3</sub>, 58 vol. % H<sub>2</sub>, 20 vol. % CO and 9 vol. % N<sub>2</sub> (as inert gas) at 823 K for 72 h, followed

---

<sup>7.2</sup> In Ref. [10] these somewhat differing Young's moduli have misleadingly been indicated as demonstrating the high elastic anisotropy of Fe<sub>3</sub>C. However, the extreme anisotropy of the SECs found here and in [10] originates from the very small value of  $c_{44}$ , which does not contribute to the Young's moduli presented in [6] and considered in [10].

by quenching the specimen in water. The massive Fe<sub>3</sub>C compound layer grown onto the  $\alpha$ -Fe surface has a thickness of about 4.6  $\mu\text{m}$  and contains distinct residual compressive stress as already encountered previously for such layers [34] (cf. *chapter 2*).

High-resolution X-ray diffraction using synchrotron radiation was performed at HASYLAB, Hamburg, Germany. Station B2 was equipped with an Eulerian cradle and operated with a wavelength of 0.79323 Å which is sufficiently small to ensure negligible absorption of radiation within the Fe<sub>3</sub>C layer. During the measurements the specimen was rotated around its surface normal to achieve better crystallite statistics.

Adopting a rotationally symmetric biaxial state of stress of the Fe<sub>3</sub>C layer parallel to the surface of the specimen (e.g. due to thermal misfit with the  $\alpha$ -Fe substrate [33], arising upon quenching the specimen from the nitrocarburising temperature to room temperature), i.e.,  $\sigma_{\parallel} \equiv \sigma_{11} = \sigma_{22}$ , strain,  $\varepsilon_{\psi}^{hkl}$ , and (macro)stress,  $\sigma_{\parallel}$ , for a Fe<sub>3</sub>C *hkl*-reflection are related by [35]:

$$\varepsilon_{\psi}^{hkl} = 2S_1^{hkl} \sigma_{\parallel} + \frac{1}{2} S_2^{hkl} \sigma_{\parallel} \sin^2 \psi, \quad (7.1)$$

with  $\psi$  denoting the tilt angle of the diffraction vector with respect to the surface normal of the specimen and  $S_1^{hkl}$  and  $\frac{1}{2} S_2^{hkl}$  as the X-ray elastic constants (XECs) which, recognizing the occurrence of grain interaction, can be taken as [35]:

$$S_{1,2}^{hkl} = w S_{1,2}^V + (1-w) S_{1,2}^{R,hkl}, \quad (7.2)$$

where  $w$  ( $0 \leq w \leq 1$ ) is a weighting factor indicating the relative contributions of the Voigt and Reuss types of grain interaction,  $S_{1,2}^V$  and  $S_{1,2}^{R,hkl}$  (note that  $S_{1,2}^V$  is *hkl* independent).

A plot of  $\varepsilon_{\psi}^{hkl}$  vs.  $\sin^2 \psi$  should yield a straight line for a given  $hkl$  (cf. Eq. (7.1); Fig. 7.2), the slope of which equals

$$\frac{1}{2}S_2^{hkl}\sigma_{\parallel} = \frac{1}{2}(wS_2^V + (1-w)S_2^{R,hkl})\sigma_{\parallel}. \quad (7.3)$$

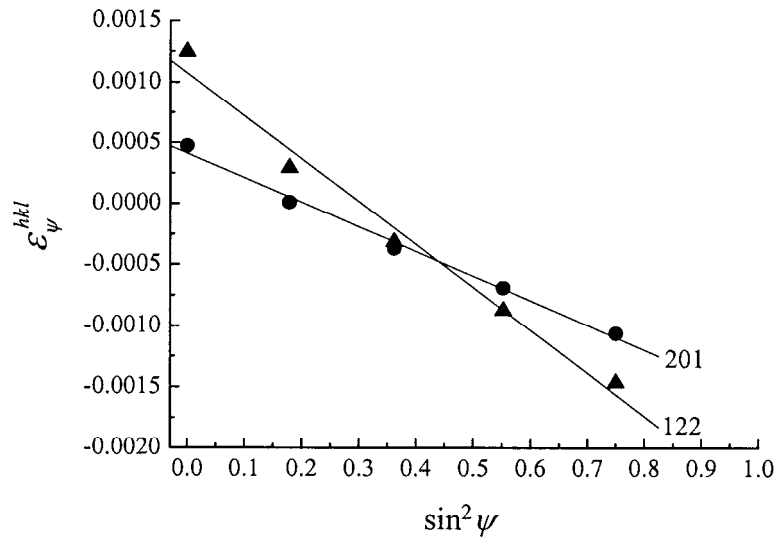


**Fig. 7.2:**  $\varepsilon_{\psi}^{hkl}$  vs.  $\sin^2 \psi$  -plot demonstrating the maximal variation in the slope,  $\frac{1}{2}S_2^{\text{obs},hkl}\sigma_{\parallel}$ , due to its  $hkl$ -dependence.

Several  $\text{Fe}_3\text{C}$   $hkl$  reflections were recorded at different tilt angles  $\psi$  of the diffraction vector with respect to the surface normal. The strain  $\varepsilon_{\psi}^{hkl}$  at tilt angle  $\psi$  with respect to the surface normal is given by:

$$\varepsilon_{\psi}^{hkl} = (d_{\psi}^{hkl} - d_0^{hkl}) / d_0^{hkl}, \quad (7.4)$$

where  $d_0^{hkl}$  is the strain-free  $d$ -spacing pertaining to the  $hkl$ -reflection of orthorhombic  $\text{Fe}_3\text{C}$  and  $d_{\psi}^{hkl}$  denotes the strained lattice spacing, as determined from the peak maximum recorded at tilt angle  $\psi$  using Bragg's law.

The extreme values of  $\frac{1}{2}S_2^{hkl}$  ( $\frac{1}{2}S_2^V$  and  $\frac{1}{2}S_2^{R,hkl}$ ; cf. Eq. (7.1)), are directly related with the single-crystal elastic constants<sup>3</sup>, as calculated according to [28]. Similar expressions as for  $\frac{1}{2}S_2^{hkl}$  also exist for  $S_1^{hkl}$  [28] (cf. Eq. (7.1)). Note that  $\frac{1}{2}S_2^V$  is *hkl*-independent, whereas  $\frac{1}{2}S_2^{R,hkl}$  depends on the direction of the diffraction vector<sup>7.3</sup>.

Data evaluation was done by determining the reflection positions by fitting of pseudo-Voigt functions. These observed reflection positions  $2\theta_{\psi}^{hkl,obs}$ , pertaining to different *hkl* and different tilt angles  $\psi$ , were compared with calculated reflection positions  $2\theta_{\psi}^{hkl,calc}$ . The calculated reflection positions were obtained by application of Bragg's law to the strained lattice spacing  $d_{\psi}^{hkl}$  as calculated on the basis of Eqs. (7.1) - (7.4),

$$d_{\psi}^{hkl} = d_0^{hkl} \sigma_{\parallel} \left[ 2(wS_1^V + (1-w)S_1^{R,hkl}) + \frac{1}{2}(wS_2^V + (1-w)S_2^{R,hkl}) \sin^2 \psi \right] + d_0^{hkl}, \quad (7.5)$$

adopting for the calculation of the XECs (cf. footnote<sup>7.3</sup>) the SECs obtained by first-principles calculations (Table 7.1) and where  $d_0^{hkl}$  was calculated from the lattice parameters *a*, *b* and *c* of orthorhombic Fe<sub>3</sub>C. The refinement was performed by minimizing  $\sum (2\theta_{\psi}^{hkl,obs} - 2\theta_{\psi}^{hkl,calc})^2$  for all *hkl* and  $\psi$  upon adopting as fit parameters the macrostress  $\sigma_{\parallel}$ , the weighting factor *w*, the lattice parameters *a*, *b*, *c* and a zero-point  $2\theta$  offset of the diffractometer.

---

7.3

$$\frac{1}{2}S_2^V = \frac{15(c_{11} + c_{22} + c_{33}) + 30(c_{12} + c_{13} + c_{23})}{2[(c_{11} + c_{22} + c_{33}) + 2(c_{12} + c_{13} + c_{23})][(c_{11} + c_{22} + c_{33}) - (c_{12} + c_{13} + c_{23}) + 3(c_{66} + c_{55} + c_{44})]}$$

$$\frac{1}{2}S_2^{R,hkl} = \frac{1}{2} \left[ \begin{aligned} &(2s_{11} - s_{12} - s_{13})x_1^4 + (-s_{12} + 2s_{22} - s_{23})x_2^4 + (-s_{13} - s_{23} + 2s_{33})x_3^4 \\ &+ (-s_{11} - s_{22} - s_{13} - s_{23} + 4s_{12} + 3s_{66})x_1^2x_2^2 + (-s_{11} - s_{33} - s_{12} - s_{23} + 4s_{13} + 3s_{55})x_1^2x_3^2 \\ &+ (-s_{22} - s_{33} - s_{12} - s_{13} + 4s_{23} + 3s_{44})x_2^2x_3^2 \end{aligned} \right]$$

where  $x_1, x_2, x_3$  are the components of a unit vector parallel to the diffraction vector in the chosen Cartesian coordinate system (cf. footnote<sup>7.1</sup>).

It was obtained  $\sigma_{\parallel} = -440$  MPa. The compressive stress parallel to the surface of the specimen can be ascribed to the cooling-induced thermal layer/substrate misfit due to the difference between the thermal expansion coefficients of  $\text{Fe}_3\text{C}$  [3] and  $\alpha\text{-Fe}$  [36]. The obtained weighting factor  $w = 0.84$  indicates an intermediate type of grain interaction more closely to the Voigt type one. The lattice parameters of  $\text{Fe}_3\text{C}$  were obtained as  $a = 5.0893$  Å,  $b = 6.7504$  Å and  $c = 4.5271$  Å, which values agree well with experimental literature data [1] and the values obtained from the first-principles calculations (cf. Table 7.1).

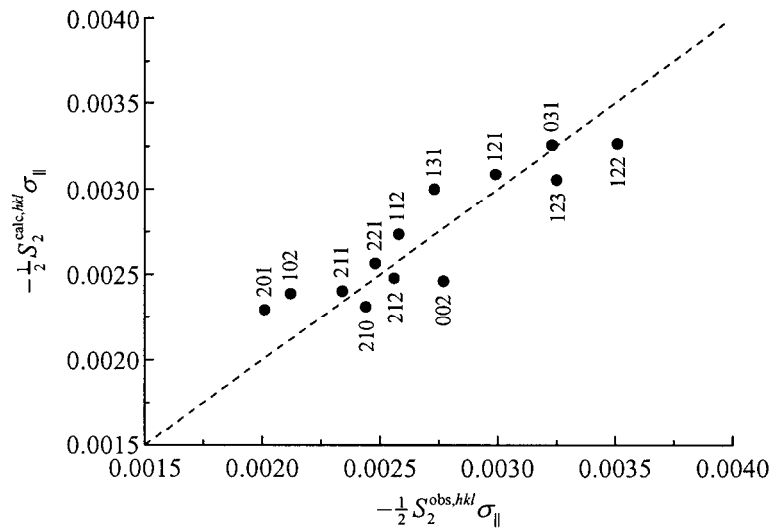


**Fig. 7.3:** Comparison of observed and calculated (cf. Eq. (7.4)) values for the  $hkl$ -dependence of the slope of the straight line in the  $\varepsilon_{\psi}^{hkl}$  vs.  $\sin^2 \psi$ -plot. The dashed line corresponds to equality of observed and calculated slopes.

Evidently, the results obtained well describe the  $hkl$ -dependence of the slope  $\frac{1}{2} S_2^{hkl} \sigma_{\parallel}$  of  $\varepsilon_{\psi}^{hkl}$  vs.  $\sin^2 \psi$ -plots (cf. Fig. 7.3). The slope  $\frac{1}{2} S_2^{hkl} \sigma_{\parallel}$  varies pronouncedly with  $hkl$ : the maximum and minimum slopes differ by a factor of 1.7 (cf. Fig. 7.2). This is an experimental confirmation of the extremely large anisotropy of  $\text{Fe}_3\text{C}$ . The largest slopes were observed for  $hkl$  with large  $k$ , and large  $l$  and small  $h$ , implying diffraction vectors close to the bisectors of the  $\langle 010 \rangle$  and  $\langle 001 \rangle$  crystallographic directions. This is an experimental confirmation of the elastic anisotropic behavior as predicted by the first-principles calculations of the SECs resulting in a very small  $c_{44}$ .

There is a clear correspondence between the  $hkl$ -dependence of  $\frac{1}{2}S_2^{hkl,calc}$  (determined from Eq. (7.3), adopting for the calculation of the XECs (cf. footnote <sup>7.3</sup>) the SECs obtained by first-principles calculations (Table 7.1)) and  $1/E^{hkl}$  in the (100) plane (cf. Fig. 7.1). Indeed, the XEC  $\frac{1}{2}S_2^{hkl}$  can be regarded as a grain-interaction weighted, average value of  $[(1+\nu)/E]^{hkl}$  [28] ( $\nu$  denotes the Poisson's ratio), of which the numerator  $1+\nu$  will definitely vary less with  $hkl$  than the denominator  $E$ . The strong  $hkl$ -dependence of  $\frac{1}{2}S_2^{hkl}$  in the (100) plane is governed by the very small  $c_{44} = 1/s_{44}$ . This is illustrated by the strong impact of a large  $s_{44}$  ( $=1/c_{44}$ ) on the  $x_2^2x_3^2$  term of  $\frac{1}{2}S_2^{R,hkl}$  (cf. footnote <sup>7.3</sup>), in which  $s_{44}$  has a large positive weight. The term  $x_2^2x_3^2$  becomes important for large  $k$  and large  $l$ , in agreement with the above regarded experimental results.

The residual scatter of the data points in Fig. 7.3 may significantly be reduced by additional refinement of some of the SECs obtained by the first-principles calculations; these minor changes in the SECs, however, do not influence the extreme elastic anisotropy of  $Fe_3C$  dominated by a very small  $c_{44}$ .

Hence, the extremely high elastic anisotropy of  $Fe_3C$ , due to a relatively very small value of  $c_{44}$ , as predicted by first-principles calculations, is confirmed by the X-ray diffraction stress measurements, on the basis of an analysis of the  $hkl$ -dependence of the stress-induced reflection shifts.

## Acknowledgement

First-principles calculations were performed on resources of the NERSC, which is supported by the Office of Science of the U.S. DOE under Contract No. DE-AC02-05CH11231. SLS, YW and ZKL at the Pennsylvania State University were partially supported by the National Science Foundation through Grants Nos. DMR-0205232 and 0510180. The authors thank Dr. D. Trots and M. Hinterstein (TU Darmstadt/HASYLAB) for their support with the synchrotron measurements.

## References

- [1] E.J. Fasiska, G.A. Jeffrey: *Acta Cryst.* 19 (1965) 463.
- [2] D. Fruchart, P. Chadouet, R. Fruchart, A. Rouault, J.P. Senateur: *J. Solid State Chem.* 51 (1984) 246.
- [3] I.G. Wood, L. Vočadlo, K.S. Knight, D.P. Dobson, W.G. Marshall, G.D. Price, J. Brodholt: *J. Appl. Crystallogr.* 37 (2004) 82.
- [4] E. Duman, M. Acet, E.F. Wassermann, J.P. Itié, F. Baudelet, O. Mathon, S. Pascarelli: *Phys. Rev. Lett.* 94 (2005).
- [5] M. Reibold, P. Paufler, A.A. Levin, W. Kochmann, N. Pätzke, D.C. Meyer: *Nature* 444 (2006) 286.
- [6] A. Kagawa, T. Okamoto, H. Matsumoto: *Acta Metall.* 35 (1987) 797.
- [7] J. Li, H.K. Mao, Y. Fei, E. Gregoryanz, M. Erements, C.S. Zha: *Phys. Chem. Minerals* 29 (2002) 166.
- [8] M. Umemoto, Y. Todaka, T. Takahashi, P. Li, R. Tokumiya, K. Tsuchiya: *J. Metastab. Nanocryst. Mater.* 15-16 (2003) 607.
- [9] E. Duman, M. Acet, T. Hülser, E.F. Wassermann, B. Rellinghaus, J.P. Itié, P. Munsch: *J. Appl. Phys.* 96 (2004) 5668.
- [10] C. Jiang, S.G. Srinivasan, A. Caro, S.A. Maloy: *J. Appl. Phys.* 103 (2008) 043502.
- [11] G. Kresse, D. Joubert: *Phys. Rev. B* 59 (1999) 1758.
- [12] J.P. Perdew, K. Burke, M. Ernzerhof: *Phys. Rev. Lett.* 77 (1996) 3865.
- [13] G. Kresse, J. Furthmuller: *Comput. Mater. Sci.* 6 (1996) 15.
- [14] S.L. Shang, Y. Wang, Z.K. Liu: *Appl. Phys. Lett.* 90 (2007) 101909.
- [15] M. Methfessel, A.T. Paxton: *Phys. Rev. B* 40 (1989) 3616.
- [16] P.E. Blöchl, O. Jepsen, O.K. Andersen: *Phys. Rev. B* 49 (1994) 16223.
- [17] H.M. Ledbetter, R.L. Moment: *Acta Metall.* 24 (1976) 891.
- [18] J. F. Nye: *Physical properties of crystals: their representation by tensors and matrices*, Oxford University Press (1985).
- [19] R.A. Cowley: *Phys. Rev. B* 13 (1976) 4877.
- [20] M. Born, K. Huang: *Dynamical theory of crystal lattices*, Oxford University Press (1988).



- [21] P. Toledano, M.M. Fejer, B.A. Auld: *Phys. Rev B* 27 (1983) 5717.
- [22] R.W. Cahn: *Nature* 413 (2001) 582.
- [23] G. Simmons, H. Wang: *Single crystal elastic constants and calculated aggregate properties*, MIT Press (1971).
- [24] L. Huang, N.V. Skorodumova, A.B. Belonoshko, B. Johansson, R. Ahuja: *Geophys. Res. Lett.* 32 (2005) L21314.
- [25] L. Vocadlo, J. Brodholt, D.P. Dobson, K.S. Knight, W.G. Marshall, G.D. Price, I.G. Wood: *Earth Planet. Sci. Lett.* 203 (2002) 567.
- [26] H.I. Faraoun, Y.D. Zhang, C. Esling, H. Aourag: *J. Appl. Phys.* 99 (2006).
- [27] F. Laszlo, H. Nolle: *J. Mech. Phys. Solids* 7 (1959) 193.
- [28] C.J. Howard, E.H. Kisi: *J. Appl. Crystallogr.* 32 (1999) 624.
- [29] S. Matthies, H.G. Priesmeyer, M.R. Daymond: *J. Appl. Cryst.* 34 (2001) 585.
- [30] H.K.D.H. Bhadeshia: *Worked examples in the Geometry of Crystals*, 2<sup>nd</sup> edition, The Institute of Metals, London (2006).
- [31] U. Welzel, E.J. Mittemeijer: *J. Appl. Phys.* 93 (2003) 9001.
- [32] D.B. Hovis, A. Reddy, A.H. Heuer: *Appl. Phys. Lett.* 88 (2006) 131910.
- [33] T. Gressmann, M. Wohlschlägel, S. Shang, U. Welzel, A. Leineweber, E.J. Mittemeijer, Z.-K. Liu: *Acta Mat.* 55 (2007) 5833.
- [34] T. Gressmann, M. Nikolussi, A. Leineweber, E.J. Mittemeijer: *Scr. Mat.* 55 (2006) 723.
- [35] U. Welzel, J. Ligot, P. Lamparter, A.C. Vermeulen, E.J. Mittemeijer: *J. Appl. Crystallogr.* 38 (2005) 1.
- [36] Y.S. Touloukian, R.K. Kirby, R.E. Taylor, P.D. Desai: *Thermal expansion: metallic elements and alloys*, IFI/Plenum (1977).



## *Summary*

### **8.1 Introduction**

Gaseous nitriding, gaseous carburising and gaseous nitrocarburising are thermochemical heat treatments, which are of pronounced technical importance since the beginning of the twentieth century. The substrate (iron-based materials, mostly steels) reacts with the gas atmosphere, and, due to the chemical reactions that take place, a concerted change of the chemical composition of the iron-based workpieces results. This can lead to the formation of a diffusion zone with a thickness of several hundreds of micrometers, within which nitrogen and/or carbon (provided by the gas atmosphere) are either dissolved in the octahedral sites of the iron *bcc*-lattice or are bound to alloying elements. This diffusion zone is responsible for a considerable enhancement of the fatigue endurance of the iron-based workpiece. Furthermore, the concerted change of the chemical composition of the iron-based workpiece can lead to the generation of hard, wear- and corrosion-resistant surface compound layers, which can extend several tens of micrometers.

Gaseous nitriding and gaseous nitrocarburising are usually performed at temperatures in the range of 773 K – 843 K. The process temperature is located below the binary/ternary eutectoid temperatures of the Fe–N/Fe–N–C solid solutions i.e. in the ferritic regime. Whereas the nitriding and/or the nitrocarburising gas atmosphere provide nitrogen and/or carbon, the carburising gas atmosphere only provides carbon. These are incorporated into the surface region of an iron-based workpiece by diffusion processes. Gaseous carburising is usually performed at much higher treatment temperatures in the range of 1173 – 1273 K. Therefore, the process temperature is located in the austenitic regime, which results in - in contrast to gaseous

nitriding/nitrocarburising - considerable changes of the dimensions of the iron-based workpiece.

Within the diffusion zone, which developed after the thermochemical heat treatment (in the course of the present work gaseous nitriding/nitrocarburising),  $\alpha''$ -Fe<sub>16</sub>N<sub>2</sub> or  $\gamma'$ -Fe<sub>4</sub>N<sub>1-y</sub> precipitates can be formed. The compound layer (located on top of the diffusion zone), which may develop after the thermochemical heat treatment under certain circumstances (high activities of nitrogen and/or carbon) can, depending on the process parameters (treatment temperature, treatment pressure, treatment time, composition of the gas atmosphere) consist of different phases. The compound layer is usually composed of  $\gamma'$ -Fe<sub>4</sub>N<sub>1-y</sub> and/or  $\epsilon$ -Fe<sub>3</sub>(N,C)<sub>1+x</sub> but, also cementite can form within the compound layer coexisting with  $\gamma'$ -Fe<sub>4</sub>N<sub>1-y</sub> and  $\epsilon$ -Fe<sub>3</sub>(N,C)<sub>1+x</sub>.

The formation of massive cementite compound layers on ferrite substrates is not trivial. Cementite formation upon gaseous carburising is usually accompanied by severe sooting and cementite disintegration, so-called metal dusting. It was reported in the literature that due to the addition of H<sub>2</sub>S to the carburising gas atmosphere, sooting and metal dusting can be suppressed. There were even hints in the literature that the addition of ammonia to the carburising gas atmosphere may delay or even suppress sooting and metal dusting.

Although thermochemical heat treatments such as gaseous nitrocarburising are widely applied in industrial processes, many open questions remain. The present work aims on the one hand at the generation of massive cementite compound layers on ferrite substrates. On the other hand, the present work shall answer some open questions concerning cementite in the Fe–N–C system.

## 8.2 Experimental Procedure

By cold-rolling an  $\alpha$ -iron cast rod (99.98 gew.-% Fe) on both sides, an iron foil of 1 mm thickness was produced. The rectangular specimens (20 mm × 25 mm) to be thermochemically heat treated were cut from this iron foil, afterwards ground and polished. Prior to the thermochemical heat treatment, the specimens were recrystallised for 2 h at 973 K under a reductive hydrogen atmosphere.

For the thermochemical heat treatments the specimens were positioned by a sample stage at which a quartz fibre was fixed in the middle of a vertical quartz-tube furnace within which the process temperature was controlled by  $\pm 1$  K. At the top of the quartz-tube furnace, ammonia, hydrogen, carbon monoxide and nitrogen – controlled by separate mass-flow controllers - were inserted into the furnace. At the bottom, the quartz-tube furnace was equipped with a water container (flushed with N<sub>2</sub>) for quenching the specimens (retain microstructural states which were produced at the treatment temperature) to room temperature.

The thermochemically treated specimens were analysed by different techniques. The examination of the microstructure was performed by light-optical microscopy. Phase analysis was performed by both electron backscatter diffraction and X-ray diffraction (CoK<sub>α</sub> radiation). For the determination of residual stresses of the specimens, synchrotron radiation was used. The diffractometer was equipped with an Eulerian cradle and operated in parallel-beam geometry.

## 8.3 Results and Discussion

### 8.3.1 Formation of massive cementite compound layers and its growth kinetics

To date, fundamental knowledge on cementite and the growth kinetics of cementite layers lacks. This is basically due to the fact that the formation of massive cementite compound layers with strongly carburising gas atmosphere (high carbon activities), is usually accompanied by simultaneous sooting and cementite disintegration (metal dusting).

In *chapters 2 and 3* of the present work it was demonstrated for the first time that the concerted addition of ammonia to a strongly carburising gas atmosphere can suppress both sooting and cementite disintegration (metal dusting). However, cementite formation succeeded only in a small parameter range (cf. Fig. 8.1a). An increased ammonia content in the gas atmosphere led to the formation of iron(carbo)-nitrides, whereas a decreased ammonia content in the gas atmosphere led to simultaneous sooting and cementite disintegration (metal dusting). Moreover, it was

shown in *chapter 2* that the cementite-layer thickness increased with increasing ammonia content.

In *chapter 2* and *3* of the present work the growth kinetics of cementite layers was investigated. Cementite-layer growth can for the whole parameter range within which cementite-layer formation succeeded be described by a modified parabolic growth law (cf. Fig. 8.1b)

$$S_{\text{Fe}_3\text{C}}^2(t, T) = k(T)t + S_0^2(T), \quad (8.1)$$

where  $S_{\text{Fe}_3\text{C}}$  [m] is the time-dependent cementite-layer thickness,  $k$  the temperature-dependent parabolic growth constant and  $S_0$  a temperature-dependent, hypothetical initial cementite-layer thickness at  $t = 0$ . This  $S_0$  describes a shift of the cementite-layer thickness data, dissenting from simple parabolic growth, due to a faster cementite-layer growth in the initial stage.

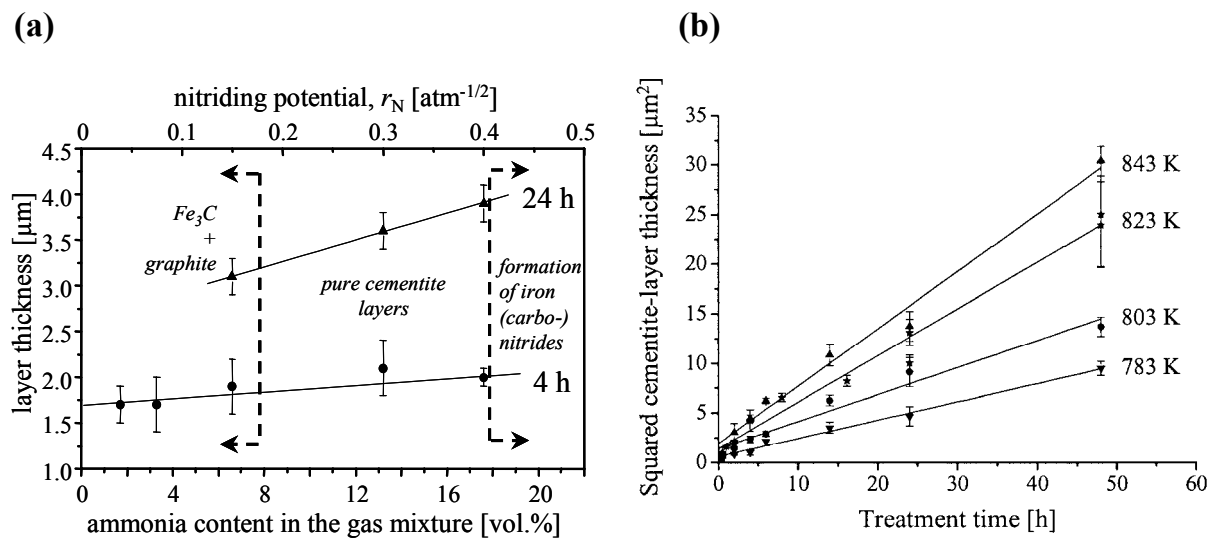


**Abb. 8.1:** (a) Increase of the cementite-layer thickness as a function of the ammonia content in the gas atmosphere. In a specific parameter range pure, massive cementite layers can be formed on ferrite substrates at 823 K. For increased ammonia contents iron(carbo-)nitrides were formed additionally. For decreased ammonia contents simultaneous sooting and cementite disintegration took place. (b) Time-dependent evolution of the squared cementite-layer thickness at 783 K, 803 K, 823 K and 843 K. Cementite-layer growth can be described by a modified parabolic growth law (continuous lines).

The effective diffusion coefficient of carbon decreases as a function of time; cementite-layer growth was explained on the basis of a two-stage mechanism. In the early stage ( $t \leq 5$  min) only a few cementite crystallites have formed on the ferrite substrate. Since carbon diffusion in cementite is much slower than in ferrite, carbon transport proceeds mainly through the ferrite, bypassing cementite. After coalescence of the cementite crystallites a closed cementite layer resulted. However, this closed cementite layer is relatively thin and defect-rich (high grain-boundary density). This leads initially ( $5 \text{ min} < t < 1 \text{ h}$ ) to an increased effective diffusion coefficient of carbon through cementite. After defects have annihilated in the later stage of cementite-layer growth ( $t < 1 \text{ h}$ ), a decreasing diffusion coefficient of carbon through cementite resulted. For treatment times  $t \geq 1 \text{ h}$  parabolic cementite-layer growth was found, indicating a constant effective diffusion coefficient of carbon in cementite during this stage.

In *chapter 3* of the present work an “apparent” activation energy for cementite-layer growth was determined according to the Arrhenius-type temperature dependence of the parabolic growth constant. It was shown that this “apparent” activation energy is composed of two contributions: (i) a positive contribution due to the activation energy of (tracer-)diffusion of carbon in cementite and (ii) a negative contribution due to an energy which is evoked by the temperature dependence of the carbon activity difference between the surface of the specimen and the interface cementite/ferrite. This negative energy is caused by an “effective” carbon activity at the surface of the specimen (the activity of carbon at the interface cementite/ferrite remains virtually constant), which can be estimated using literature data and which decreases considerably with increasing treatment temperature.

### **8.3.2 Orientation relationships of cementite and ferrite and the consequences**

To date, the orientation relationship between cementite and ferrite has been investigated in many works, several types of orientation relationships were observed. These investigations have mainly been performed in perlite and other microstructures

resulting from the austenite/ferrite transition. The orientation relationship between cementite grains of a compound layer and ferrite grains of the underlying substrate has not been investigated, yet.

In *chapter 4* of the present work a detailed study of the orientation relationship between cementite grains of the compound layer and ferrite grains of the substrate was performed on the basis of measurements by means of electron backscatter diffraction (EBSD). It was shown for the first time that the Bagaryatsky orientation relationship holds for this system. Based on this orientation relationship twelve orientation variants can be deduced. These twelve orientation variants can - depending on the orientation of the underlying ferrite substrate – be grouped into classes of orientation variants, which differ with respect to the surface normal of the specimen. Preference of specific classes of orientation variants was indicated by the experimental data. This was ascribed to low misfit-strain energy for favoured orientation variants as compared to high misfit-strain energy for unfavoured orientation variants.

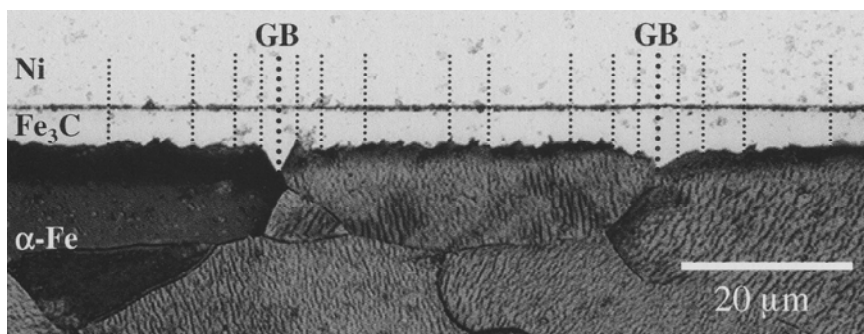


**Abb. 8.2:** Light-optical microscopic image of a cementite layer on a ferrite substrate. The cementite-layer thickness is highest at the location of ferrite grain boundaries (GB).

Furthermore, on the basis of the Bagaryatsky orientation relationship, also the orientation relationship between neighbored cementite grains was investigated. It was shown that neighbored cementite grains, which were grown on the same underlying ferrite grain, exhibited high-energy cementite grain boundaries. In contrast, neighbored cementite grains, which were grown on two adjacent underlying ferrite grains, exhibited low-energy cementite grain boundaries.



The development of high-energy cementite grain boundaries promoted carbon transport via cementite grain-boundary diffusion.

This was experimentally evidenced by larger cementite-layer thicknesses at the location of ferrite-grain boundaries intersecting the substrate surface (cf. Fig. 8.2).

### 8.3.3 Diffusivity of nitrogen and activation energy of nitrogen diffusion in cementite

Since there are no works published in the literature which report either on the diffusivity of nitrogen or on the activation energy of nitrogen diffusion in cementite, these were determined in *chapter 5* of the present work on the basis of hardness-depth profiles (cf. Fig. 8.3). A growing cementite layer of time-dependent thickness was grown on a ferrite substrate. Nitrogen diffusion through the cementite layer took place, i.e. the underlying ferrite substrate got enriched with interstitially dissolved nitrogen. Due to the embedding process (necessary for metallographic investigation), which can be considered as heat treatment,  $\alpha''$ -Fe<sub>16</sub>N<sub>2</sub> precipitated had formed in the ferrite substrate, which led to a considerable increase of its hardness. The order of the hardness increase is a measure for the amount of nitrogen dissolved in the ferrite. On the basis of additional measurements by chemical analysis a calibration line was constructed with which such hardness-depth profiles were transformed into nitrogen concentration-depth profiles (cf. Fig. 8.3).

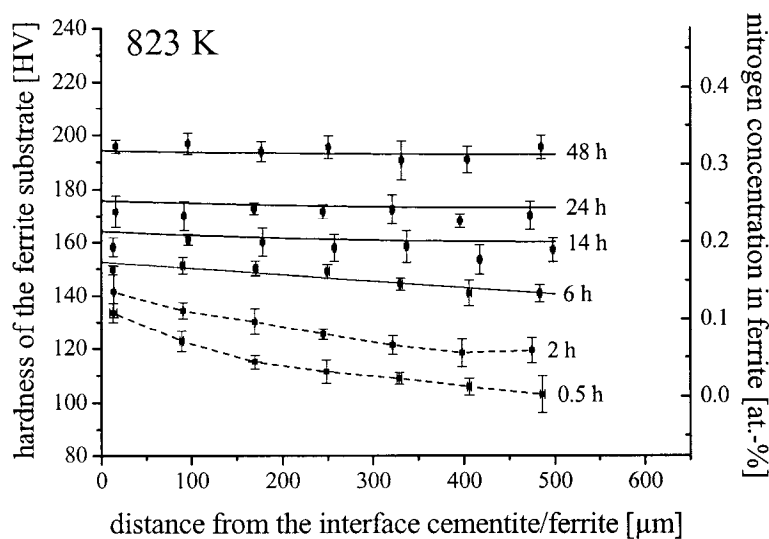


**Fig. 8.3:** Hardness-depth profiles in the ferrite substrate after nitrocarburising treatments at 823 K for different treatment times under the formation of cementite layers at the surface of the specimen. By the help of a calibration line, these profiles were transformed into nitrogen concentration-depth profiles.

Such nitrogen concentration-depth profiles were simulated on the basis of a developed model using the implicit-finite difference method. These simulated profiles were accommodated to the experimentally determined nitrogen concentration-depth profiles by minimising the sum of the squared differences between simulated and experimental values. The simulation yielded, for the first time, values for both the diffusivity of nitrogen through cementite and the activation energy of nitrogen diffusion in cementite. The activation energy, which was determined for nitrogen diffusion in cementite, is relatively low and is in the order of the activation energy for nitrogen/carbon diffusion in ferrite. This was explained on the basis of nitrogen grain-boundary diffusion through cementite.

### 8.3.4 New information on the Fe–N–C system

To date, the existence of the two-phase region  $\alpha\text{-Fe} + \varepsilon\text{-Fe}_3(\text{N,C})_{1+x}$  itself and the temperature range at which it occurs are discussed controversially in the literature. The existence of this two-phase region is directly related with the invariant transition reaction  $\gamma'\text{-Fe}_4\text{N} + \text{Fe}_3\text{C} \rightarrow \alpha\text{-Fe}[\text{N,C}] + \varepsilon\text{-Fe}_3(\text{N,C})_{1+x}$ , which is passed at one *single* temperature.

In *chapter 6* of the present work the existence of the two-phase region  $\alpha\text{-Fe} + \varepsilon\text{-Fe}_3(\text{N,C})_{1+x}$  was proven experimentally for the first time. Moreover, on the basis of nitrocarburising experiments and systematic secondary annealing (after nitrocarburising), the invariant transition reaction  $\gamma'\text{-Fe}_4\text{N} + \text{Fe}_3\text{C} \rightarrow \alpha\text{-Fe}[\text{N,C}] + \varepsilon\text{-Fe}_3(\text{N,C})_{1+x}$  could be shown to proceed at a temperature between 833 K and 843 K. It was shown that electron backscatter diffraction (EBSD) is a powerful tool for performing systematic phase identification within the microstructure (compound layer). The obtained results provided new insight into the constitution of the ternary phase diagram Fe–N–C and might also be of technical relevance.

### 8.3.5 Elastic constants of cementite

Although cementite-containing steels are common in technical and industrial applications, fundamental knowledge on the mechanical properties of cementite lacks. This is mainly due to difficulties in preparing single-phase polycrystalline cementite specimens. Thus, the experimental (single-crystal) elastic constants of cementite are yet unknown. Hence, it is not possible to analyse and/or model the elastic response of e.g. cementite containing steels to mechanical deformation. Very recently, *first-principles* calculations have been reported in the literature which yielded the full set of nine independent elastic constants of orthorhombic cementite.

In *chapter 7* of the present work the nine independent elastic constant of orthorhombic cementite were calculated for the first time as a function of pressure. The results of these calculations indicated extreme elastic anisotropy of cementite manifested by an extremely small value of  $c_{44}$  as compared to  $c_{55}$  and  $c_{66}$ . This extreme elastic anisotropy was proven experimentally in *chapter 7* of the present work. Residual-stress measurements were performed on cementite layers grown on ferrite substrates using synchrotron radiation. These cementite layers exhibited compressive residual stresses. The  $hkl$ -dependent stress-induced reflection shifts can be regarded as experimental evidence for the extreme elastic anisotropy of cementite.



## *Zusammenfassung in deutscher Sprache*

### **9.1 Einleitung**

Gasnitrieren, Gascarburieren und Gasnitrocarburieren sind thermochemische Wärmebehandlungsverfahren von Eisenbasismaterialien, meist Stählen, die seit dem 20. Jahrhundert von großer technologischer Bedeutung sind. Hierbei wird durch eine chemische Reaktion des Substratmaterials mit einer reaktiven Gasatmosphäre, die Stickstoff und/oder Kohlenstoff bereitstellt, eine gezielte Veränderung der chemischen Zusammensetzung des Eisenbasismaterials erzielt. Dieses kann zur Erzeugung einer sogenannten Diffusionszone führen, in der primär Stickstoff und/oder Kohlenstoff in den Oktaederlücken des kubisch-raumzentrierten Eisens eingelagert werden können. Die Diffusionszone, die mehrere hundert Mikrometer dick sein kann, ist für eine erhebliche Verbesserung der Ermüdungsbeständigkeit des Eisenbasismaterials verantwortlich. Darüber hinaus kann unter bestimmten Reaktionsbedingungen (hohe Stickstoff- und/oder Kohlenstoffaktivität in der Gasatmosphäre) die gezielte Veränderung der chemischen Zusammensetzung des Eisenbasismaterials zur Erzeugung einer harten, verschleißfesten und korrosionsbeständigen Verbindungsschicht an der Probenoberfläche führen, die mehrere zehn Mikrometer dick sein kann.

Die Prozesse des Gasnitrierens und des Gasnitrocarburierens werden für gewöhnlich im Temperaturbereich zwischen 773 K und 843 K durchgeführt, d.h. man befindet sich dabei unterhalb der binären/ternären eutektoiden Temperatur (ferritisch) des Fe–N/Fe–N–C-Mischkristalls. Im Verlauf der Behandlungsreaktion werden Stickstoff und/oder Kohlenstoff mittels Diffusionsprozessen im Oberflächenbereich des Eisenbasismaterials eingelagert. Dem gegenüber steht der Prozess des Gascarburierens bei dem bei einer Behandlungstemperatur von 1173 K – 1273 K, also

bei einer wesentlich höheren Behandlungstemperatur, Kohlenstoff im Oberflächenbereich des Eisenbasismaterials eingelagert wird. Durch diese höheren Behandlungstemperaturen - man befindet sich im Austenitgebiet - kommt es im Gegensatz zum Gasnitrieren und Gasnitrocarburieren zu einem erheblichen Verzug der zu behandelnden Probe.

Innerhalb der Diffusionszone, die sich nach Beendigung der thermochemischen Wärmebehandlung (im Rahmen dieser Arbeit handelt es sich dabei um Gasnitrieren und Gasnitrocarburieren) ausgebildet hat, können  $\alpha''$ - $\text{Fe}_{16}\text{N}_2$ - oder  $\gamma'$ - $\text{Fe}_4\text{N}_{1-y}$ -Ausscheidungen entstehen. Die ausgebildete Verbindungsschicht kann in Abhängigkeit der Prozessparameter (Behandlungstemperatur, Behandlungsdruck, Behandlungsdauer, Zusammensetzung der reaktiven Gasatmosphäre) aus unterschiedlichen Phasen bestehen. Gewöhnlich besteht die erzeugte Verbindungsschicht aus  $\gamma'$ - $\text{Fe}_4\text{N}_{1-y}$  und/oder  $\epsilon$ - $\text{Fe}_3(\text{N,C})_{1+x}$ , aber auch Zementit kann neben diesen beiden erwähnten Phasen in der Verbindungsschicht koexistieren.

Die Erzeugung von reinen, massiven Zementitschichten mittels Gascarburierens hingegen wird immer von starker Verrußung und der Zementitzersetzung begleitet, welche als „metal dusting“ bezeichnet wird. Auf Grund dessen kann die Erzeugung von reinen, massiven Zementitschichten als nicht gerade trivial bezeichnet werden. In der Literatur wurde berichtet, dass die Verrußung und die Zementitzersetzung („metal dusting“) durch die Zugabe von  $\text{H}_2\text{S}$  zur aufkohlenden Gasatmosphäre unterdrückt werden können. Darüber hinaus gibt es in der Literatur Hinweise darauf, dass auch die Zugabe von Ammoniak zur aufkohlenden Gasatmosphäre die Verrußung und die Zementitzersetzung verlangsamen oder gar unterdrücken können.

Trotz der Tatsache, dass Gasnitrocarburieren in industriellen Prozessen weit verbreitet ist, gibt es viele unbeantwortete Fragen. Das Ziel dieser Arbeit soll einerseits die Erzeugung von reinen, massiven Zementitschichten auf ferritischen Reineisensubstraten sein. Andererseits sollen bisher unbeantwortete Fragen beantwortet werden, die im Zusammenhang mit Zementit als einer Phase des Fe-N-C Systems stehen.

## 9.2 Experimentelle Vorgehensweise

Aus einem Reineisenabguss (99,98 gew.-% Fe) wurde durch beidseitiges Kaltwalzen eine Eisenfolie der Dicke von 1 mm hergestellt. Daraus wurden die zu behandelnden rechteckigen Proben (20 mm × 25 mm) herausgeschnitten, anschließend geschliffen, poliert und gereinigt. Vor der thermochemischen Wärmebehandlung wurden die Proben für 2 h bei 973 K unter einer reduzierenden Wasserstoffatmosphäre rekristallisiert.

Für die thermochemische Wärmebehandlung wurden die Proben mit Hilfe einer Probenstange und eines daran befestigten Quarzfadens in die Mitte eines vertikal angeordneten Mehrzonenofens eingebracht, in dem die Behandlungstemperatur (geregelt innerhalb  $\pm 1$  K) vorlag. Am oberen Ende des Mehrzonenofens befindet sich der Gaseinlass, an dem Ammoniak, Wasserstoff, Kohlenstoffdioxid und Stickstoff, gesteuert durch Massedurchflussregler, in den Mehrzonenofens eingeleitet werden können. Am unteren Ende des Mehrzonenofens befindet sich eine Abschreckeinheit, die aus einer Wasserflasche besteht, die mit Stickstoff gespült wird. Nach Ablauf der gewünschten Behandlungsdauer kann der Quarzfaden mechanisch abgetrennt werden und die Probe fällt direkt in die Abschreckeinheit. Dadurch kann die Mikrostruktur, die bei der Behandlungstemperatur vorlag, bei Raumtemperatur stabilisiert werden.

Die behandelten Proben wurden mit unterschiedlichen Methoden charakterisiert. Die Untersuchung der Mikrostruktur erfolgte mittels Lichtmikroskopie an Querschliffen. Zur Phasenanalyse wurden die Elektronenrückstreubeugung sowie die Röntgenpulverdiffraktometrie ( $\text{CoK}_\alpha$ -Strahlung) herangezogen. Zur röntgenographischen Spannungsmessung wurde Synchrotronstrahlung verwendet. Das entsprechende Diffraktometer war mit einer Eulerwiege ausgestattet und arbeitete in Parallelstrahlgeometrie.

## 9.3 Ergebnisse und Diskussion

### 9.3.1 Erzeugung von reinen, massiven Zementitschichten und deren Wachstumskinetik

Bis heute ist über Zementit und die Wachstumskinetik von Zementitschichten wenig bekannt. Das liegt hauptsächlich daran, dass die Erzeugung von reinen, massiven Zementitschichten mittels stark aufkohlender Gasatmosphären immer von Verrußung und Zementitzersetzung („metal dusting“) begleitet wird.

In den *Kapiteln 2* und *3* dieser Arbeit konnte zum ersten Mal gezeigt werden, dass die gezielte Zugabe von Ammoniak zu einer stark aufkohlenden Gasatmosphäre sowohl die Verrußung als auch die Zementitzersetzung („metal dusting“) unterdrücken kann. Jedoch ist dies lediglich in einem schmalen Parameterbereich möglich (Abb. 9.1a). Wird ein zu hoher Ammoniakgehalt zur Gasatmosphäre dazugegeben, so erfolgt eine zusätzliche Bildung von Eisen(carbo)nitriden in der Verbindungsschicht. Wird ein zu geringer Ammoniakgehalt zur Gasatmosphäre dazugegeben, so tritt hingegen Verrußung und Zementitzersetzung („metal dusting“) ein. Darüber hinaus konnte in *Kapitel 2* gezeigt werden, dass die Zementitschichtdicke tendenziell mit zunehmendem Ammoniakgehalt zunimmt.

In den *Kapiteln 2* und *3* dieser Arbeit wurde die Schichtwachstumskinetik des Zementits untersucht. Die Schichtwachstumskinetik des Zementits kann für den gesamten Behandlungstemperaturbereich in dem Zementit erzeugt werden kann, durch ein modifiziertes Wachstumsgesetz beschrieben werden (Abb. 9.1b):

$$S_{\text{Fe}_3\text{C}}^2(t, T) = k(T)t + S_0^2(T), \quad (9.1)$$

wobei  $S_{\text{Fe}_3\text{C}}$  [m] die zeitabhängige Zementitschichtdicke,  $k$  die temperaturabhängige parabolische Wachstumskonstante und  $S_0$  eine temperaturabhängige, hypothetische, anfängliche Zementitschichtdicke bei der Zeit  $t = 0$  ist.



Dieses  $S_0$  beschreibt einen Versatz in den Schichtdickendaten, der durch eine Abweichung von rein parabolischem Wachstum aufgrund eines anfänglich schnelleren Zementitschichtwachstums verursacht wird.

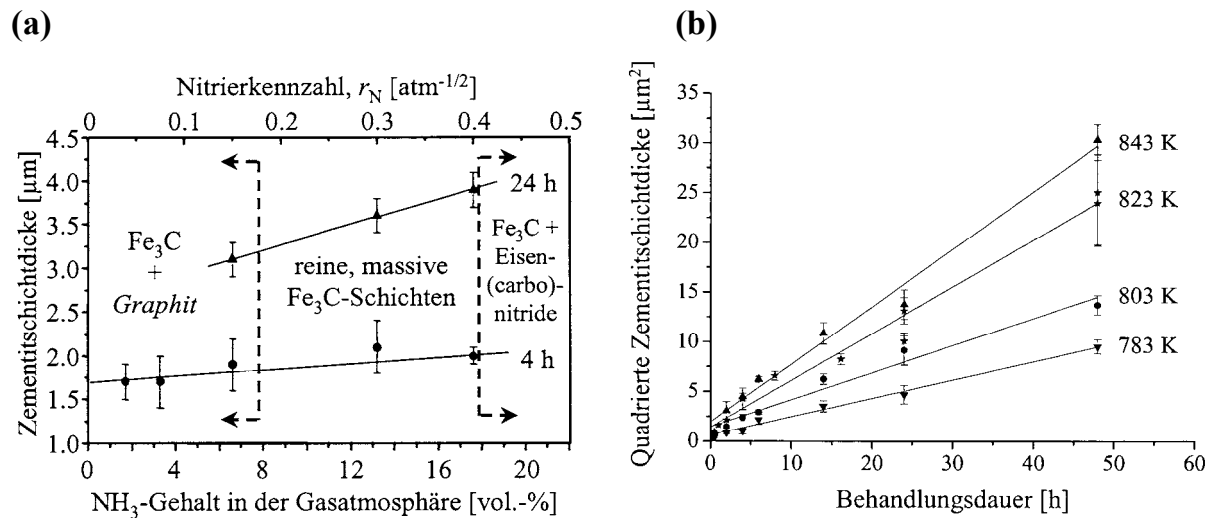


**Abb. 9.1:** (a) Zunahme der Zementitschichtdicke als Funktion des Ammoniakgehalts. Bei 823 K können in einem bestimmten Parameterbereich reine, massive Zementitschichten entstehen. Bei höherem Ammoniakgehalt entsteht zusätzlich Eisen(carbo)nitrid in der Verbindungsschicht. Bei zu niedrigem Ammoniakgehalt kommt es zu Verrußung und Zementitzersetzung. (b) Zeitliche Entwicklung der quadrierten Zementitschichtdicke bei 783 K, 803 K, 823 K und 843 K. Das Zementitschichtwachstum kann durch ein modifiziertes parabolisches Wachstumsgesetz beschrieben werden (durchgezogene Linien).

Der effektive Diffusionskoeffizient von Kohlenstoff sinkt als Funktion der Zeit und das Zementitschichtwachstum kann mit einem zweistufig ablaufenden Mechanismus erklärt werden. Im Anfangsstadium ( $t \leq 5$  min) haben sich nur vereinzelt Zementitkristalle auf dem ferritischen Substrat gebildet. Zementit kann als Diffusionsbarriere für Kohlenstoff angesehen werden. Deshalb erfolgt der Kohlenstofftransport nicht über Zementit, sondern über Ferrit. Kohlenstoff diffundiert demnach um die einzelnen Zementitkristalle herum. Nachdem die einzelnen Zementitkristalle zusammengewachsen sind, ist die Zementitschicht zwar geschlossen, jedoch zunächst relativ dünn und defektreich (hohe Korngrenzendichte). Dies führt anfänglich ( $5 \text{ min} < t < 1 \text{ h}$ ) zu einem erhöhten effektiven Diffusionskoeffizienten von

Kohlenstoff durch Zementit. Nachdem im späteren Stadium des Zementitschichtwachstums ( $t < 1$  h) die Defekte ausgeheilt sind, sinkt der effektive Diffusionskoeffizient von Kohlenstoff durch Zementit. Ab einer Behandlungszeit von  $t \geq 1$  h kann für Zementit parabolisches Wachstum angenommen werden.

In *Kapitel 3* dieser Arbeit wurde anhand der Arrhenius-artigen Temperaturabhängigkeit der parabolischen Wachstumskonstante eine „effektive“ Aktivierungsenergie bestimmt. Es konnte gezeigt werden, dass diese „effektive“ Aktivierungsenergie aus zwei Bestandteilen besteht: Zum einen aus der (positiven) Aktivierungsenergie für Kohlenstoff(tracer)diffusion in Zementit und zum anderen aus einer (negativen) Energie, die sich auf die Temperaturabhängigkeit der Kohlenstoffaktivitätsdifferenz zwischen der Oberfläche der Probe und der Grenzfläche Zementit/Ferrit zurückführen lässt. Diese negative Energie hat zu Folge, dass die „effektive“ Kohlenstoffaktivität an der Oberfläche der Probe (die Kohlenstoffaktivität an der Grenzfläche Zementit/Ferrit bleibt nahezu konstant), die anhand von Literaturdaten berechnet werden kann, mit steigender Temperatur erheblich abnimmt.

### **9.3.2 Orientierungsbeziehung zwischen Zementit und Ferrit und die daraus resultierenden Konsequenzen**

Bis heute wurde in der Literatur die Orientierungsbeziehung zwischen Zementit und Ferrit in vielen Arbeiten untersucht, mehrere Arten von Orientierungsbeziehungen wurden beobachtet. Diese Untersuchungen erfolgten zumeist in Perlit, die Orientierungsbeziehung zwischen Zementitkörnern von Verbindungsschichten und Ferritkörnern des Substrats wurde bis dato noch nicht untersucht.

In *Kapitel 4* dieser Arbeit wurde eine ausführliche Studie der Orientierungsbeziehung zwischen Zementitkörnern der Verbindungsschicht und Ferritkörnern des Substrats mit Hilfe der Elektronenrückstreubeugung durchgeführt. Es konnte zum ersten Mal gezeigt werden, dass für dieses System die Bagaryatsky-Orientierungsbeziehung vorliegt. Ausgehend von dieser Orientierungsbeziehung lassen sich zwölf Orientierungsvarianten ableiten. Diese zwölf Orientierungsvarianten wiederum lassen sich, je nach der kristallographischen Orientierung des Substrats, zu

Klassen von Orientierungsvarianten zusammenfassen, die sich relativ zur Oberflächennormalen der Probe unterscheiden. Es konnte gezeigt werden, dass manche Klassen dieser Orientierungsvarianten bevorzugt, andere wiederum benachteiligt gebildet werden. Dieses kann auf die Ausbildung von Fehlpassungsspannungen zurückgeführt werden. Die Klassen von Orientierungsvarianten, die bevorzugt gebildet werden, weisen die geringsten Fehlpassungsspannungen auf, die Klassen von Orientierungsvarianten die benachteiligt gebildet werden weisen, die größten Fehlpassungsspannungen auf.

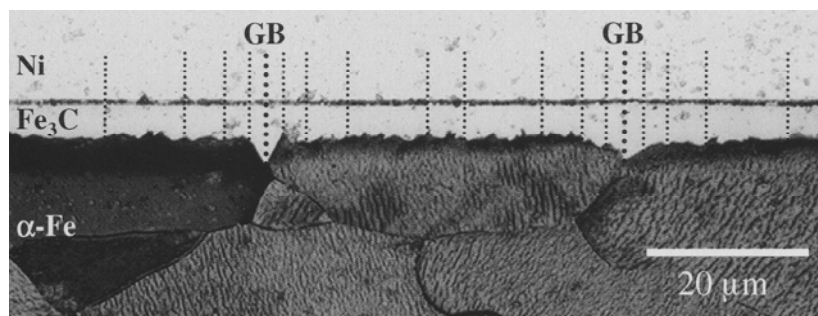


**Abb. 9.2:** Lichtmikroskopische Aufnahme (Querschliff) einer Zementitschicht auf Ferrit. Die Zementitschichtdicke ist direkt an Ferritkorngrenzen höher als davon entfernt.

Ausgehend von der Bagaryatsky-Orientierungsbeziehung kann auch die Orientierungsbeziehung zwischen benachbarten Zementitkörnern der Verbindungsschicht untersucht werden. Es konnte gezeigt werden, dass benachbarte Zementitkörner, die auf demselben Ferritkorn aufgewachsen sind, niedrigenergetische Korngrenzen ausbilden. Benachbarte Zementitkörner, die auf zwei verschiedenen Ferritkörnern aufgewachsen sind, bilden hochenergetische Korngrenzen aus. Die Ausbildung von hochenergetischen Korngrenzen zwischen benachbarten Zementitkörnern begünstigt den Kohlenstofftransport über Korngrendiffusion. Diese These wird durch experimentelle Daten untermauert: Direkt an Ferrit-Ferrit Korngrenzen, wo zwei benachbarte Zementitkörner aufeinandertreffen, die auf diesen zwei verschiedenen Ferritkörnern aufgewachsen sind, ist die Zementitschichtdicke größer als entfernt von Ferrit-Ferrit Korngrenzen (Abb. 9.2).

### 9.3.3 Stickstofftransport durch Zementit

Bis dato wurde in der Literatur weder über die Diffusivität von Stickstoff noch über die Aktivierungsenergie der Stickstoffdiffusion in Zementit berichtet. Diese werden in *Kapitel 5* dieser Arbeit über Härte-Tiefenprofile in Ferrit experimentell bestimmt (Abb. 9.3). Auf dem ferritischen Reineisensubstrat befand sich eine wachsende Zementitschicht zeitabhängiger Zementitschichtdicke. Durch die oberflächliche Zementitschicht erfolgt Stickstoffdiffusion, d.h. das darunterliegende ferritische Reineisensubstrat wird mit Stickstoff angereichert, der interstitiell gelöst ist. Durch den Einbettprozess, der für die metallographische Untersuchung notwendig ist und als Wärmebehandlung angesehen werden kann, bilden sich  $\alpha''$ - $\text{Fe}_{16}\text{N}_2$  Ausscheidung im Reineisensubstrat, die für dessen erhebliche Härtesteigerung verantwortlich sind. Die Höhe des Härteanstiegs im Reineisensubstrat ist ein Indikator für dessen Stickstoffgehalt.

Zusätzlich zur Bestimmung von Härte-Tiefenprofilen in Ferrit wurden chemische Analysen zur Bestimmung der Stickstoffgehalte im Reineisensubstrat durchgeführt. Dadurch konnte eine Kalibriergerade erzeugt werden, die einen Zusammenhang zwischen Härte und Stickstoffgehalt des Reineisensubstrats herstellt. Mit Hilfe dieser Kalibriergeraden können Härte-Tiefenprofile in Stickkonzentrations-Tiefenprofile umgerechnet werden (Abb. 9.3).

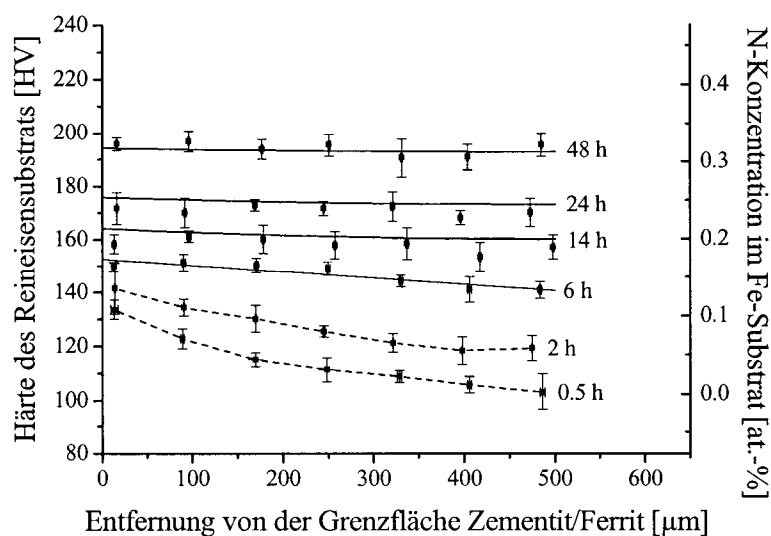


**Abb. 9.3:** Härte-Tiefenprofile in Ferrit nach unterschiedlich lange durchgeführten Nitrocarburierbehandlungen bei 823 K unter Ausbildung von oberflächlichen Zementitschichten. Mit Hilfe der Kalibriergeraden kann das Härte-Tiefenprofil in ein Stickstoffkonzentrationsprofil umgerechnet werden.

Solche Stickstoffkonzentrations-Tiefenprofile wurden anhand eines neu entwickelten Modells mittels der impliziten, finiten Differenzenmethode simuliert. Die simulierten Stickstoffkonzentrations-Tiefenprofile wurden an die experimentell bestimmten Profile angepasst, indem die Summe der quadrierten Differenzen zwischen simulierten und experimentell bestimmten Stickstoffkonzentrationswerte minimiert wurde. Als Ergebnis dieser Simulation wurden zum ersten Mal Werte sowohl für die Diffusivität von Stickstoff als auch für die Aktivierungsenergie der Stickstoffdiffusion in Zementit erhalten. Die bestimmte Aktivierungsenergie der Stickstoffdiffusion in Zementit ist relativ klein und liegt im Bereich der Werte, die für Stickstoff- bzw. Kohlenstoffdiffusion in Ferrit berichtet wurden. Dieses kann damit erklärt werden, dass Stickstofftransport in Zementit hauptsächlich über Zementitkorngranzendiffusion erfolgt.

#### 9.3.4 Neue Informationen über das Fe–N–C system

Bis dato wurde in der Literatur zum einen generell die Existenz des Zweiphasengebiets  $\alpha\text{-Fe} + \varepsilon\text{-Fe}_3(\text{N,C})_{1+x}$  und zum anderen die Frage, bei welcher Temperatur sich dieses Zweiphasengebiet öffnet, kontrovers diskutiert. Die Existenz dieses Zweiphasengebiets steht direkt im Zusammenhang mit der invarianten Übergangsreaktion  $\gamma\text{-Fe}_4\text{N} + \text{Fe}_3\text{C} \rightarrow \alpha\text{-Fe}[\text{N,C}] + \varepsilon\text{-Fe}_3(\text{N,C})_{1+x}$ , die bei *einer* bestimmten Temperatur abläuft.

In *Kapitel 6* dieser Arbeit konnte zum ersten Mal die Existenz des Zweiphasengebiets  $\alpha\text{-Fe} + \varepsilon\text{-Fe}_3(\text{N,C})_{1+x}$  experimentell nachgewiesen werden. Darüber hinaus konnte durch Nitrocarburierexperimente und systematische Auslagerungsexperimente (nach erfolgten Nitrocarburierexperimenten) die invariante Übergangsreaktion verfolgt werden und die Temperatur, bei der diese Reaktion abläuft, auf den Temperaturbereich von 833 K – 843 K eingegrenzt werden. Es konnte gezeigt werden, dass die Elektronenrückstreubeugung eine sehr gute Methode ist, um eine gezielte Phasenidentifikation innerhalb der Mikrostruktur (Verbindungsschicht) der Probe durchzuführen.

Die gewonnenen Ergebnisse geben Aufschluss über die Konstitution des ternären Phasendiagramms Fe–N–C. Des Weiteren könnten die gewonnenen Ergebnisse von technischer Relevanz sein, wenn es darum geht reine  $\varepsilon\text{-Fe}_3(\text{N,C})_{1+x}$ -Schichten zu erzeugen, denen oftmals bessere Adhäsions- und Korrosionsbeständigkeits-eigenschaften als anderen Phasen der Verbindungsschicht nachgesagt werden.

### 9.3.5 Elastische Konstanten des Zementits

Trotz der Tatsache, dass zementithaltige Stähle in technischen und industriellen Anwendungen weit verbreitet sind, ist wenig über die mechanischen Eigenschaften des Zementits bekannt. Dadurch, dass es extrem schwierig ist, einphasige, polykristalline Zementitproben zu erzeugen, sind bis dato experimentell bestimmte einkristallelastische Konstanten des Zementits unbekannt. Dieses macht die Untersuchung und die Modellierung des elastischen Verhaltens des Zementits auf mechanische Deformation unmöglich. Kürzlich wurde in der Literatur davon berichtet, dass die neun unabhängigen elastischen Konstanten des Zementits mit *first-principles*-Methoden berechnet wurden.

In *Kapitel 7* dieser Arbeit wurden die neun unabhängigen elastischen Konstanten des Zementits zum ersten Mal als Funktion des Druckes berechnet. Die Ergebnisse dieser Berechnungen zeigen, dass Zementit eine extreme Anisotropie der elastischen Konstanten aufweist. So erhält man anhand der Berechnungen einen extrem kleinen Wert von  $c_{44}$  relativ zu  $c_{55}$  und  $c_{66}$ . Die extreme Anisotropie des Zementits, die aus diesen Berechnungen hervorgeht, wurde in *Kapitel 7* dieser Arbeit experimentell bestätigt. Es wurden Spannungsmessungen mit Synchrotronstrahlung an Zementitschichten auf ferritischen Reineisensubstraten durchgeführt. Die Zementitschichten weisen Druckeigenstressungen auf; die *hkl*-abhängige, spannungsinduzierte Reflexverschiebung der Zementitreflexe kann als experimenteller Beweis für die extreme, elastische Anisotropie des Zementits herangezogen werden.

---

## *List of publications*

1. T. Gressmann, M. Nikolussi, A. Leineweber, E.J. Mittemeijer: *Formation of massive cementite layers on iron by ferritic carburising in the additional presence of ammonia*, Scr. Mat. 55 (2006) 723.
2. A. Leineweber, T. Liapina, T. Gressmann, M. Nikolussi, E.J. Mittemeijer: *Phase transformations and interstitial atom diffusion in iron-nitride, iron-carbonitride and iron-carbide layers*, Adv. Sci. Tech. 46 (2006) 32.
3. M. Nikolussi, A. Leineweber, E. Bischoff, E.J. Mittemeijer: *Examination of phase transformations in the system Fe–N–C by means of nitrocarburising reactions and secondary annealing experiments; the  $\alpha + \epsilon$  two-phase equilibrium*, Int. J. Mat. Res. 98 (2007) 11.
4. M. Nikolussi, S.L. Shang, T. Gressmann, A. Leineweber, E.J. Mittemeijer, Y. Wang, Z.-K. Liu: *Extreme elastic anisotropy of cementite, Fe<sub>3</sub>C: First-principles calculations and experimental evidence*, Scr. Mat. 59 (2008) 814.
5. M. Nikolussi, A. Leineweber, E.J. Mittemeijer: *Microstructure and crystallography of massive cementite layers on ferrite substrates*, Acta Mat. in press.
6. M. Nikolussi, A. Leineweber, E.J. Mittemeijer: *Growth of massive cementite layers; thermodynamic parameters and kinetics*, submitted for publication.
7. M. Nikolussi, A. Leineweber, E.J. Mittemeijer: *Nitrogen diffusion through cementite layers*, submitted for publication.





## *Danksagung*

Die vorliegende Arbeit wurde am Institut für Metallkunde der Universität Stuttgart und am Max-Planck-Institut für Metallforschung angefertigt. An dieser Stelle möchte ich all denen herzlich danken, die zum Gelingen dieser Arbeit beigetragen haben.

Allen voran möchte ich mich bei Herrn Prof. Dr. Ir. E.J. Mittemeijer für die freundliche Aufnahme in seine Abteilung und das damit in mich gesetzte Vertrauen bedanken. Seine Betreuung durch die monatlichen Treffen und die damit verbundenen wissenschaftlichen Diskussionen gaben mir stets das Gefühl auf dem richtigen Weg zu sein. Ich empfand es als sehr wertvoll, dass ich in wissenschaftlicher Hinsicht immer freie Hand bei der Gestaltung meiner Arbeit hatte.

Herrn Priv.-Doz. Dr. J. Bill danke ich für die freundliche Übernahme des Mitberichts und Herrn Prof. Dr. H. Bertagnolli danke ich für die Zusage, den Prüfungsvorsitz zu übernehmen.

Herrn Dr. A. Leineweber, meinem täglichen Betreuer, gebührt ein ganz besonderer Dank. Er hat durch sein unerschöpfliches Fachwissen wesentlich zum Gelingen dieser Arbeit beigetragen. Darüber hinaus konnte man mit ihm in freundschaftlicher Atmosphäre über jegliche Probleme des Wissenschaftsalltags diskutieren.

Allen Mitarbeiterinnen und Mitarbeitern des Max-Planck-Instituts für Metallforschung, insbesondere den Kollegen der Abteilung Mittemeijer, möchte ich für die freundschaftliche Zusammenarbeit danken. Ich habe die Zeit in dieser Abteilung sehr genossen.

Zu guter Letzt möchte ich meiner Familie dafür danken, dass sie mich stets in allen Belangen unterstützt hat, mich motiviert hat und mir in dieser Zeit auch immer viel Verständnis entgegengebracht hat.



---

## *Curriculum Vitae*

### **Persönliche Daten**

Name                    Marc Nikolussi  
geboren                am 20.03.1980 in Ehenbichl (Österreich)

### **Schulbildung**

1987-1991              Grundschole Höfingen  
1991-2000              Johannes-Kepler-Gymnasium Leonberg  
mit dem Abschluss: Allgemeine Hochschulreife

### **Hochschulbildung**

2000-2005              Studium im Diplomstudiengang Werkstoffwissenschaft an der  
Universität Stuttgart mit dem Abschluss: Diplom-Ingenieur  
2005                      Diplomarbeit am Institut für Metallkunde der Universität Stuttgart  
mit dem Thema: „Zementitbildung beim Nitrokarburieren und  
Karburieren von Eisen“  
Hauptberichter: Prof. Dr. Ir. E.J. Mittemeijer

### **Promotion**

2005-2008              Max-Planck-Institut für Metallforschung, Stuttgart und Institut für  
Metallkunde der Universität Stuttgart  
Thema: „Cementite in the Fe-N-C system“  
Hauptberichter: Prof. Dr. Ir. E.J. Mittemeijer